Printability, mechanical and thermal performance study of sustainable concrete lattice structures

A thesis submitted

in partial fulfillment of the requirements

for the degree of

Doctor of Philosophy

By

Dhrutiman Dey

(Roll No: 206103110)

Under the supervision of

Dr. Biranchi Panda

Department of Mechanical Engineering

Indian Institute of Technology Guwahati

June, 2025

Department of Mechanical Engineering
Indian Institute of Technology Guwahati
Guwahati – 781039
INDIA

CERTIFICATE

It is certified that the thesis entitled "Printability, mechanical and thermal performance study of sustainable concrete lattice structures" submitted by Dhrutiman Dey (Roll No. 206103110), to the Indian Institute of Technology Guwahati, India, for the award of Doctor of Philosophy has been carried out under my supervision in the Department of Mechanical Engineering, Indian Institute of Technology Guwahati. I further certify that this work has not been submitted elsewhere for the award of any other degree or diploma and meets the requirements as prescribed by the regulations of the institute for the award of the doctoral degree.

Dr. Biranchi Panda
Assistant Professor
Department of Mechanical Engineering
Indian Institute of Technology Guwahati
Guwahati-781039, Assam, India
Date:

Department of Mechanical Engineering
Indian Institute of Technology Guwahati
Guwahati – 781039
INDIA

DECLARATION

I declare that this written submission represents my idea in my own words and where others' ideas or words have been included, I have adequately cited and referenced the original sources. I also declare that I have adhered to all principles of academic honesty and integrity and have not misrepresented or fabricated any idea/data/fact/source in my submission. I understand that any violation of the above will cause for disciplinary action by the institute and can evoke penal action from the sources which have thus not been properly cited or from whom proper permission has not been taken where needed.

Date: 11/06/2025

Dhrutiman Dey
Roll No.: 206103110

Dedicated

to

My Parents & Supervisor

ACKNOWLEDGEMENT

This thesis is the culmination of the collaborative efforts of numerous individuals who have supported me, both directly and indirectly, throughout this journey. First and foremost, I express my deepest respect and sincere gratitude to my supervisor, Dr. Biranchi Panda for his invaluable advice, resourceful guidance, inspiring instructions, active supervision, and constant encouragement. His unwavering support has been instrumental in shaping my research and academic growth.

I am profoundly grateful to my Doctoral Committee members Prof. Pankaj Biswas, Prof. Manas Das, and Prof. Bulu Pradhan for their keen support. I extend my appreciation to the Head of the Mechanical Engineering Department (both past and present) and all faculty members, especially Prof. Amaresh Dalal for his insightful suggestions at the critical juncture of my thesis work. I also thank the laboratory staff and scientific officers of the Central Instruments Facility (CIF), Civil Engineering Department of IIT Guwahati, and the Centre for Advanced Research in Building Science & Energy (CARBSE), Ahmedabad, India, for their assistance in conducting the experimental work.

My sincere gratitude extends to my industry collaborators Dr. Jagabandhu Kole and Mr. Manoj Rustagi from JSW Cement Limited, as well as my academic collaborators Dr. Jonathan Tran and Dr. Vuong Nguyen Van from the Department of Civil and Infrastructure Engineering, RMIT University, Australia, and Dr. Rajan Rawal and Dr. Yash Shukla from CEPT University, Ahmedabad, India. Their continuous support, technical discussions, and expertise have greatly helped in my research.

I am also thankful to my labmates, colleagues, and seniors, including Dr. Niranjan Kumar Choudhury, Dr. Uday Boddepalli, Dr. Dheeraj Kumar, Mr. Dodda Srinivas, Mr. Boda Ramalingaiah, Mr. Akshay Sahu, Mr. Shubham Maurya, Mr. Lalit Kumar, Ms. Syed Bustan Fatima Warsi, Mr. Srajan Prakash, Mr. Ventrapragada Durga Prasad, Mr. Dileswar Meher, Mr. C. Aswin Karthik, Mr. Jagannath Verma, Mr. Amit Kumar Chaurasiya, Mr. Ankit Dwivedi, Mr. Deepak Kumar Rathour, Mr. Antash Kishore Sinha, Mr. Manish Dalakoti, Mr. Subhojit Jash, Mr. Arup Kumar Mohapatra, Mr. Abhishek Parida, Mr. Giridhar Raveendar, Mr. Rongali Mahesh, and Ms. Limashree Sahoo. Their stimulating discussions and unwavering support made my research journey a truly enriching experience.

A special expression of gratitude is reserved for my all-time well-wishers HG Anukulchandra Chakravarty, HG Srila Prabhupada, Shri Rasaparayana Dasa, Dr. Tvarit Patel, Dr. Karisma Mohapatra, Dr. Snehasish Panigrahy, Mr. Chandan Kumar Sahoo, Mr. Satyanarayan Pruseth, Mr. Rakesh Tunk, Mr. Ronit Muduli, Mrs. Gayatri Sahoo, Mrs. Lipsa Sahoo, Ms. Lata Yadav, and Ms. Anjli for their positive influence throughout my PhD journey.

Finally, and most importantly, I wish to express my deepest gratitude to Lord Jagannath, whose divine arrangements have given me the necessary strength to stand still in all circumstance during my PhD journey. Last but not least, I extend my heartfelt thanks to my parents, sister, brother-in-law, all other family members and well-wishers for their unwavering love, constant moral support, and encouragement. I owe everything to them, their belief in me has been the driving force behind all my accomplishments.

With immense gratitude,

DHRUTIMAN DEY

Abstract

Concrete 3D printing (3DCP) is an advanced construction technology that uses additive manufacturing technique to build structures layer by layer, offering greater precision, reduced waste, and design flexibility compared to traditional methods using formwork. Despite these advantages, 3DCP faces significant challenges that must be addressed to enhance its sustainability and functionality. 3D printable concrete typically requires no coarse aggregate, higher cement paste volume and induce significant embodied carbon. The usage of fine aggregates, often sourced from natural river sand causes ecological damage, including habitat destruction and biodiversity loss. Consequently, there is an urgent need for the development of low carbon 3DCP mixes by utilizing local materials and industrial wastes. The material as well as 3D printed structure design can be tailored for improving fresh, hardened and functional properties such as thermal conductivity, which perfectly align with the growing demand for sustainable and functional structures in the built environment. The main objective of this research is three-fold: (1) development and characterization of 3D printable sustainable mortar mixes using two steel industry by-products such as Portland slag cement and slag sand (2) exploring flexural response of 3D printed concrete structures with different lattice configurations and (3) an accurate steady-state approach for comprehension of thermal performance of lattice infilled 3D printed concrete walls.

First, the development of sustainable 3D printable thixotropic mortar is explored, aiming to uncover the influence of Portland slag cement (PSC) and slag sand (SS) on fresh, hardened and thermal properties. The results of printing trials revealed smooth extrusion of fresh concrete, characterized by the excellent dynamic yield stress and plastic viscosity, affected by the PSC and SS content. The angular morphology of SS enhanced inter-particle friction, while PSC's finer particles and high reactivity contributed to better cohesion and print stability. The synergetic effect of PSC and SS resulted highest buildability but reduced the open time to 20 minutes, compared to the control (OPC and river sand) mix having 40 minutes' open time. In the hardened state, SS improved thermal resistance by reducing crystallinity and increasing phonon scattering but directional compressive strength was slightly reduced due to the higher porosity. It was also found that PSC resulted in improved carbon sequestration capacity by decalcifying secondary hydration products. These findings were substantiated by microstructural analyses, including X-ray diffraction (XRD), thermo-gravimetric analysis (TGA/DTG), and mercury intrusion porosimetry (MIP). Despite the higher cost associated with

SS, the sustainability analysis highlights lowest equivalent CO_2 emissions (327 kg/m^3) for mixes containing both SS and PSC. These results show potential of direct utilization of the steel industry by-products to formulate printable mortar mixes, while addressing both material performance and ecological sustainability.

Second, flexural performance of 3D-printed concrete beams with extant lattice infilled configurations was experimentally tested in two different loading (vertical/transverse) directions. A multi-scale finite element (FE) simulation was developed to model the mechanical behavior, and the proposed FE model was calibrated through experimental testing. The comparative analysis of simulation and experimental results proves the reliability of the numerical model, which correctly estimated the peak load and damage patterns. Leveraging this validated model, parametric studies were conducted by varying the ratio of horizontal-to-triangular pattern lengths to optimize the infill design. These studies led to the development of lattice infill-optimized simply supported beam, achieving a substantial improvement in peak load (60%) and maximum midpoint displacement (12%). These findings underscore the critical role of infill configuration optimization in enhancing structural performance, offering a pathway for design of light weight 3D-printed concrete components.

Third, thermal performance of 3D-printed concrete walls with different lattice infill configurations was explored through a combination of experimental testing and steady state CFD numerical modelling, aiming to uncover the underlying mechanism, direction and magnitude of heat flow affecting thermal transmittance. A calibrated numerical model accurately predicted the thermal performance, underscoring reliability of the proposed model. Based on the model suggested heat transfer mechanism, we expand the lattice design space, aiming to uncover configurations that exhibit superior performance with insulation material. The results indicate lowest U-value (0.79 W/m^{2}K) of modified partially insulated lattice infill wall, surpassing the studied configurations. This study offers a critical evaluation of infill configurations to develop thermally efficient cost-effective concrete wall, that align with the growing demand for lightweight, functional structures in built environment. In summary, the present work advances the research in 3DCP by developing printable sustainable mixes along with model driven strategies to design infill lattice configurations for lightweight structures, where both mechanical and thermal performance are essential.

Table of Contents

List of Figures

List of Tables

CHAPTER 1

Introduction

This chapter provides a general introduction to concrete 3D printing and outlines the objectives, scope, and organization of the thesis.

1.1 Background and motivation

3D Concrete printing (3DCP) has emerged as a transformative technology in the construction industry, offering remarkable potential for both sustainability and functionality. Unlike conventional construction methods, which are often resource-intensive and time-consuming, 3DCP provides a highly automated approach to building complex structures with reduced material waste [1]. 3D concrete printing has gained significant attention in the recent past, primarily because of its ability to eliminate formwork for concrete construction, thereby enabling the construction of complex, structurally and functionally efficient geometries [2,3]. Extrusion-based printing technique is currently the most widely explored method for in-situ and pre-cast concrete 3D printing applications. This technique extrudes fresh mortar from a digitally controlled nozzle mounted on a gantry or robotic arm to print a structure layer-by-layer.

The performance of 3D-printed concrete is heavily influenced by the choice of materials, which play a crucial role in both printability and sustainability [3]. Printability refers to the material's rheological properties, such as extrudability, buildability, and open time, which govern the success of layer-by-layer deposition without deformation or collapse. A large number of ongoing studies focus on the use of alternative binders, which has been widely recognized as a sustainable option to reduce the carbon footprint of printable concrete. More recently, materials like portland slag cement (PSC) and slag sand (SS), derived from industrial by-products, have emerged as promising alternatives to conventional materials like ordinary portland cement (OPC) and natural river sand [4]. These materials can not only address the critical issue of industrial waste management but also have potential to enhance the sustainability and performance of 3DCP.

For large-scale construction, the integration between 3DCP and lattice infilled configurations opens up opportunities for fabricating sustainable and structurally efficient structures such as lattice beams, walls etc. These lattice configurations, characterized by their repetitive patterns of interconnected elements, provide a unique interplay of stiffness, strength, and material efficiency. Lattice configurations have demonstrated exceptional capabilities in optimizing the mechanical performance of structures by effectively distributing loads, mitigating stress concentrations, and enhancing overall performance. Due to high strength-to-weight ratio, the flexural performance of such structures is of particular interest to many designers, as it directly

influences their suitability for many load-bearing applications. In addition to mechanical performance, the thermal behavior of 3D printed concrete walls is of significant interest, particularly in the context of energy-efficient buildings and infrastructure. The inherent cavity of lattice infilled designs promotes thermal insulation by disrupting heat transfer pathways, making them suitable for applications in building envelopes and climate-responsive structures. However, the thermal performance of these systems is influenced by multiple factors, including material thermal conductivity, lattice configurations, and external environmental conditions. Thus, in order to optimize the lattice design via unravelling the stress distribution and heat transfer mechanisms within the lattice structures, numerical simulations and experimental validations are essential. These insights will facilitate the development of 3D printable sustainable materials and lattice infilled structure design strategies with tailored mechanical and thermal performance.

The rapid development of 3DCP technology presents significant opportunities for advancing construction processes, yet it is accompanied by considerable challenges that must be addressed to enhance both its sustainability and functionality. A primary concern lies in the composition of 3DCP mixtures, which typically require higher binder contents, primarily OPC based binder, compared to conventional concrete. While this increased binder content is necessary to achieve the requisite rheological properties for 3D printing, it simultaneously elevates the environmental impact. High thermal conductivity of the printed materials is also another challenge, which limits their potential for energy-efficient building solutions. Beyond material, structural integrity and thermal comfort of printed structures depends on infilled lattice configurations. Addressing these challenges presents an opportunity to significantly enhance the environmental sustainability and performance of 3DCP systems, thereby paving the way for more efficient and eco-friendly construction practices in the future.

1.2 Objective of the thesis

Building upon the challenges identified in the motivation, this research seeks to address the critical gaps in sustainability and performance improvement for 3D printed concrete structures. The study emphasizes advancing material composition, optimizing structural design, and enhancing thermal performance to foster the widespread adoption of 3DCP in the construction industry. Accordingly, the specific objectives of this thesis are as follows:

1. Experimental investigation into the influence of portland slag cement and slag sand on sustainability and performance of 3D printable mortar.
2. Investigation of the effect of infilled lattice configurations on flexural performance of 3D printed concrete structure.
3. Improving thermal performance of 3D printed concrete walls with geometrically modified infill lattice configurations via validated simulation.

1.3 Scope

A combination of both experimental and numerical investigation approach was adapted in this research, addressing the sustainability and performance of 3D-printed concrete structures. Experimental studies were conducted using an extrusion-based, lab-scale gantry 3D printer with an auger screw extrusion system, capable of pumping batch-mixed material over a maximum distance up to 3 meters. The printable mortar was developed using PSC and SS as substitutes for OPC and river sand, without incorporating special admixtures such as accelerators or retarders, to ensure simplicity, cost-effectiveness, and practicality for field applications. Numerical simulations adopted in this study was limited to a simplified modelling approach, applying tie constraints between the printed layers and thereby enhancing computational efficiency. Mechanical performance investigation was focused on flexural behaviour of the printed beam elements subjected to three-point loading conditions, while the thermal performance study was limited to wall elements only, which are predominant fraction of a building envelope. The scope deliberately excludes alternative printing technologies, advanced material formulations, and interfacial modeling, offering a focused yet comprehensive exploration of sustainable materials and performance enhancement for 3DCP.

1.4 Thesis organization

This thesis is organized into six chapters, focusing on a specific aspect of the research related to sustainable and performance-enhanced 3D concrete printing. Chapter 1 introduces the field of concrete 3D printing, outlining the motivation, objectives, and scope of the study, as well as providing an overview of the thesis structure. Chapter 2 presents a comprehensive literature review, covering material requirements for 3D concrete printing, eco-friendly industrial waste materials, their fresh and hardened state properties, along with the mechanical and thermal performance of various infill patterns used in 3DCP. Chapter 3 investigates the printability of sustainable slag-based concrete, focusing on the effect of PSC and SS on the rheological,

mechanical, and thermal properties. Chapter 4 examines the effect of different infill lattice patterns on flexural performance of 3D printed beams through seamlessly combining experimental testing and multi-scale numerical simulations. Chapter 5 delves into a comprehensive investigation into the thermal performance of 3D-printed concrete lattice walls via a calibrated CFD simulation. Finally, Chapter 6 provides the conclusions drawn from the research, summarizing the key findings and contributions to the field of 3D concrete printing, and discusses potential future research directions to further advance the sustainability and performance of 3DCP technology.

CHAPTER 2

Literature review

Chapter 2 delves into the material requirements and advancements in concrete 3D printing, emphasizing the integration of eco-friendly industrial waste materials. It explores key factors influencing material selection, challenges in their incorporation, and their impact on fresh and hardened properties. Additionally, the chapter examines the mechanical and thermal performance of various infill patterns, providing a holistic understanding of the material and lattice infill design considerations critical to 3DCP.

A portion of this chapter has been published in:

Dey, D., Srinivas, D., Panda, B., Suraneni, P., & Sitharam, T. G. (2022). Use of industrial waste materials for 3D printing of sustainable concrete: A review. Journal of Cleaner Production, 340, 130749. https://doi.org/10.1016/j.jclepro.2022.

2.1 Concrete 3D printing

Since ages, traditional construction is treated as a slow and segmented process as it involves several stages e.g. formwork installation, pouring the concrete, waiting for it to harden and then formwork removal for every construction component (**Figure 2.1**). The introduction of additive manufacturing in construction, also termed as 3D Concrete Printing (3DCP) is gaining a lot of attention from both academia and industry as it holds the potential to print the structure without any formwork. In addition, reduced human involvement, minimum material wastage, and mass customization act as added advantages to it [5].

Figure 2.1 Steps in conventional construction method.

The rapid development of large-scale 3DCP technology can be categorised into two main techniques, namely (1) Binder jetting and (2) Extrusion based 3D printing. Binder jetting involves the sequential deposition of powder layers onto a build platform, followed by the application of a binder along predefined paths to create the desired geometry [6]. While it offers high precision and flexibility, binder jetting requires additional post-processing steps, such as the removal of uncured powder from the final structure, and relies on the movement of the substrate, making it more suited for relatively small-scale, pre-cast components. In contrast, extrusion-based 3DCP (see **Figure 2.2**), enables the production of large-scale structures both off-site and on-site. In this method, layers are successively extruded according to the specifications of a computer-aided design (CAD) model, with the main challenge being the development of a material that can maintain its shape and support the weight of multiple layers without significant deformation [7]. As extrusion-based technology is considered more practical and feasible for large-scale construction worldwide, this thesis aims to take it to the next level by addressing key challenges and improving its functionalities and applicability.

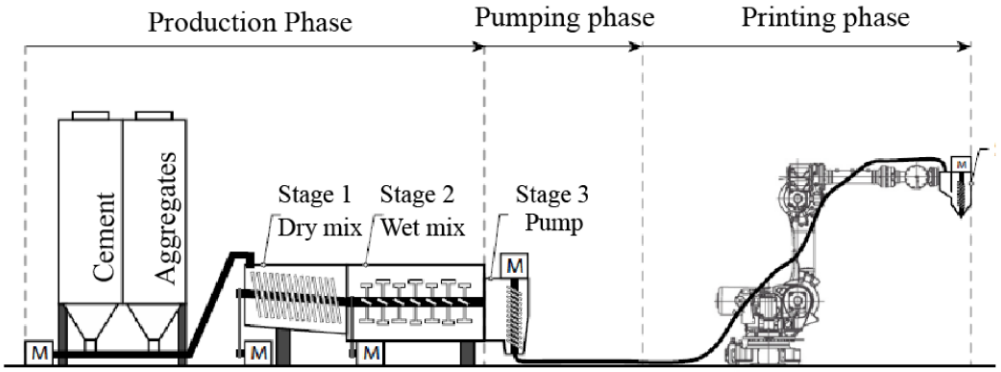

Figure 2.2 Schematic of different phases of 3DCP [7].

In general, 3D printing of materials such as metals, plastics, and polymers involves hardening of the deposited layers through melting. However, the solidification of the print material in 3DCP occurs as a (relatively) slow chemical process, namely the exothermal hydration reaction between cementitious materials and water [8]. As illustrated in **Figure 2.3**, the interdependency of material properties, design parameters, and the resulting performance of the printed component is a critical consideration in 3DCP. To address these complexities, the literature review section has been expanded to provide a detailed exploration of each of these interconnected aspects, offering a comprehensive understanding of their role in advancing construction 3D printing technology.

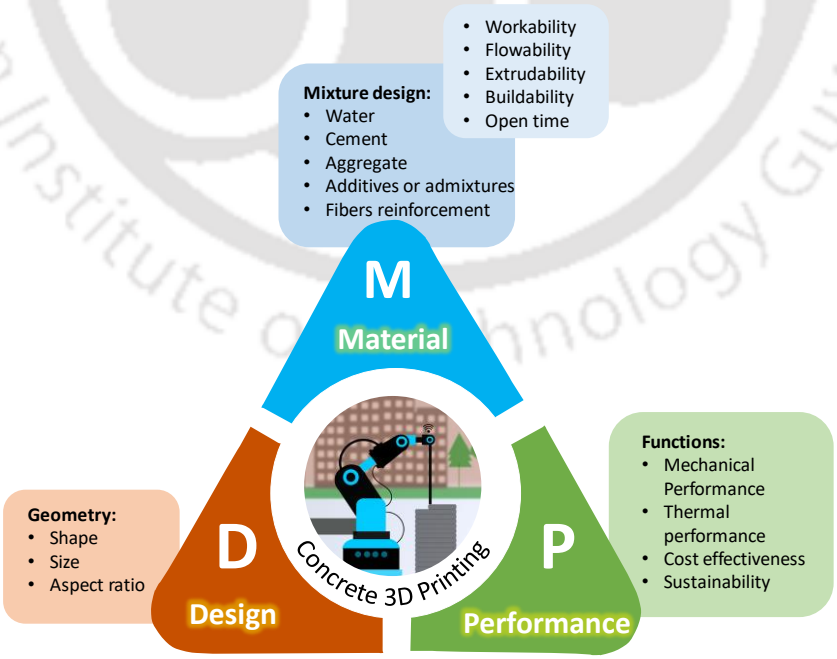

Figure 2.3 Interdependency of material, design and performance in 3DCP.

2.2 Material properties requirement for 3DCP

The 3DCP differ significantly from traditional casting processes by virtue of the importance of control of the yield stress, and especially with respect to its evolution over time. More specifically, the requirements of material delivery and placement are similar to some processes seen in traditional construction processes, but the absence of a traditional formwork requires an additional aspect, that of controlling structural build-up, to ensure stability during production [9]. In the printing process, appropriate workability is required to ensure extrudability, shape stability and buildability after deposition. More specifically, to achieve printable concrete, it is needed to balance among these critical printing requirements.

Workability of fresh 3DCP is commonly evaluated using slump test, flow test or V-funnel test. In the slump test, workability is evaluated through the slump, which is the slumped height of concrete paste relative to the height of the cone after demolding. Additionally, V-funnel is used to evaluate flow ease by the flow time [10]. Flow test, also called slump flow test, spread-flow test or mini-slump test, is the most widely used to measure workability of printable concrete because it is simple, fast, economical and reliable. Rheological parameters such as static/dynamic yield stress and plastic viscosity obtained from rheological tests are also considered important properties to evaluate flowability of fresh concrete. For instance, static yield stress needs to be sufficiently low for being pumpable and high enough for carrying self-weight [11].

In 3DCP, the extruded layers are hardened by hydration reaction of the material and therefore, it is very important to design the material so that it can harden rapidly while retaining the nozzle shape [12]. In case of extrusion by pump, the material design is even more challenging as it needs to be very fluid during pumping and after deposition, it should be stiff enough to hold its own weight and the load of other layers. After successful extrusion, buildability of fresh concrete must be ensured, and it depends on shape stability of each filament [13]. As discussed above, fresh concrete is required to have appropriate workability to meet two competing requirements i.e. ‘extrudability’ and ‘buildability’. These requirements vary across different timescales during the printing process, from mixing to final setting as shown in **Figure 2.4**, making material design inherently complex [14].

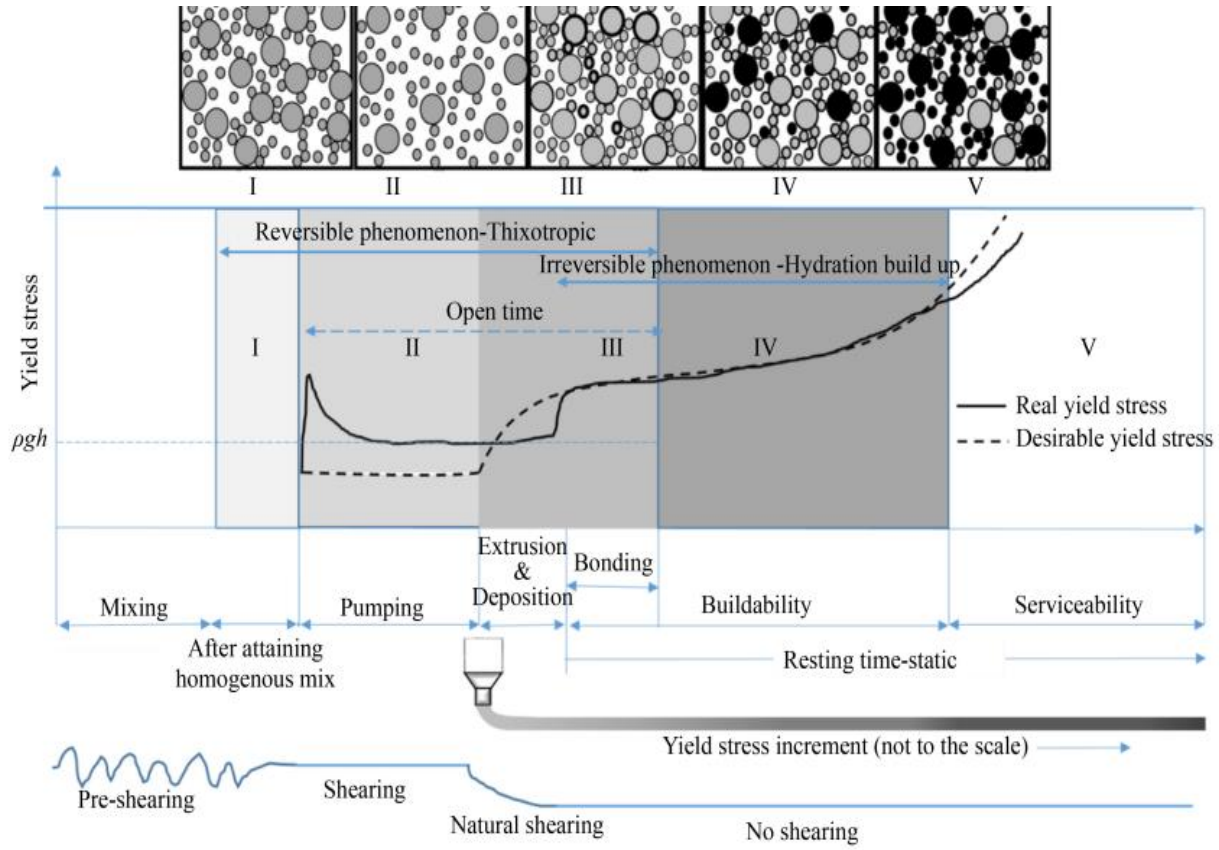

Figure 2.4 Yield stress growth at different printing time scale [14].

Mixing phase (Zone I): During the initial mixing phase, the challenge lies in achieving homogeneity in the material which can be effectively solved by incorporation of chemical admixtures such as superplasticizers (SP) and viscosity-modifying agents (VMA). The yield stress remains low at this stage due to the absence of significant hydration effects. Critical factors include:

- Flowability: Ensuring the material is sufficiently fluid to facilitate uniform mixing without segregation.
- Particle dispersion: Proper dispersion of cement particles is essential to avoid agglomeration and ensure consistent rheological behavior.

Pumping and extrusion phase (Zone II): The material transitions to the pumping and extrusion stage, where it undergoes deflocculation due to shearing forces. Key factors include:

- Thixotropy: The ability of the material to regain structure after shear thinning is critical for maintaining shape stability post-extrusion.

- Pumpability and extrudability: The material must flow smoothly through the pump and nozzle without clogging while maintaining cohesion to avoid cracking during extrusion.

Open time and green strength development (Zone III): In this phase, the material begins to exhibit reflocculation as it rests between layers. The yield stress increases steadily, contributing to green strength development. However, achieving an optimal balance is critical:

- Open time: The material must maintain sufficient workability to ensure proper bonding between layers.
- Green strength: Rapid development of green strength is necessary to support subsequent layers without deformation or collapse.

Rigidification and buildability phase (Zone IV): As the hydration process intensifies, the material undergoes rigidification, which is marked by exponential strength growth. Critical considerations include:

- Rate of rigidification: This must align with the printing speed to prevent cold joints and ensure seamless layer bonding.
- Dimensional stability: The printed structure must resist deformation under its weight and external loads.

Setting and long-term performance (Zone V): In the final phase, irreversible structural build-up occurs as the material sets. This stage determines the strength, durability and serviceability of the printed structure. Key factors include:

- Hydration dynamics: Proper curing time facilitates continued hydration, essential for developing strength and reducing porosity.
- Microstructural development: A dense and uniform microstructure ensures hardened state properties such as dry density, compressive strength, thermal conductivity etc.

As highlighted in the preceding discussion, achieving this balance necessitates a comprehensive understanding of fresh state and hardened state properties. However, alongside optimizing these properties, there is a growing need to address the environmental challenges associated with the extensive use of natural resources in concrete production. This pressing concern has driven researchers toward the utilization of industrial waste as a sustainable alternative for both binder and aggregate replacement [15]. The integration of industrial waste materials in 3DCP not only contributes to resource conservation and waste management but also presents unique challenges and opportunities in tailoring the material properties.

2.2.1 Overview and use of industrial wastes in 3DCP

Industrial waste, generated as byproducts from various manufacturing processes, offers significant potential to replace conventional binders and aggregate in concrete as shown in **Figure 2.5**. Fly ash (FA) and fly ash cenosphere, both by-products of coal-fired power plants, have gained prominence in 3DCP due to their pozzolanic nature and spherical morphology. Fly ash cenosphere is lightweight hollow microspheres which offer high thermal insulation and density reduction when incorporated in to the mix [16]. Silica fume (SF), a by-product of silicon or ferrosilicon alloy production, is an ultra-fine material with a high silica content (~90%) and large surface area, enhancing the strength and durability of cementitious matrices [17]. Waste slags, including ground granulated blast furnace slag (GGBFS or iron slag), steel slag, and copper slag, are derived from metallurgical industries. In general, these slags are glassy material which are rich in calcium silicate and acts as a latent hydraulic binder. Steel and copper slags are typically denser and coarser, contribute to improved aggregate properties while reducing natural resource depletion [18]. Recycled construction powder (RCP), generated from crushed and ground demolition waste, offers a low-cost binder replacement but requires treatment to remove contaminants and ensure uniformity [19]. The utilization of these wastes is influenced by factors such as particle size distribution, chemical reactivity, and compatibility with other mix components, all of which are critical for achieving optimal performance in fresh and hardened states [20].

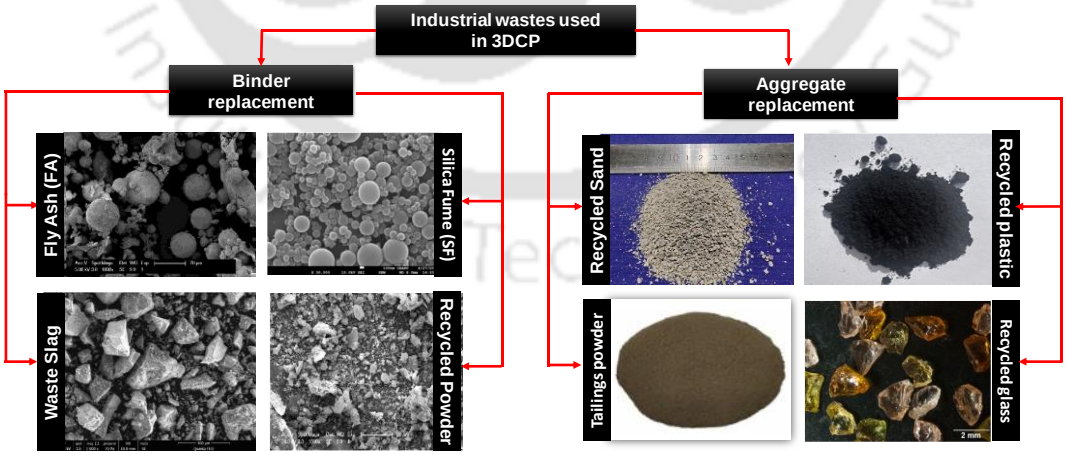

Figure 2.5 Examples of various industrial waste materials used in 3DCP [21–24].

Recycled sand, derived from crushed concrete and demolition debris, serves as an effective replacement for natural sand. It primarily comprises quartz and calcite particles, often

containing residual cement paste [25]. Recycled glass, derived from post-consumer or industrial waste, is processed into fine aggregates. The glossy, angular particles not only contribute to flowability but also provide a distinct aesthetic to 3D-printed structures. Its high silica content makes it pozzolanic when finely ground, adding strength and durability to the mix [26]. Recycled plastic and rubber powders, obtained from discarded plastic products and used tires, act as lightweight aggregate replacements. Their bulk appearance reveals irregular and porous particles, reducing the density of the concrete and mitigating shrinkage cracks [27]. Iron and copper tailings, by-products of mining processes, are commonly used as aggregate replacements [28]. Iron tailings exhibit a granular, sand-like texture, with silica and iron oxides being their primary components, as observed in their bulk form (see **Figure 2.5**). The physical characteristics of these materials guide the optimization of mix designs for sustainable 3DCP applications, reducing reliance on natural resources while effectively utilizing industrial waste.

2.2.1.1 Fly ash

Panda et al. [29] investigated the incorporation of high-volume fly ash (70%) into 3D-printable concrete and identified that low yield stress and insufficient plastic viscosity is the cause of significant bottom layer deformation. Authors found that addition of nanoclay (NC) improved shape stability by enhancing yield stress and viscosity recovery through particle reflocculation, enabling 20-layer deposition without deformation, as shown in **Figure 2.6**. In the hardened state, the compressive strength showed a slight increase (10%), while tensile bond strength decreased (33%) due to rapid yield stress buildup and poor interface bonding strength.

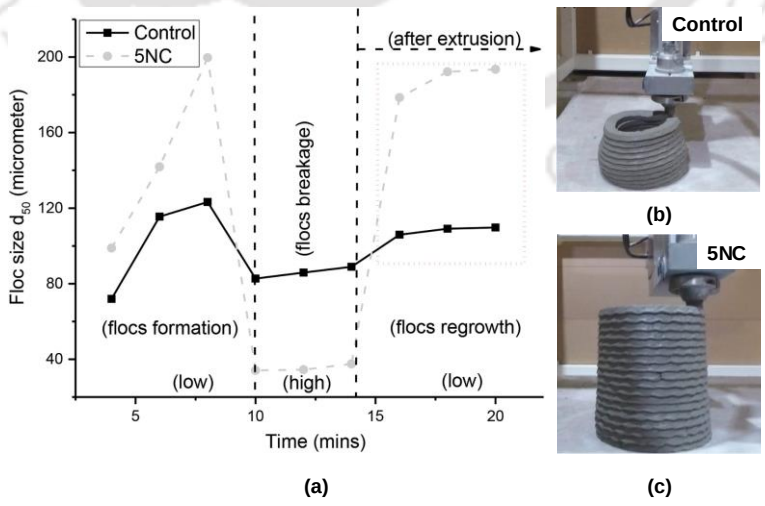

Figure 2.6 (a) Floc size variation at different shear condition, (b) Control and (c) 5NC mix buildability [29].

Wang et al. [30] investigated the incorporation of fly ash cenosphere into white portland cement for 3D printing applications. In the fresh state, control mix exhibited slow reaction kinetics, characterized by low-intensity hydration peaks and a delayed hardening process, resulting in poor buildability and deformation during printing. The addition of 25 wt.% cenosphere improved paste extrudability and retained buildability, while 4 wt.% $CaCl_2$ further enhanced hydration kinetics by intensifying hydration peaks, providing a solution to the delayed hardening challenge. In the hardened state, the inclusion of cenosphere led to a 24% reduction in thermal conductivity (from 0.95 W/mK to 0.72 W/mK), significantly enhancing thermal properties. However, this improvement came at the cost of a 33% decrease in compressive strength (from 27.7 MPa to 18.6 MPa), attributed to the lightweight and hollow structure of the cenosphere reducing material density.

2.2.1.2 Silica fume

Panda and Tan [31] demonstrated that replacing FA with 2.5 wt.% SF doubled the yield stress and structural buildup rate of high volume FA mixes while improving viscosity recovery, required for 3DCP applications. However, SF >5% caused excessive yield stress, disrupting extrusion continuity. Similarly, Kazemian et al. [32] found that 10% SF improved fresh properties, enabling the successful printing of stable 5-layered specimens. Zhang et al. [33] reported that 2% SF enhanced buildability by accelerating hydration and forming a robust flocculated microstructure, highlighting SF's role in improving early-age properties. Rubio et al. [34] reported that replacing cement with 8 wt.% SF reduced slump flow from 220 mm (unextrudable) to 175 mm, while viscosity-modifying admixtures further improved stability and minimized layer segregation in printed structures. Soltan and Li [35] found that replacing silica sand with 10 wt.% micro-silica and 5 wt.% ground silica enhanced early flowability and hardening, ensuring robust 3DCP mixtures. Similarly, Weng et al. [36] demonstrated SF's strong influence on flow resistance, making it ideal for rheology control. Aside these, several other literatures [37–43] highlight that SF and FA are commonly incorporated into 3DCP mixtures to enhance yield stress and structural build-up rates. However, the ultrafine particle size of these materials poses a challenge by substantially increasing the water demand, which can be effectively addressed through the inclusion of superplasticizers and other concrete additives.

2.2.1.3 Waste slag

Several studies [44–48] have explored the development of slag-based OPC mixtures for 3DCP, incorporating conventional slag and its derivatives such as steel slag, copper slag, and iron-rich slag as key components in the mixture formulation. To investigate the specific effect, Panda et al. [49] examined the rheological properties and compressive strength of ternary blends comprising cement, lime, and slag (with slag constituting 70–85 wt.% of the binder) for 3D concrete printing applications. The incorporation of a high volume of slag significantly improved buildability, enabling the construction of up to seven layers, attributed to the angular particle interlocking provided by slag. Furthermore, the study revealed that enhanced particle packing had a substantial positive effect on green strength, which directly influences the material's buildability and structural stability during the printing process. Rahul et al. [48] investigated phase separation during the extrusion of cementitious mortars containing 50 wt.% iron slag and highlighted the necessary addition of polycarboxylate based superplasticizer and hydroxy propyl methyl cellulose based admixtures in minimising phase separation as shown in **Figure 2.7**. Aside this, lower water to cement ratio and higher particle packing was also found to have a strong influence on desorptivity.

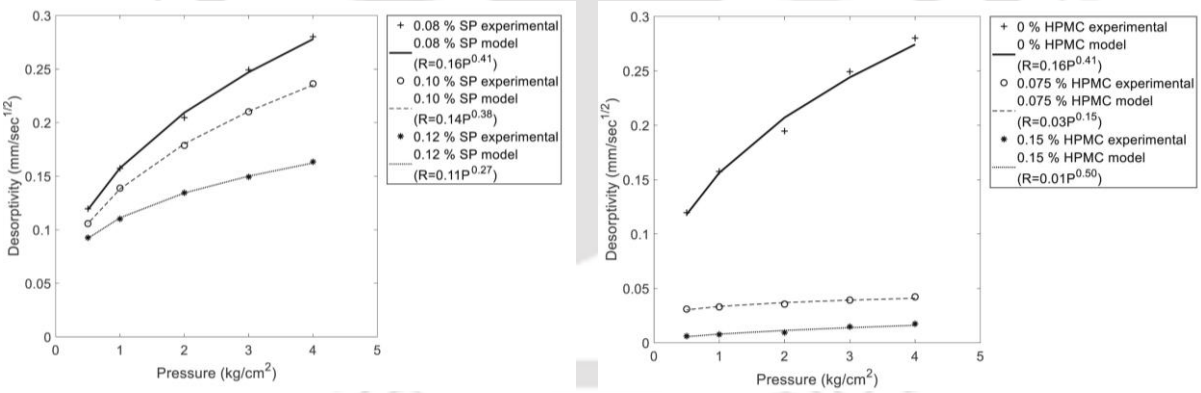

Figure 2.7 Desorptivity curve for various superplasticizer and HPMC combinations [48].

Dai et al. [50] studied the feasibility of replacement of steel slag as fine aggregate in 3DCP and find issue with its volume stability (due to free calcium and magnesium present in steel slag), which restrict its maximum replacement level up to 25%. Nekkanti et al. [51] observed the yield stress behaviour in OPC-based slag mixtures by increasing slag replacement levels, both in the freshly mixed condition and at the end of the open period. The plastic viscosity decreased

with increase in slag replacement while, plastic viscosity of mixtures at the end of open time was much lower than that of a freshly mixed mixture.

Ma et al. [52] investigated the use of copper slag (CS) as a partial replacement for cement in mixtures for 3DCP. By varying the CS content from 5% to 35%, they assessed its impact on extrusion performance and structural stability. At a low replacement level (5%), the extruded filament showed poor shape retention due to insufficient particle interlocking, which is critical for maintaining layer integrity. Increasing the CS content to 10–25% significantly improved buildability, evidenced by a higher Height-to-Width (H/W) ratio (see **Figure 2.8**). This improvement was attributed to better particle packing and interlocking, which enhanced green strength and layer stability. However, beyond 25%, excessive CS content caused gap grading issues, reducing workability and water retention while increasing internal friction during extrusion. These problems led to nozzle blockages and discontinuities, limiting practical applicability. A 25% CS replacement was identified as the optimal content, balancing buildability and extrudability. Similar findings have also been reported by [53–55] while using the CS to enhance electromagnetic and microwave absorbing properties of 3DCP.

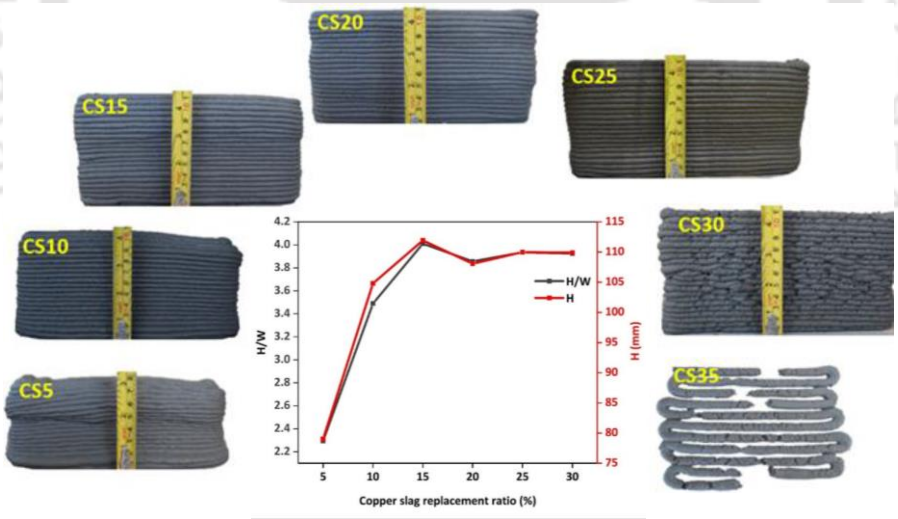

Figure 2.8 Buildability characteristics of mortar with different CS replacement ratios [52].

2.2.1.4 Recycled construction powder

Duan et al. [56] investigated the physical and chemical properties of recycled construction powder (RCP) on rheological properties of 3D printable mortars. Their findings indicate that the inclusion of RCP significantly increases the yield stress, plastic viscosity, and thixotropy of the mortar. Hou et al. [24] revealed that the incorporation of RCP (0% to 30%) into 3D

printable mortar significantly accelerates the rate of flowability loss, resulting in a substantial reduction in open time (60 minutes to 15 minutes). Furthermore, the printable mortars with RCP showed a rapid increase in penetration resistance stress over time, resulting in shorter initial and final setting times. Specifically, replacing 30% of the cement with RCP reduced the initial setting time from 6 hours to 3.2 hours and the final setting time from 8 hours to 4.6 hours. It was found that for below 10% RCP replacement ratio, the maximum stress and Young's modulus increased linearly over time. However, at higher RCP ratios (above 20%) the final properties exhibited rapid growth (see **Figure 2.9(a)),** demonstrating excellent extrudability and buildability as shown in **Figure 2.9(b)**.

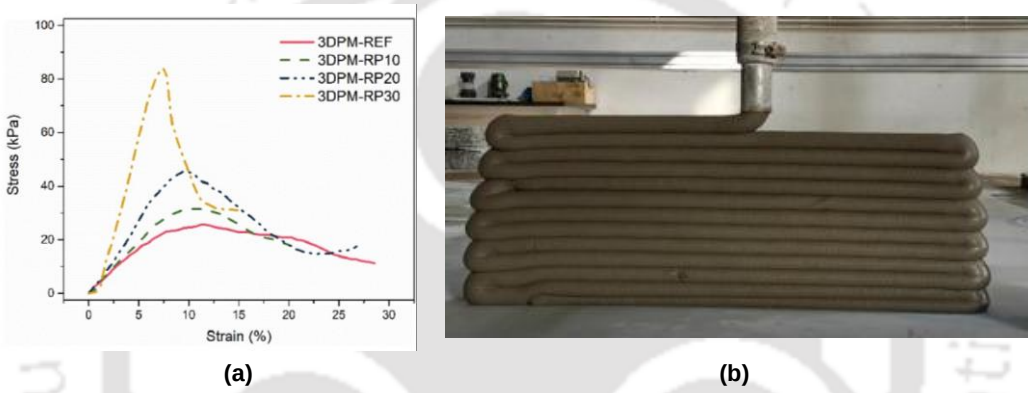

(a) (b)

Figure 2.9 (a) Stress ~ strain curve (b) printing of 3D printable mortar with RCP [24].

Qian et al. [57] studied the impact of recycled construction powder on the hardening performance of materials by optimizing the gradation of printable materials, conducting rheological tests, and initial failure height tests. Through gradation optimization, it was found that when the RCP replacement rate was 20%, the compressive strength decreased from 49.5 MPa to 44.1 MPa. Hou et al. [58] discovered that at low RCP replacement rates, the filling effect and secondary hydration characteristics of RCP reduced the proportion of harmful pores in the cement matrix, resulting in a slight improvement in the mechanical properties. However, when the replacement rate exceeded 20%, the fluidity loss rate was increased significantly, leading to weaker interlayer bonding and reduced concrete mechanical strength.

2.2.1.5 Recycled sand

Ding et al. [59] investigated the early-age performance of 3D-printed mortar by partially replacing natural sand with recycled sand at 25% and 50% ratios. The study revealed that incorporating recycled sand significantly affects the fresh mechanical properties of the mortar.

As the recycled sand content increased, the peak load capacity of the mortar also increased while the corresponding lateral deformation decreased. This indicates that higher amounts of recycled sand enhance the material's green strength and young's modulus, thereby accelerating early-age strength development and significantly improving the buildability of 3D printed structures. In terms of failure modes, the research identified two distinct patterns in mortar containing recycled sand under compression at different maturity stages (see **Figure 2.10**). In another study, Vlieger et al. [60] investigated the effects of 100% replacement of natural sand with recycled sand and found insufficient pumpability and extrudability for the new mix designs. Furthermore, the incorporation of recycled sand decreases the initial setting time of material, which is likely due to the presence of non-hydrated cement particles in the recycled sand, that lowers the water-to-cement ratio and accelerates the hydration process.

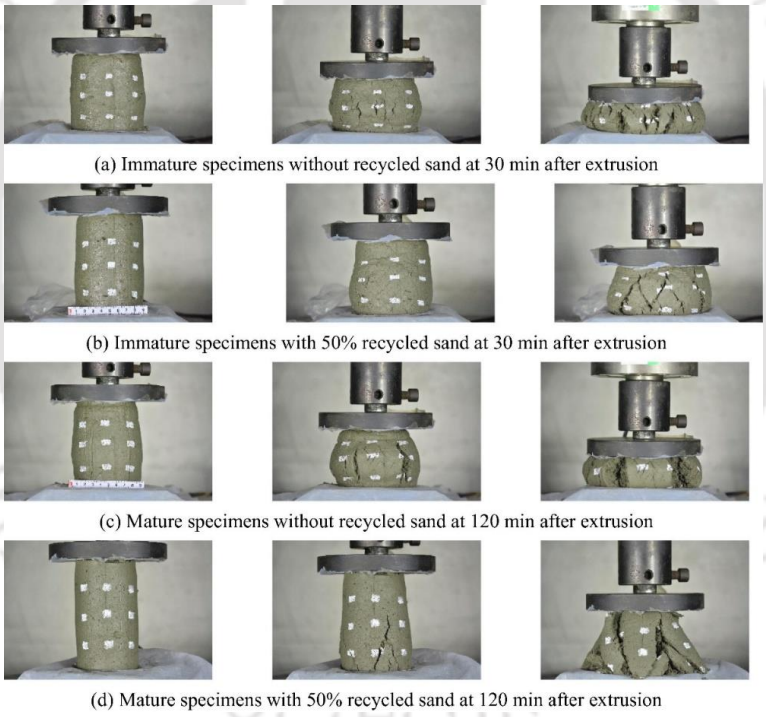

Figure 2.10 Fresh stage compression behaviour of 3D printable mixes (with and without RFA) at (a , b) 30 min and (c , d) 120 min after extrusion [59].

Zou et al. [61] also reported similar results where 100% replacement of natural sand with recycled sand not only decreases the initial fluidity of printing mortar but also increases the rate at which fluidity is lost, thereby shortening the printability window. Later, sodium gluconate was added to the printing mortar and the modified mix exhibited significantly higher green strength at early ages compared to the mortar with 100% natural sand [62].

Bai et al. [63] found that the high-water absorption rate of recycled sand improves the consistency of 3D printing mortar, making it more suitable for 3DCP applications. The porous nature of recycled sand and its inherent micro cracks facilitate the development of multiple cracks in 3DPC, which contributes to enhanced ductility property. Ding et al. [64] found high amount of unhydrated cement paste attached to recycled sand, coupled with the abundance of pores in the old cement paste and its loose microstructure, significantly reduced the density of the printed recycled mortar. In their study, the average compressive strength of 3D printed concrete with 25% recycled sand decreased by 38.4%, 54.8%, and 13.2% in the X, Y, and Z directions, respectively. The addition of recycled sand to 3D printable materials increases the amount of additional cement, ensuring that the mechanical strength does not decrease excessively, thus meeting engineering requirements.

2.2.1.6 Recycled glass

Zhou et al. [65] investigated the effects of using Recycled Ultrafine Glass Powder (UFGP) as a partial cement replacement in concrete mixtures. Their findings revealed that a 25% incorporation of UFGP led to a 27.45% increase in slump flow. This enhancement in workability was attributed to the hydrophobic and smooth surface of the glass powder, which increased the availability of free water, thereby improving lubrication between particles and reducing friction. The findings suggest that UFGP can effectively improve the fresh performance of 3D printable concrete by enhancing its flowability. Ting et al. [66] focused on the effects of varying the glass-to-binder ratio and the fineness modulus of recycled glass on filament deformation in 3DCP. The results showed that increasing the glass-to-binder ratio and decreasing the fineness modulus of RGA led to reduced filament deformation. This suggests that optimizing the proportion and particle size distribution of recycled glass can enhance the dimensional stability of 3D printed structures.

Ting et al. [67] also compared performance of mixtures containing fine river sand and recycled glass aggregates. The mixture with recycled glass exhibited lower dynamic yield stress and plastic viscosity than the river sand mixture, indicating better flow properties. However, the static yield stress was much lower for mixtures with recycled glass, potentially leading to weaker buildability. Later, Ting et al. [68] studied the application of recycled glass cullets as fine aggregates in concrete for 3DCP. It is observed that increasing the recycled glass cullet content from 25 wt.% to 100 wt.% led to a slight reduction in static yield stress. Despite this

reduction, there were no significant changes in buildability across the mixtures, with all displaying similar buildability levels. However, the overall buildability was relatively low, limited to only 8 to 9 layers (see **Figure 2.11**).

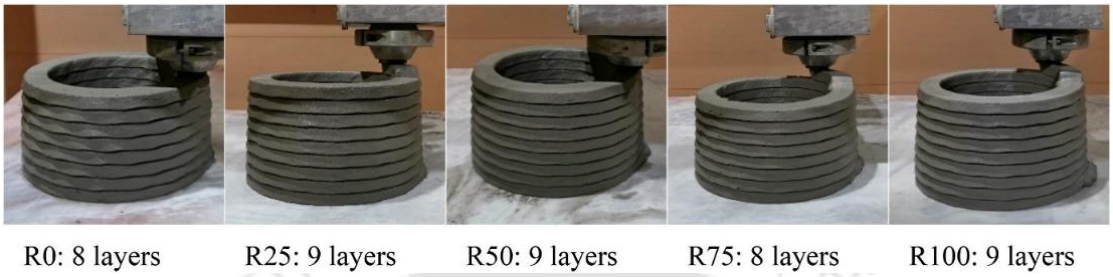

Figure 2.11 Buildability of 3D printed mortar with RGA replacement from 0% to 100% [68].

While analysing the hardened state properties, Ting et al. [68] found that the interfacial transition zone between the recycled glass particles and the binder matrix lacked adhesion owing to the smooth surface and sharp edges of the recycled glass particles [69]. Moreover, because of the hydrophobic nature of recycled glass fragments, excess water in the binder matrix can lead to segregation of the glass aggregate, further reducing the strength of concrete [70]. The compressive strength of the printed samples decreased by 20.2% to 25.8% at 100% replacement compared to control samples. Cuevas et al. [71] investigated the use of waste glass and expanded thermoplastic microspheres (ETM) as replacements for natural aggregates to enhance thermal performance in concrete. Incorporating ETM improved the thermal performance by 40% but delayed the concrete strength gain. This study underscores the challenge of optimizing both thermal and mechanical properties, highlighting the need for innovative approaches which could simultaneously increase their hydrophilicity and bonding performances.

2.2.1.7 Other plastic and rubber wastes

Novel modified concrete materials can be created by incorporating recycled plastic pellets of varying sizes and types into concrete aggregates in different proportions. In this direction, Skibicki et al. [72] explored the feasibility of modifying a mortar for 3D printing by incorporating Polyethylene Terephthalate (PET) granules as a replacement (10%, 30%, and 50% by volume) for fine aggregate. The study found that the addition of PET significantly decreased the young's modulus of the fresh mixture up to 30.1% for PET50 mixtures.

Oosthuizen et al. [73] explored the incorporation of recycled plastic waste (Resin8) as a fine aggregate replacement in 3D-printed concrete, with replacement levels ranging from 5% to 15%. The addition of Resin8 reduced static and dynamic yield stresses, mitigating the thixotropic behavior but negatively affecting buildability. In the hardened state, Resin8 enhanced interlayer bonding due to its hydrophobic nature, which increased surface moisture in interlayer regions, thereby reducing interlayer porosity and improving bond strength.

Sambucci et al. [74] converted waste tires into coarse rubber granules (RG, 2-4 mm) and fine rubber powder (RP, less than 1 mm), incorporated these rubber particles into concrete to replace natural aggregates, and studied the mechanical properties of 3D-printed rubber concrete. They found that when river sand was replaced by rubber powder at 50 and 100 vol%, the compressive strength decreased by 65% and 77%, respectively, owing to weaker filler-matrix adhesion and reduced material density. Through four-point bending tests, they observed that at the same replacement levels, the flexural strength decreased by 30% and 67%, respectively. In another study, Sambucci et al. [75] further demonstrated that despite the reduction in mechanical strength, adding rubber particles to 3D-printed concrete positively affected the ductility, sound insulation, and thermal insulation properties. The partial replacement of natural aggregates with rubber aggregates led to a reduction in the mechanical strength of the hardened material because of the decreased overall density and cement filler adhesion. These studies emphasize the trade-off between thermal and mechanical properties in sustainable material design as shown in **Figure 2.12**.

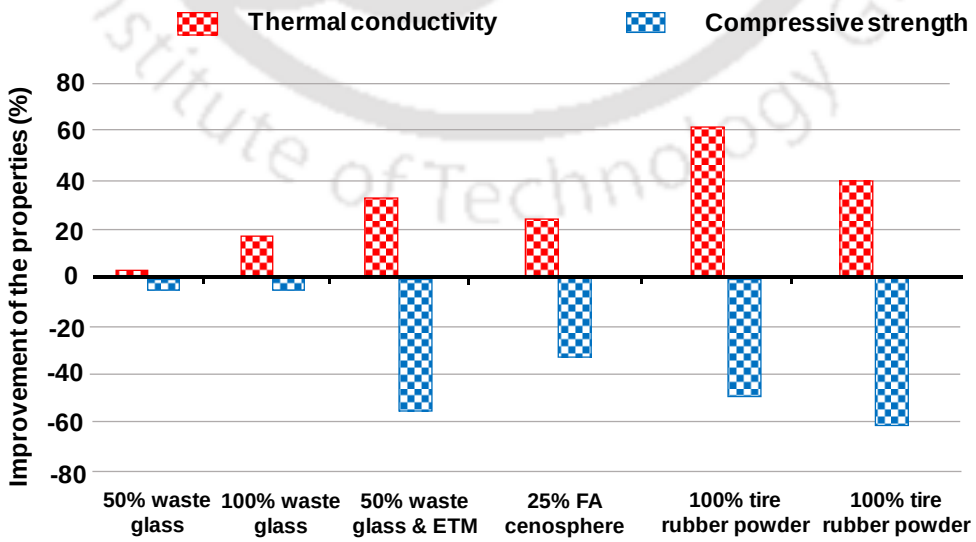

Figure 2.12 Thermomechanical properties of 3DCP mixes incorporating different industrial wastes [76].

2.2.1.8 Iron and copper tailings

Ma et al. [77] conducted an in-depth study on the material optimization for 3DCP by replacing natural sand with copper tailings. Their study focused on the impact of copper tailings' finer particle size on the flowability and buildability of the printed paste. As the copper tailings ratio increased, flowability improved. However, this also led to a decrease in buildability, with lower penetration resistance and height-to-width ratios. The study identified mix R30 (see **Figure 2.13**), with a 0.26 water-binder ratio and a 3:2 sand-to-tailings ratio, as the most optimal for freeform 3D printing. This mix included 70% cement, 20% fly ash, and 10% silica fume, alongside micro polypropylene fibers and superplasticizer for improved workability. Despite these advantages, printed samples exhibited 31.4% lower flexural strength and 36.3% lower deflection resistance than cast counterparts, highlighting a potential trade-off between printability and mechanical performance.

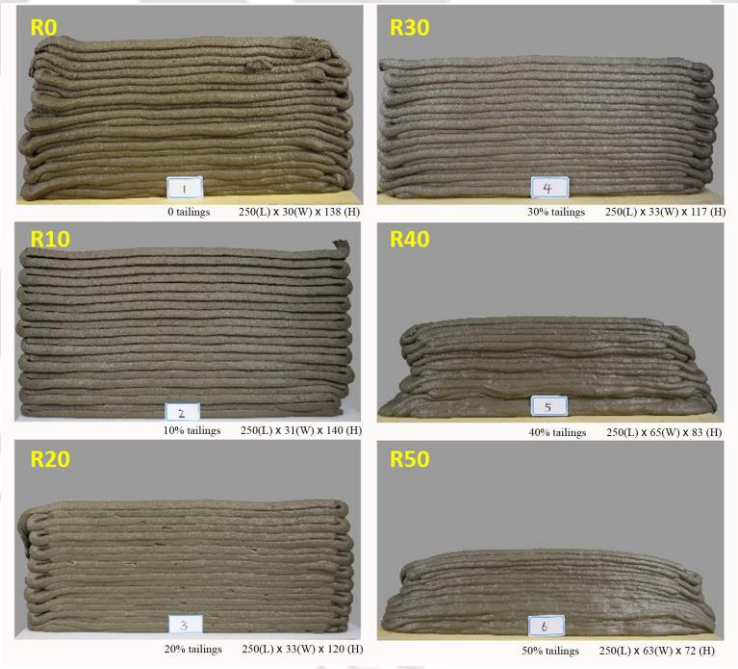

Figure 2.13 Buildability test result with different copper tailing dosages [77].

Li et al. [78] studied the development of 3D printable building materials using a combination of copper tailings and iron tailings. Their findings indicated that replacing iron tailings with copper tailings reduced the fluidity and accelerated the setting times of the material due to the finer particle size of copper tailings. Among various trials, the optimal performance was achieved with an iron-to-copper tailings ratio of 4:1, yielding a 28-day flexural strength of 8.2

MPa and compressive strength of 45.2 MPa. This mix also demonstrated desirable fluidity (197.5 mm) and setting times (50 min for initial and 82 min for final), making it suitable for 3D printing applications. The primary hydration products, including calcium silicate hydrate (C-S-H) gels and ettringite, were found to significantly contribute to the material's strength development. Microscopic analysis further revealed that the ettringite crystals formed a web-like structure within the matrix, enhancing the mechanical properties of the 3D printable material.

2.3 Mechanical and thermal performance of 3DCP structures

The increasing focus on sustainable construction, driven by the flexibility offered by freeform design, has led to the widespread adoption of lightweight 3D-printed concrete structures across the globe [79]. A critical design feature in these structures is infilled lattice architecture, which are primarily subjected to mechanical and thermal loading conditions as shown in **Figure 2.14**. The performance of these structures under such conditions is closely tied to factors such as the geometry of the lattice, infill density, and the properties of the materials used. The following sub-sections will provide a review of both experimental and numerical approaches for analyzing mechanical and thermal behavior of 3DCP structures.

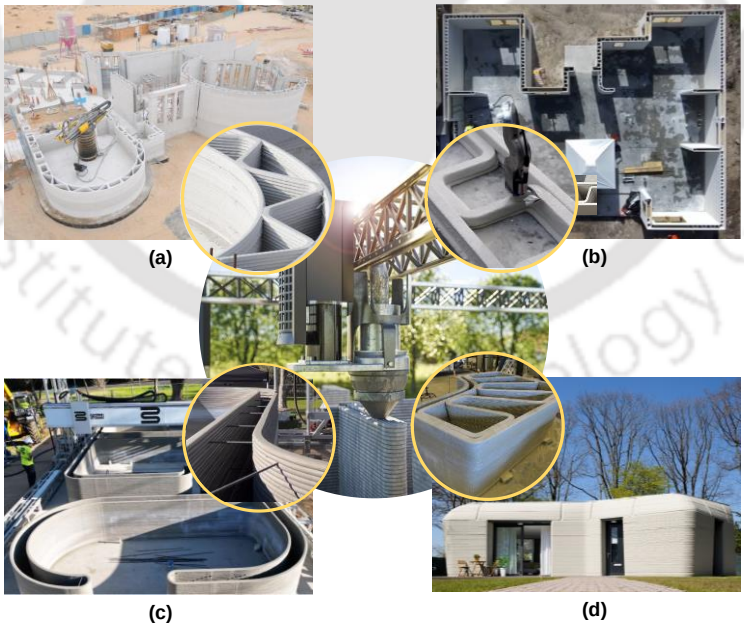

Figure 2.14 Examples of 3D printed housing projects with (structural/ load-bearing) lattice wall Reference: (a) World's largest 3D-printed office building of Dubai Municipality by Apis cor [80], (b) 3D printed model house in Melbourne by Apis cor [81], (c) Austral Australia's first 3D printed amenities block in New south wales by Contour 3D [82], (d) first habitable 3D printed concrete house in Netherland [83].

2.3.1 Mechanical performance

Wang et al. [84] investigated flexural behavior of the 3D-printed concrete beams with various hollow topologies, including cellular, triangular, truss, and lattice designs. From different topologies; cellular beams showed cracks along loading and support points, attributed to shear stress, while other topologies exhibited mid-span cracks caused by tensile stresses (see **Figure 2.15**). The study highlighted that cracks typically initiate at the filament-to-edge contact points. It also revealed distinct brittle failure modes across all structures due to the absence of reinforcement. Among the topologies, truss-shaped beams exhibited the highest tensile strain (137 με) and deflection (0.86 mm), indicating the lowest bending deformation resistance. In contrast, lattice beams demonstrated the smallest strain (90 με) and deflection (0.51 mm), offering superior flexural deformation resistance. However, it is to be noted that authors have used lightweight concrete mix (incorporating very fine silica sand and ceramsite sand) in this study, which poses strength limitations for many practical applications.

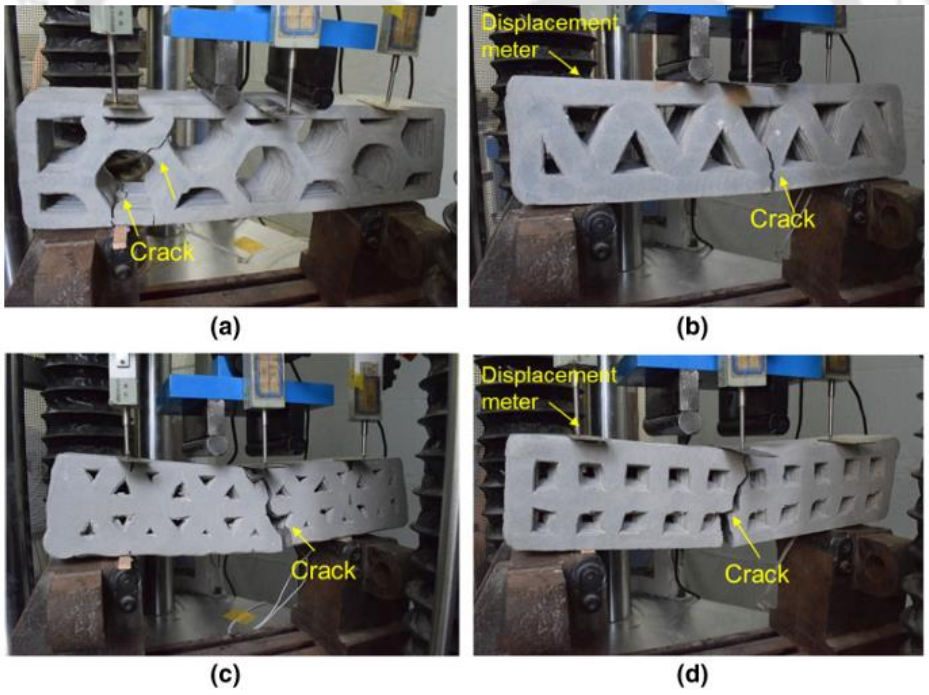

Figure 2.15 Failure modes of (a) cellular, (b) triangular (c) truss-shaped, and (d) lattice hollow 3D-printed structures [84].

Bai et al. [85] investigated the structural performance of topology-optimized 3D-printed ultra-high-performance concrete (3DP-UHPC) skeleton forms through four-point bending tests on various beam configurations. These included 3DP-UHPC skeleton composite reinforced

concrete beams (CRC), rebars locally reinforced CRC beams (R-CRC), rebars locally reinforced 3D printed concrete beams (R-PC), and conventional reinforced concrete beams (RC) as benchmarks. The results indicated that CRC and R-PC achieved only 25% and 50% of the flexural capacity of RC, respectively, with sudden failures highlighting their limited structural performance. In contrast, R-CRC exhibited significantly higher stiffness and strength, demonstrating its potential as an effective alternative to conventional reinforcement cages (see **Figure 2.16**). This approach enhances load-bearing capacity while maintaining 3D printing flexibility. The study also introduced a novel load transfer mechanism, where the 3DP-UHPC skeleton and rebars at the beam bottom bear the load, while normal concrete (NC) disperses internal forces and improves stiffness. However, further research is needed to explore the intricate stress dynamics, shear behavior, and broader load-bearing properties of this innovative design.

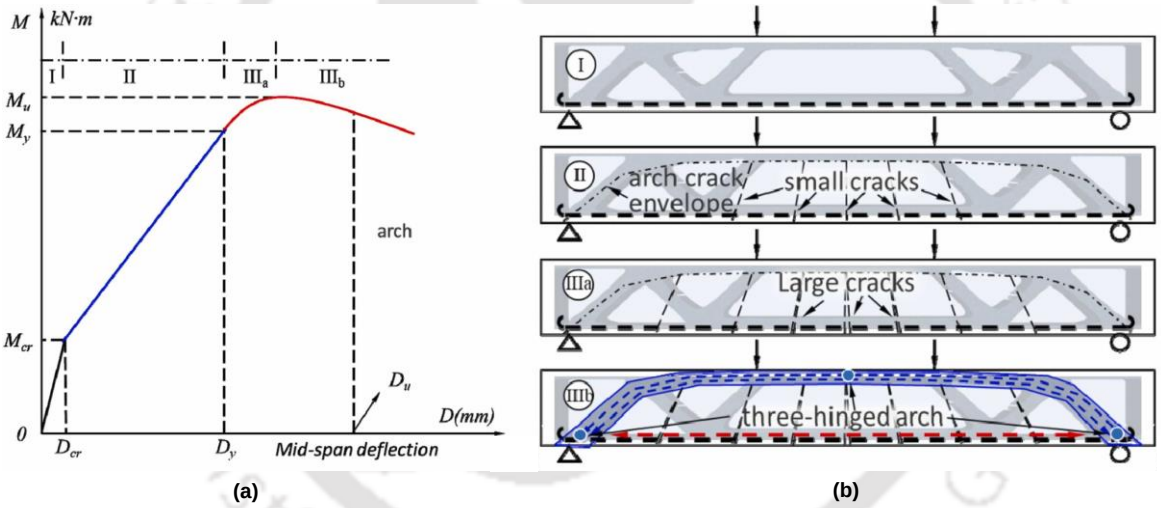

Figure 2.16 (a) Representative load-bearing stages and (b) typical crack patterns observed at each stage of the R-CRC beam [85].

Nair et al. [86] explored the impact of layer height on rheology, print quality, interlayer bonding, and mechanical properties of 3D-printed beams. Layer heights of 5, 10, and 15 mm, corresponding to 25%, 50%, and 75% of a 20 mm nozzle diameter, were examined. The findings revealed that smaller layer heights enhanced flexural strength and fracture properties in both unreinforced and fiber-reinforced mortars, despite increasing the number of interfaces and extending printing time. The addition of steel fibers effectively addressed the weaknesses at interfaces, resulting in 30–40% higher flexural strength and approximately 30%

improvement in fracture toughness and crack resistance compared to plain mixtures, thereby ensuring superior bulk properties.

Asprone et al. [87] proposed a different method for fabricating reinforced concrete (RC) members using 3D printing technology. The technique involves partitioning RC members into distinct concrete segments that are individually 3D printed and subsequently assembled with a steel reinforcement system. This approach facilitates the production of free-form, structurally optimized RC elements while minimizing concrete usage and reducing structural weight. A case study details the material characterization, fabrication process, and full-scale three-point bending test of a 3.0 m-long straight RC beam (see **Figure 2.17**), alongside the demonstration of a free-form variable cross-section RC beam to showcase its versatility. A finite element model was developed to analyze the flexural response of the printed beam, revealing that interfaces and connections play a critical role in stress distribution under loading. The findings indicate that the printed RC beam's initial flexural stiffness is comparable to a conventional solid RC beam. However, local failure mechanisms, such as shear damage at segment interfaces and anchoring issues, affect its nonlinear flexural behavior, resulting in large deflections without steel yielding. The authors suggest further testing to address critical issues, including interface behavior, overall ductility, size effects, and thermal/fire resistance.

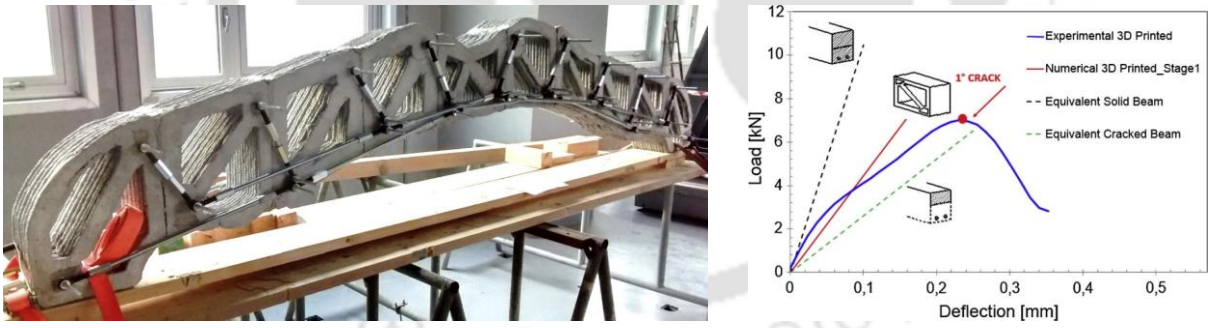

(a) **(b)**

Figure 2.17 (a) 3D-printed RC beam featuring a variable cross-section; (b) Experimental and numerical load-deflection curves [87].

An innovative approach combining engineered cementitious composites (ECC) and recycled fine aggregate concrete was introduced to overcome challenges in embedding steel reinforcement within 3DCP [88]. In this study, flexural performance tests were conducted on 3D-printed composite beams with varying ECC heights (15, 30, and 45 mm) and shear-span

ratios (2.0, 2.5, and 3.0). The results demonstrated 3D printed beams with ECC heights of 30 and 45 mm achieved load-bearing capacities comparable to reinforced concrete beams with longitudinal reinforcement ratios of 0.2%. A finite element model incorporating the effects of printed interfaces was developed to further examine the role of interfacial bond strength, ECC height, and ECC strength on flexural behavior. While increases in ECC height and strength improved load-bearing capacity, the study identified that the bond strength of printed interfaces could act as a limiting factor in realizing these enhancements.

Feng et al. [89] explored the effect of printing directions on load-bearing capacity of the 3DCP structures using the ultimate stress criterion model, while Freek et al. [90] applied a plastic damage model to analyze the ductile behavior of fiber-reinforced 3D-printed concrete beams. Wang et al. [84] simulated failure mechanisms of 3DCP objects through the discrete element method. While these approaches enhance understanding, limitations remain in accurately simulating multifaceted failures, such as crack propagation and anisotropic behavior. In order to consider multi-surface limit functions for capturing the failure of cementitious materials, Zijl et al. [91] proposed a method by using the anisotropic Rankine yield criterion. Later, Heever et al. [92,93] developed a plasticity continuum crack model to capture the anisotropic inelastic behavior of fiber-reinforced 3DPC objects, in which the anisotropic Rankine-Hill theory can portray the hardening/softening characteristics. However, the above-mentioned approaches are only applied to planar (2D) problems, where the influence of the out-of-plane direction was not considered.

2.3.2 Thermal performance

The thermal performance of 3D-printed building components lies in the intersection of material properties, lattice wall designs, and printing process as mentioned in section 2.2.1. Recent studies [94,95] have explored the thermal behavior of 3D-printed lattice wall configurations through experimental and numerical investigations. Ramakrishna et al. [96] investigated thermal behaviour of three type of 3D printed panels such as solid-core, hollow-core, and hollow-core insulated by analyzing their behavior under infrared irradiance in simulated test rooms condition (see **Figure 2.18**). Authors reported that the solid-core panels demonstrated superior thermal regulation, maintaining the lowest indoor air temperature (33.0°C) due to their high thermal energy storage capacity (4300 kJ/m²). This was attributed to their dense structure and minimal void content, which allowed efficient heat absorption and limited thermal

transmission. In contrast, hollow-core panels exhibited higher thermal inertia and reduced energy storage (1730 kJ/m²) because of their lower thermal mass. Hollow-core insulated panels, enhanced with polyurethane foam, slightly improved thermal energy storage and demonstrated sustained thermal inertia, reaching a peak temperature difference of 14.7°C between interior and exterior surfaces. The findings highlight the trade-offs between thermal insulation and energy storage in 3D-printed elements.

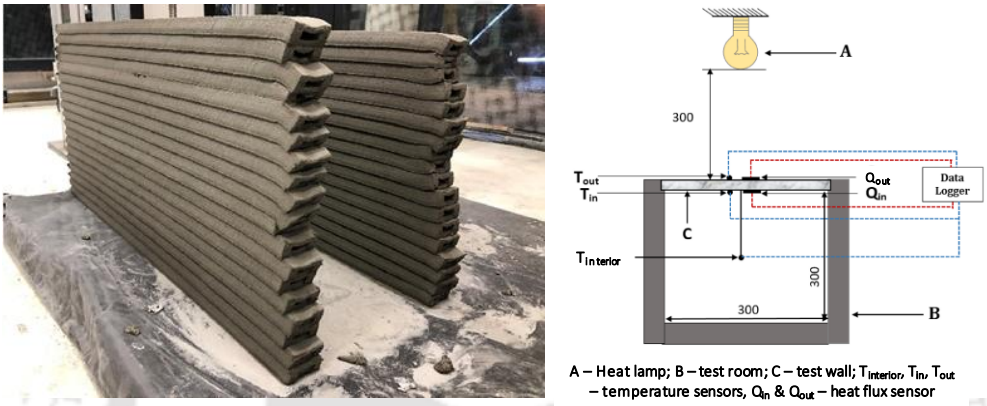

Figure 2.18 (a) Hollow core printed layers (b) simulated test room test set up [96].

Christen et al. [97] conducted thermal testing on a 3D-printed facade section installed on the roof of Stellenbosch University, for the collection of real-time data on solar flux, ambient temperature, and wind speed for detailed interpretation (see **Figure 2.19**). To address such transient thermal problems numerically, Marais et al. [98] predicted the internal surface temperature of a 3DCP wall, recommending the integration of a greater number of smaller-width cavities within the wall. The authors of [99] further refined and validated their numerical model to assess the impact of varying phase change material (PCM) melting temperatures and different facade surface colors across different seasons in Stellenbosch. The analysis highlighted the significant influence of darker/white surface colors on solar radiation absorption, emphasizing the importance of tailoring PCM melting temperatures to optimize seasonal performance. For climates with substantial seasonal temperature variations, using PCMs with dual melting temperatures (e.g., 18°C for winter and 28°C for summer) proved to be highly effective. The study also underscored the need for accurate modeling of cavity convection and radiation, along with iterative simulations of internal ambient temperatures, to ensure realistic and reliable predictions.

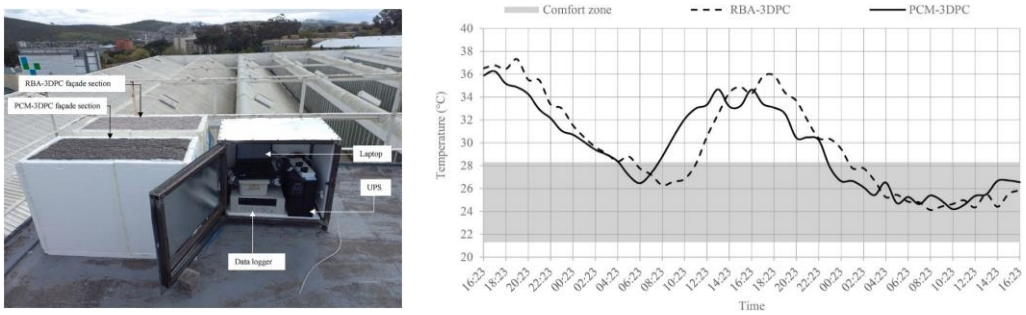

(a) (b)

Figure 2.19 (a) Transient thermal test set up exposed to open climate, and (b) inside surface temperature variation at different time interval of a day [97].

Nevertheless, due to high sensitivity of transient thermal analysis to input climatic conditions and specimen size, steady state thermal condition is commonly used by the researchers [100]. Alkhalidi et al. [101] calculated the U value of wall with triangular cavities using steady state simulation by varying the wall thickness from 0.22 m to 0.58 m (see **Figure 2.20**). Simulated results indicate that U value of binder jet printed wall (made from bound sand material) can reach up to a value of 0.15 W/m^{2}K with increasing in thickness and filling insulation material inside the cavities. In a similar study, Ravula et al. [102] proposed a unified equation to estimate the U-values for 3DPC wall panels with varying insulation infill. Nemova et al. [103] developed a customized climatic chamber to calculate the U values of infill structures such as triangular, rectangular and hexagonal shape and found that experimental results verily differ (~30%) from the numerical prediction as the uneven cavity convection was not considered in the experimental U-value calculation.

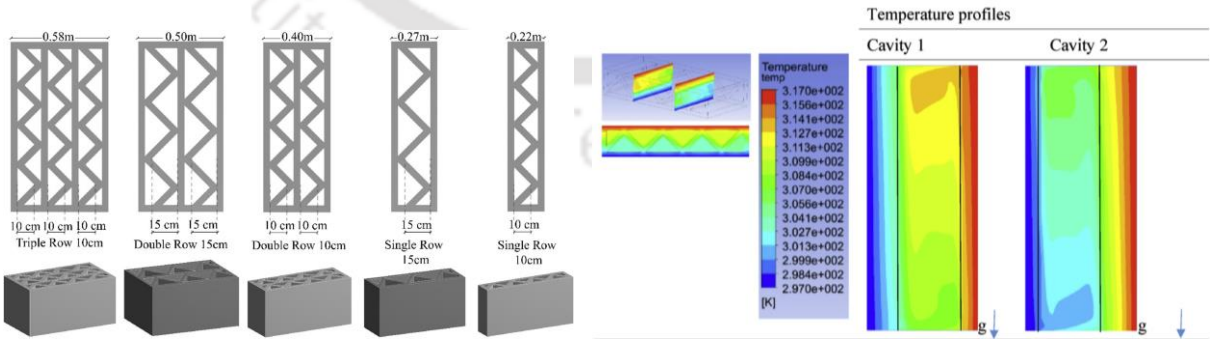

(a) (b)

Figure 2.20 (a) Various cavity configuration considered for the numerical simulation and (b) their temperature distribution plot [101].

Suntharalingam et al. [104] proposed a finite element model (FEM) considering hollow cavity as air layer for different lattice wall configurations as shown in **Figure 2.21**. In comparison to other walls, higher performance was observed for the triangular and sinusoid shaped cavity wall with double row configuration. Briels et al. [105] investigated the thermal performance of a 3DCP wall with an internal cellular structure using both experimental (heat flux measurements test set up) and numerical simulations (via THERM, a finite element-based solver). The 2D and 3D heat transfer models were validated against the experimental data with 25% s. deviation. This discrepancy was attributed to printing irregularities (drying-induced cracks) and assuming 'static surface coefficient' for radiation and convection in the numerical model.

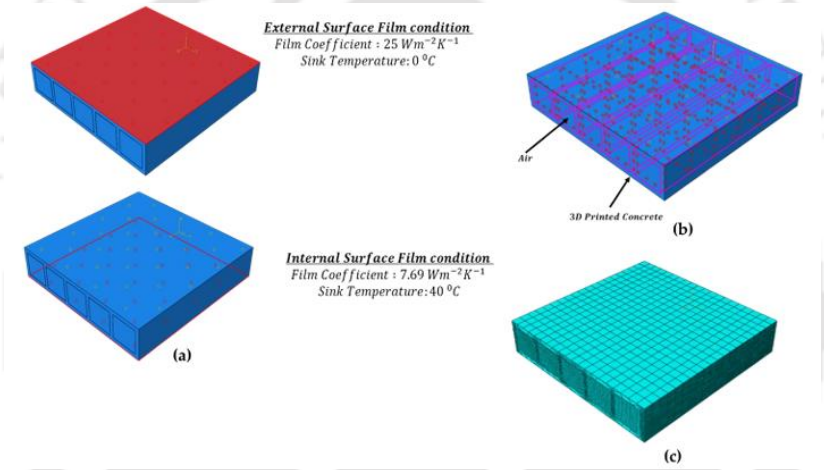

Figure 2.21 Schematic of boundary condition used in finite element study [104].

In another study, Dziura et al. [106] used FEM simulations and scale down experimental testing to evaluate the thermal performance of 3DP cavity walls. According to the results, simulated and experimental U-value differed by 61% and 23% respectively, depending on wall geometric configurations. This discrepancy underscores the need for full-scale experimental setup and formulation of robust numerical model for accurate prediction of thermal properties. It was found that the heat transfer models used in FE simulation studies [104,107,108] were often oversimplified, highlighting the computational challenges associated with conjugate heat transfer for lattice walls or real components/structures. Although Alkhalidi et al. [101] employed a CFD model, the authors did not discuss the temperature and velocity distribution inside the lattice cavity. Thus, developing a comprehensive CFD model to explore thermal performance of 3DCP structures requires overcoming these computational hurdles.

2.4 Summary

Chapter 2 presents a detailed overview of the fundamental aspects of extrusion-based concrete 3D printing, with particular emphasis on material selection, sustainable integration of industrial by-products, and the mechanical and thermal behavior of printed lattice structures. Beginning with an overview of extrusion-based 3DCP technology, the chapter highlights its advantages over conventional construction methods, such as eliminating formwork and enabling complex geometries, while noting the unique challenges related to the time-dependent rheological properties required for successful printing. The discussion on material requirements focuses on balancing fresh-state properties—including extrudability, shape retention, and buildability—across various stages of the printing process. While sustainable substitutes like slag and fly ash offer environmental benefits by reducing reliance on natural resources, their influence on material behavior during printing necessitates careful optimization. A significant portion of the chapter is then dedicated to review the mechanical strength and thermal performance of diverse lattice infill patterns used in 3DCP components. It articulates how lattice design critically affects structural integrity and energy efficiency, underscoring the potential for optimized material use without compromising performance. Distinct lattice geometries exhibit varied capabilities in load distribution and thermal insulation, which are essential considerations for advancing energy-efficient and resilient construction practices.

Nonetheless, several important knowledge gaps remain to be addressed. In particular, a comprehensive understanding of how new raw materials, such as Portland slag cement and slag sand, influence both fresh and hardened properties critical to reliable 3D printing is still lacking, including their economic and environmental sustainability. Moreover, while the mechanical and thermal behavior of lattice structures has been explored primarily at the material or small-scale level, there is a pronounced lack of studies investigating these effects at the full component scale. This highlights the need for extensive large-scale experimental validation and the development of novel hybrid lattice designs to enhance performance for practical applications. The following chapters of this thesis aim to address these gaps through systematic experimental investigations and simulation-based analyses focused on optimizing material sustainability and lattice infill configurations, thereby advancing the applicability of extrusion-based 3D concrete printing in modern construction.

CHAPTER 3

Influence of Portland slag cement and slag sand on sustainability and performance of 3D printable mortar

This chapter aims to develop slag-based 3D printable mixes with detailed investigation on the effects of (i) substitution of river sand with slag sand (ii) substitution of OPC with slag cement, and (iii) combined effect of both slag sand and cement to enhance the sustainability and 3D printability of the mixes. Specifically, the research focuses on analysing the fresh, mechanical and thermal properties, along with carbon sequestration capability. By comparing these parameters with those of conventional cement (PC)-based mixes, the study seeks to provide insights into the viability of slag-based materials in extrusion based concrete printing applications.

A portion of this chapter has been published in:

D. Dey, B. Panda, J. Kole, M. Rastogi. 2025. Printable cementitious composition and preparation method thereof. Indian Patent, filed May 15, 2025. Patent filed. Patent Application No.: 202531046998 (PUBLISHED)**.**

3.1 Introduction

Steel industry by-products, such as GGBFS or iron slag (called as slag in the rest of the text here), present a promising opportunity for the development of sustainable construction materials. Although 3D printing technology is gaining momentum, the potential of slag cement and slag sand in 3DCP is unknown. There is a dearth of investigation into the rheological and mechanical properties of such mixes that contribute to 3D printability. This chapter aims to investigate the effects of slag cement and slag sand, added to substitute (100% replacement) natural sand and OPC on rheological properties, flow, and green strength necessary for extrudability and buildability. The synergistic influences of slag cement and sand on yield stress, plastic viscosity, and shape retention, and their impact on buildability are experimentally determined. The experimental program is designed to advance scientific and technological research into the effect of 3D printing, mechanical, thermal properties and curing conditions, including normal curing (moist + dry curing) and accelerated carbonation curing.

3.2 Materials and methods

3.2.1 Materials

The primary binders used in this investigation were OPC confirming to IS 269:2015 specifications and Portland slag cement (PSC) manufactured by JSW Cement Ltd. India. PSC is a blended cement that is manufactured by intergrading Portland clinker with ground granulated blast-furnace slag (GGBFS percentage addition: 52 ± 2 %) as per IS 455:2015. The physical characteristics, morphological characteristics, chemical composition and particle size distribution (PSD) of OPC and PSC are shown in **Table 3.1**, **Figure 3.1**, **Table 3.2** and **Figure 3.2** respectively.

Table 3.1 Physical characteristics of OPC and PSC.

Type of cement sample	Fineness (m^2/kg)	Specific gravity	Setting time (min)		Soundness	
			Initial	Final	Le-chatelier (mm)	Auto Clave (%)
OPC (43 grade)	288	3.15	140	220	2.000	0.190
PSC (43 grade)	373	2.91	165	275	0.500	0.025

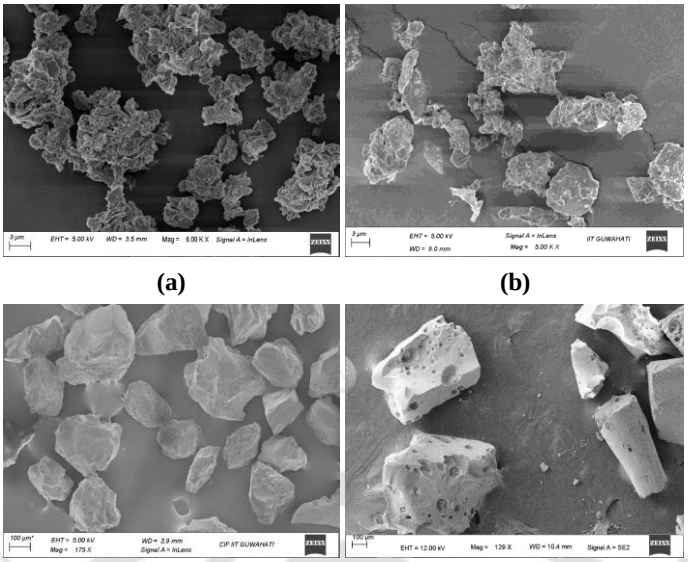

Figure 3.1 Morphological image of (a) OPC, (b) PSC, (c) RS, (d) SS.

Table 3.2 Chemical composition of raw materials.

Raw material	CaO	SiO_2	Al_2O_3	Fe_2O_3	MgO	SO_3	Na_2O	K_2O	*LOI (%)
OPC	65.93	16.54	4.25	4.56	3.65	3.13	0.06	0.52	1.33
PSC	48.90	25.52	13.14	2.71	5.10	2.16	0.19	0.82	1.42
RS	0.63	88.10	2.23	4.66	1.03	-	1.2	0.50	1.52
SS	42.17	31.26	16.70	2.16	4.96	1.7	0.33	0.64	2.01

* LOI: Loss on ignition

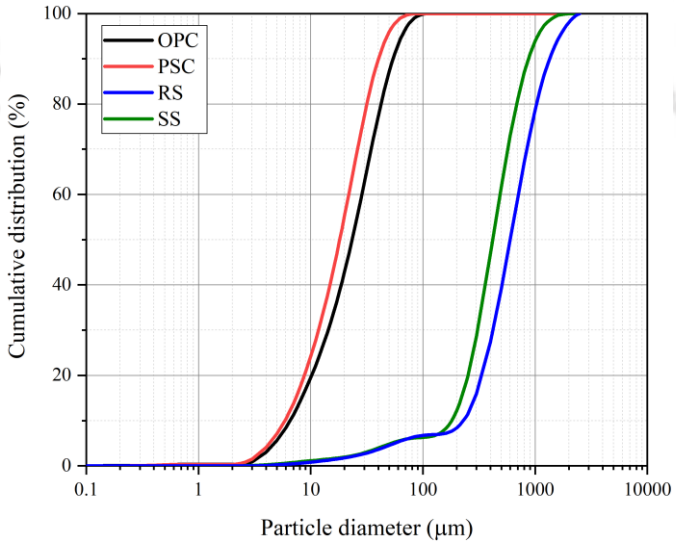

Figure 3.2 Particle size distribution of OPC, PSC, RS and SS.

Natural river sand (RS), conforming to IS 383:2016, was used as fine aggregate in control mix. Processed granulated blast furnace slag, also known as slag sand (SS), was used as substitute of the RS. The physical properties (**Table 3.3**), chemical composition (**Table 3.2**), morphological (**Figure 3.1**) analysis, particle size distribution (**Figure 3.2**), and microstructural characteristics (**Figure 3.3**) of both RS and slag sands were analyzed for understanding their influences in 3DCP.

Table 3.3 Physical properties of RS and SS.

Properties	River Sand	Slag Sand
Bulk density (kg/m^3)	1423	1350
Specific gravity	2.66	2.71
Compact porosity (%)	46.5	50.18
Fineness modulus	2.72	2.40
Water absorption (% mass)	1.07	5.84

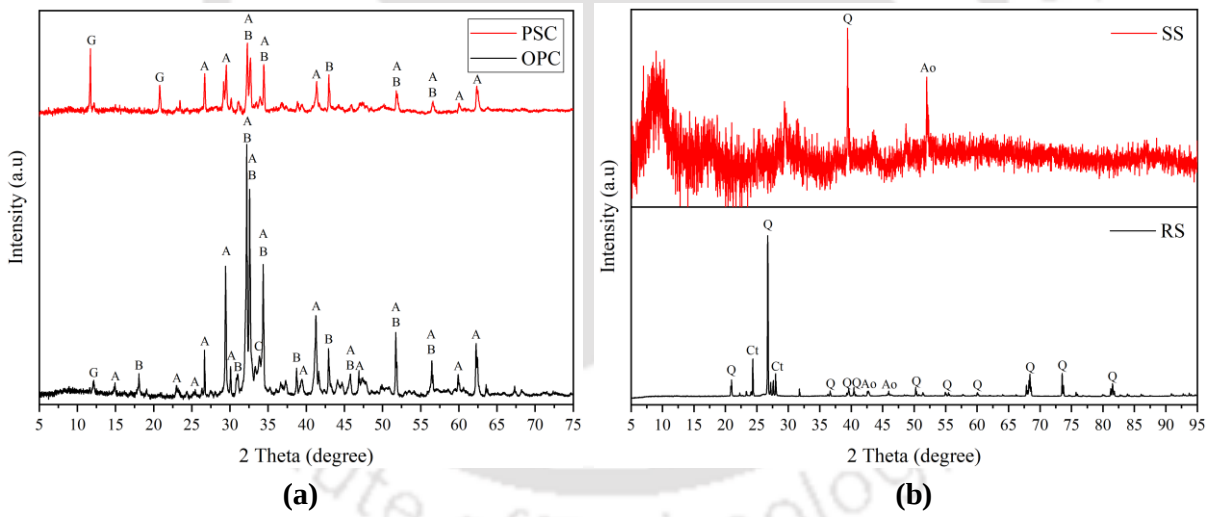

(a) **(b)**

Figure 3.3 X ray diffraction of (a) OPC and PSC, (b) RS and SS (Legend: Alite(A), Aluminum oxide (Ao), Belite (B), Celite (C), Graphite (G), Quartz(Q)).

3.2.2 Mix proportions and 3D printing

Table 3.4 shows the mix compositions investigated in this research. The selection of basic mix parameters such as the sand-to-binder and water-to-binder ratios was based on existing literature relevant to 3D printable mortars [109]. To tune the rheology of the mix amenable for printing, a non-ionic cellulose ether-based powder, Hydroxypropyl Methyl Cellulose (HPMC),

was incorporated as a viscosity-modifying admixture. Additionally, a polycarboxylate ether (PCE) based superplasticizer (SP) in powder form was used as a high-range water-reducing agent, with a bulk density of 600 ± 50 g/L. The dosage of SP was carefully adjusted in each mix design to maintain a constant flow of 185 mm, facilitating ease of pumping, extrusion, and comparative analysis of fresh-state characteristics. OR contains a mix of OPC, RS, and chemical admixtures. In PR and PS, 100 wt.% of OPC is replaced by PSC, while in OS, 100 wt.% of RS is replaced by SS.

Table 3.4 Mix design details in kg/m^3

Mix ID	OPC	PSC	RS	SS	Water	PCE	HPMC
OR (OPC+RS)	1002.70	-	1002.70	-	362.50	1.20	1.00
OS (OPC+SS)	996.10	-	-	996.10	360.10	1.24	0.99
PR (PSC+RS)	-	987.80	987.80	-	357.10	1.09	0.99
PS (PSC+SS)	-	981.40	-	981.40	354.80	1.13	0.98

All ingredients were initially dry mixed in a rotating drum-type concrete pan mixer for 2 minutes. Subsequently, water was introduced into the rotating drum at 3-minute intervals over a period of 12 minutes to achieve a homogeneous mixture. The mortar mixes were printed using a gantry-based 3D printer with a build volume of 1 m × 1 m × 0.9 m. The extruder was connected to a concrete pump (MAI®2PUMP PICTOR) via a 3-meter hose, delivering the mixes at a rate of 2.54 litres per minute. A stand-off distance of 10 mm was set, while constant print speed of 60 mm/s and layer width of 30 mm were selected to enhance layer stability and inter-layer adhesion.

3.2.3 Fresh state characterization

3.2.3.1 Extrudability, buildability and open time test

The extrudability and shape retention characteristics of the mixes were assessed by printing single-layer filament of 0.5-meter length at 10-minute interval, until visible surface cracks appeared in the extruded filament. Similar test methods have been previously used by researchers [110,111], where shape retention factor (SRF) was calculated by capturing high-resolution images using a digital camera under natural lighting conditions. The captured images

were analyzed using the ImageJ software package for printed filament width. The average width of the printed layer (W_p, mm) was divided by the modeled input width (W_m= 30 mm) to calculate the SRF. Based on the SRF value and print quality, open time of the mixes was evaluated. The developed mortar mixes were used for printing a hollow cylinder of radius 200 mm. The buildability was determined based on the number of layers that could be printed without collapse.

3.2.3.2 Rheological test

The rheological properties of the fresh 3D printable mixes were analysed using a commercial rheometer (ICAR plus) with four vane blade configurations. A batch mixing of 50 litres concrete was prepared; 15 litre mix was placed into the rheometer cell and 35 litre mix was used for the printing trials. Rheological parameters are strongly influenced by the shear history and flocculation state of the material. Therefore, the rheology test of all mixes was conducted simultaneously with the 3D printing to yield comparable time-dependent structuration properties.

The first step towards rheological characterisation is to replicate the printing-induced shearing via a rheometer. The material first experience shearing during pumping followed by material extrusion and printing action. Based on the aforementioned pump speed and hose length, the rheometer was first operated at 0.2 revolutions per second for 60 second to mimic the pump induced shearing. The shear rate of the rheometer was then lowered down to 0.1 revolutions per second and was operated up to the time (20 second) when peak torque gets stabilized with respect to the shear time. Such constant shearing test also known as stress growth test was operated at different time intervals (0 min, 2 min, 4 min, 6 min, 8 min, 10 min, 20 min, 30 min, 40 min, 50 min) to understand the time dependent rheology of the material and was subsequently correlated to the bilinear thixotropic model as proposed by Kruger et al [112].

3.2.3.3 Green Strength test

"Green strength" and stress-strain behaviours of fresh 3D printable mixes influence the stability of the printed structure under its self-weight. To understand the load bearing capacity, unconfined compressive test of freshly prepared mortar mixes was performed similar to ASTM D2166 [113]. In this test, a cylindrical specimen of 50 mm diameter and 100 mm height was prepared from a 3D printed plastic mould. Teflon was coated inside the mould to prevent adhesion between mould and specimen. Loading rate of 30 mm/min was selected so that each

test could be finish within 2–3 min to neglect effects of thixotropic build-up. The green strength tests were conducted up to 40% vertical strain for different rest time of t = 30, 60, and 90 min from the start of mortar extrusion. The overall deflection and load-displacement graph for all mixes were recorded by using a high-definition camera for further analysis.

3.2.4 Hardened state characterization

For the hardened state characterization, slabs of size 300 mm (l) × 300 mm (w) × 80 mm (h) were printed with the same printing parameter as discussed for fresh state characterization tests. These beams and slabs were printed and water cured for standard 28 days before the testing. Samples of different sizes were extracted from these printed beams and slabs as per the test requirement.

3.2.4.1 Compressive and flexural test

A servo-controlled hydraulic universal testing machine (BiSS ® 250kN capacity) was used for mechanical strength testing in which the specimens were subjected to loading at a constant displacement rate of 1 mm/min following the guidelines of ASTMC109 and ASTM C348 for compressive and flexural testing respectively. For each mix, a total of 9 cubic specimens with dimensions of 50 mm × 50 mm × 50 mm were extracted for compressive testing, while 9 prism specimens measuring 160 mm × 40 mm × 40 mm were extracted for flexural testing. The 3D-printed specimens were tested under three perpendicular loading directions as shown in **Figure 3.4**. Furthermore, the anisotropic coefficient (I_{3D}) of printed specimens was determined using the empirical formula (**equation 1**), where anisotropic coefficients in different directions (I_{Pr}, I_{Lo}, and I_{La}) are provided as per **equation 2** [114].

$$I_{3D} = (I_{Pr} + I_{Lo} + I_{La})/3 \quad (1)$$

$$I_{Direction} = \sqrt{(f_{Pr} - f_{Direction})^2 + (f_{Lo} - f_{Direction})^2 + (f_{La} - f_{Direction})^2}/f_{Direction} \quad (2)$$

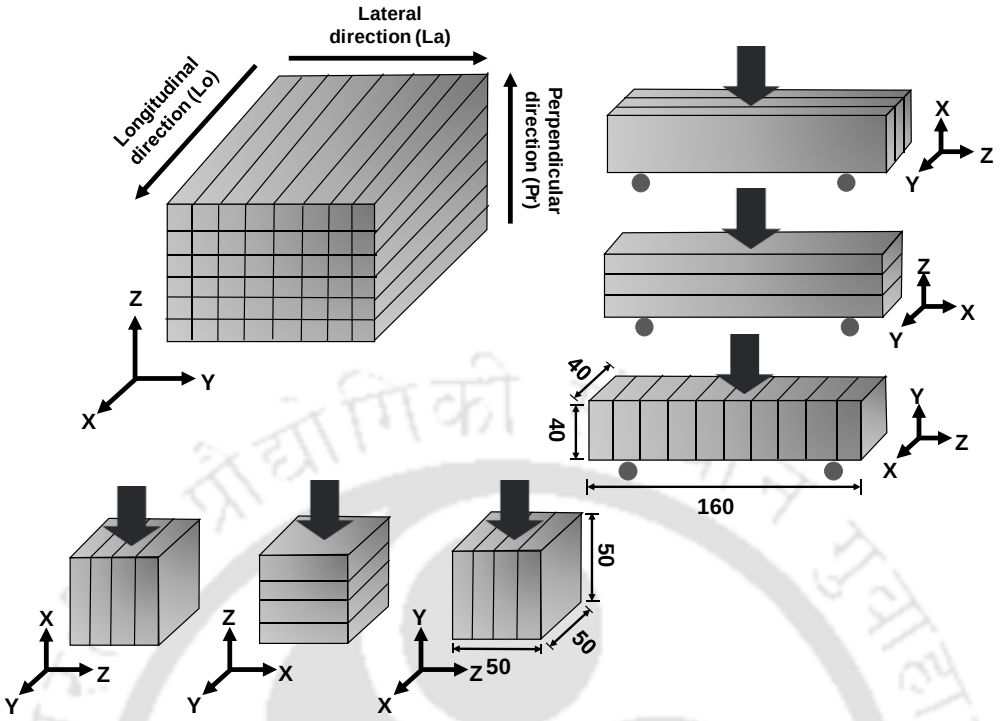

Figure 3.4 Schematic of loading direction for compressive and flexural testing.

3.2.4.2 Sorptivity test

After 28 days of curing, cubic specimens with 50 mm dimensions were prepared for capillary sorptivity testing in accordance with ASTM C1585-20. Prior to testing, a waterproof epoxy coating was applied to four sides of the specimens and allowed to dry for 24 hours. The specimens were then placed on 10 mm diameter steel bars in a water tray, ensuring that their lower surfaces were submerged to a depth of 3±1 mm. To prevent evaporation during testing, the upper surfaces of the specimens were sealed with aluminium foil. The water depth of 3 mm above the lower surfaces was carefully maintained throughout the test. Water uptake due to capillary action was measured by recording the weight gain of the surface-saturated specimens at different time intervals as mentioned in the standard. The sorptivity coefficient was determined using **equation 3** where the average value of three specimens for each mixture was reported.

$$I = S\sqrt{t} + b \tag{3}$$

where, 'I' denotes the cumulative water volume absorbed per unit surface area (mm^3/mm^2), 'S' represents the sorptivity coefficient ($mm/s^{0.5}$), 't' is the time in seconds, and 'b' accounts for the initial impact of surface water saturation. The capillary absorption process is divided into two

stages: the initial phase, occurring within the first 6 hours after testing begins, and the secondary phase, extending from 6 hours to 8 days. For this study, the initial (S_i) and secondary (S_s) sorptivity coefficients were calculated based on data from these respective phases.

3.2.4.3 Thermal test

The thermal conductivity of all specimens was measured at room temperature using a C-Therm TC kit based on the Transient Plane Source (TPS) method [115]. The TC kit operates within a measurement range of 0.03–60 W/mK, with precision exceeding 2%. The TPS method involves an electrically conductive bifilar spiral sensor, which simultaneously serves as both the heating element and the temperature sensor. This sensor is positioned between two cubic specimens of 50 mm size and a voltage change is induced across the sensor with the onset of current flow. Here, a test duration of 40 seconds and a power input of 0.9 W were chosen based on preliminary trials. The thermal conductivity values were determined from temperature-time response graph, using an iterative calculation method.

3.2.5 Early age accelerated carbonation test

In this study, accelerated carbonation curing regime was investigated. The printed beams were first moist-cured for 24 hours in the printing bed. Subsequently, the specimens were preconditioned in an environmental chamber at a controlled temperature of 25°C and 60% relative humidity for 72 hours [116]. After preconditioning, the beams were transferred to a carbonation chamber, where they were exposed to accelerated carbonation for 24 hours under a constant temperature of 25°C, 70% relative humidity, and 10% CO_2 concentration. Upon completion of the carbonation process, the samples were subjected to water curing up to 28 days prior to further testing.

3.2.6 Microstructural characterization

3.2.6.1 X-ray diffraction test (XRD)

Phase identification of the studied mixtures was conducted using X-ray diffraction (XRD) analysis on a Rigaku SmartLab 9 kW X-ray diffractometer equipped with CuKα radiation (λ = 1.5405 Å). The scan parameters included a 2θ range of 5° to 95° with a step size of 0.02° (2θ). Prior to analysis, mortar samples were ground to a fine powder using a mechanical grinder and passed through a 75 μm sieve to ensure uniformity. Diffractograms were analyzed using X'Pert HighScore Plus v.3 software for peak identification. To further quantify the degree of

crystallinity within the samples, the crystallinity index (CI) was determined using Segal method [117]. The CI was obtained by measuring the area under distinct crystalline peaks and comparing it to the total area under the diffraction pattern, which includes both crystalline and amorphous regions, using the formula (see **equation 4**):

$$CI = \frac{A_c}{A_c + A_a} \quad (4)$$

Where A_c represents the area under the crystalline peaks and A_a presents the area under the amorphous hump.

3.2.6.2 Thermo-gravimetric test (TGA)

Thermogravimetric analysis (TGA) was performed to assess the thermal stability and decomposition behavior of the mortar samples using a NETZSCH STA 449F3 instrument. The same powder samples prepared for XRD analysis were used for TGA, ensuring consistency across both tests. Powdered samples from the four mixtures were subjected to continuous heating from ambient temperature up to 950°C at a controlled heating rate of 10°C per minute. The analysis was conducted under an argon environment, with a gas flow rate of 60 mL per minute to ensure an inert atmosphere. The weight loss and corresponding thermal events were recorded throughout the heating process, providing insights into phase transformations, moisture loss, and decomposition of hydrated products. Along with TGA, the derivative thermo-gravimetry (DTG) curve was also analyzed.

3.2.6.3 Mercury-intrusion Porosimetry test (MIP)

Mercury Intrusion Porosimetry (MIP) was employed to evaluate the pore size distribution and pore microstructural analysis of the printed mixes. For this study, oven-dried samples (from the core) were cut into cuboid shapes with dimensions not exceeding 2 cm in length and 0.5 cm in width and height to ensure compatibility with the instrument. In the case of noncarbonated samples, specimens were extracted from the core, whereas for carbonated samples, the outer regions (confirmed by phenolphthalein test) were selected to capture the carbonation effects. The MIP analysis was conducted within a pressure range of 0.2 to 60,000 psi, allowing for the detection of pores with radius between 3.6 nm and 1100 µm, using Washburn **equation 5** [118] as shown below,

$$r = \frac{2\gamma \cos\theta}{P} \quad (5)$$

where r is the pore radius, γ is the surface tension of mercury, θ is the contact angle between mercury and the pore walls, and P is the applied pressure.

3.3 Results and discussions

3.3.1 Fresh state properties

3.3.1.1 Extrudability and open time

Extrudability is a critical criterion for evaluating the performance of 3D-printable mixes, and extrudability is inherently related to material flowability. Therefore, all mixes were tailored to have an initial flowability of 185 mm and it facilitated smooth extrusion with high shape retention (0.99) during 3D printing. However, the SRF gradually decreased with material rest time and at 'open time' of the material, the SRF is reduced below 90% resulting visible crack and discontinuity in the printed layer. Unlike setting time, open time dictates workability of the mixes for continuous printing. From **Figure 3.5** it is seen that in case of OR and OS mix, the open time was found to be 40 min, whereas a reduced open time of 30 min and 20 min was observed for PR and PS mixes respectively.

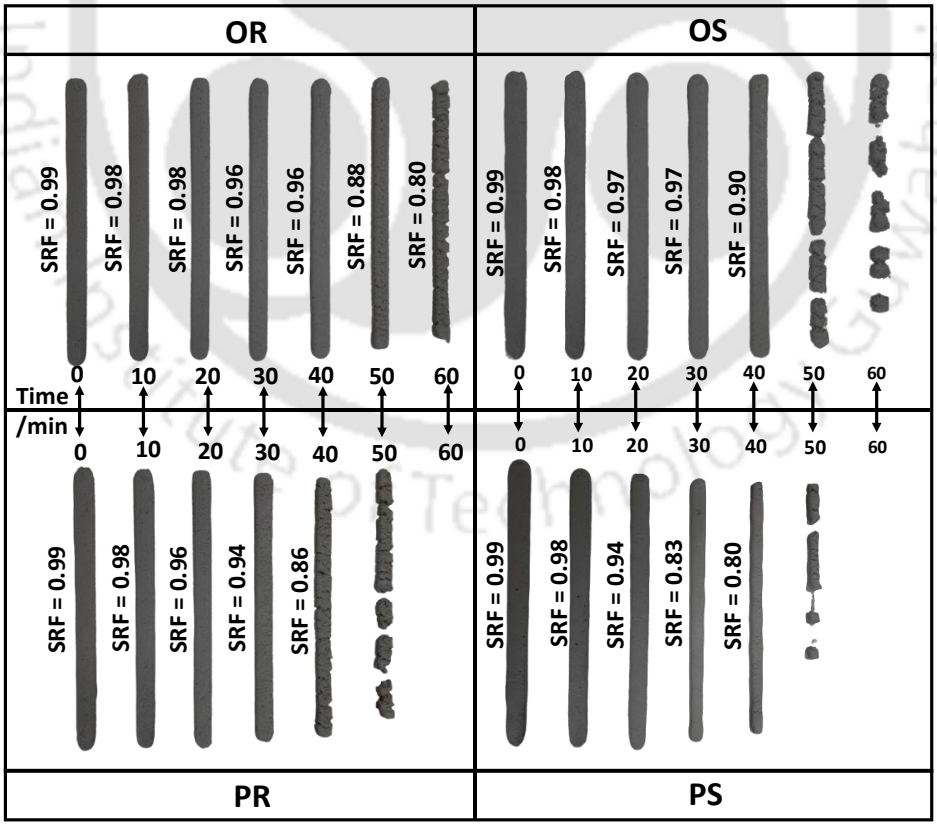

Figure 3.5 Effect of mix design on extrudability at different resting period.

It is important to note that at 50 min though the print width was reduced (SRF equals to 0.86), a continuous filament was observed for OR. This indicates material's ability to recovery the internal structure under shear forces allowed for sustained extrusion. However, at similar rest time (i.e. 50 min), discontinuous filament was observed for OS mix indicating faster loss of workability. The SS, being more angular and having a rougher texture (see **Figure 3.1(d)**) compared to natural RS, tends to increase the water demand of the mix. This results in a rapid depletion of free water during the resting period, thereby accelerating stiffening of the mix. In contrast, for PR mix, visible cracks began to appear at a 40-minute rest time. The substitution of PSC, which contains a higher proportion of alumina and silicate phases, leads to increased interaction with PCE based superplasticizers. This interaction enhances the surface adsorption of superplasticizer molecules onto the slag particles, thereby reducing the availability of free superplasticizer in the mix [119]. As a result, the dispersion of particles becomes less effective over time, which alters the rheological behavior of the mix. Similarly, in the case of the PS mix, although a continuous filament was observed at the 40-minute rest period, the print width was significantly reduced with SRF value of 0.80. This reduction is attributed to the synergistic effects of the higher water demand from the angular slag sand and accelerated structuration caused by the hydration products of PSC, which is further discussed in the following section.

3.3.1.2 Rheology and buildability

The results of initial stress growth test of all mixes shown in **Figure 3.6(a)** exhibit a rapid rise of stress to a peak, which indicates the material static yield stress ($\tau_{s,i}$). The stress levels further decrease and stabilize, reflecting the dynamic yield stress of the mix ($\tau_{d,i}$) required to maintain flow. The control mix (OR) exhibited the lowest yield stresses, with static and dynamic values of 1.99 kPa and 1.60 kPa, respectively. With respect to OR, OS mix showed moderate increase in the static (15%) and dynamic yield stress (18%) value, while the PR mix demonstrated 59% and 50% increment of static and dynamic yield stress respectively. In contrast, PS mix exhibited the highest yield stress values, with 150% increase in static yield stress and 118% increase in dynamic yield stress. It can be concluded that the use of slag as either binder or aggregate increases both static as well as dynamic yield stress. In extrusion-based 3D printing, dynamic yield stress of the material should be lower for smoother flow during pumping and extrusion, while the static yield stress of the material should be higher for holding the shape

and stability of layers after deposition. In this regard, thixotropy becomes crucial parameter, which can be measured through thixotropic index as shown in **equation 6**.

$$Thixotropy\ Index\ (TI) = \frac{(\tau_{s,i} - \tau_{d,i})}{\tau_{d,i}} \times 100\% \quad (6)$$

The thixotropic index was calculated for all the mortar mixes and plotted in **Figure 3.6(b).** It is clear that significant build up for PS mix is observed compared to OR. This trend demonstrates that the interaction of SS with PSC induces a greater thixotropic response than it's interaction with OPC. However, when PSC is mixed with SS, the alumina and silicate content in PSC interact with water and the calcium hydroxide (CH) produced during hydration over time. This chemical affinity between PSC and SS contributes to accelerated structuration and a marginal increase in thixotropy compared to OR mix.

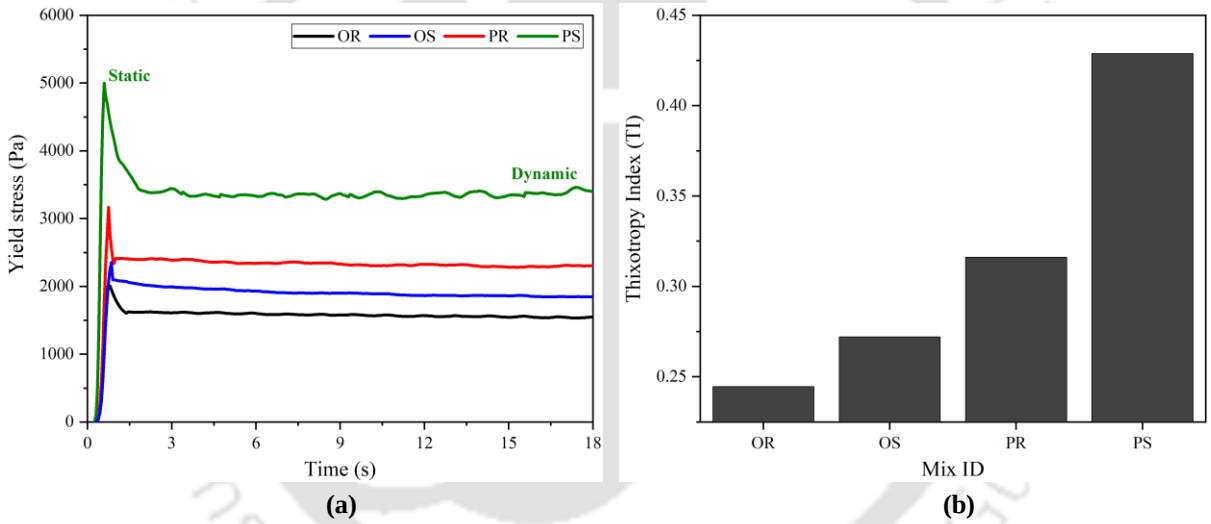

Figure 3.6 Effect of mix design on (a) yield stress, and (b) thixotropic index.

To further investigate the time-dependent rheology, the evolution of static yield shear stress was plotted in **Figure 3.7(a)**. This plot reveals a bilinear thixotropic development, where the slope of the initial curve corresponds to the re-flocculation rate (R_{thix}), and the slope of the secondary curve reflects the structuration rate (A_{thix}) of the material mixes (see **Figure 3.7(b)**). Here it was observed that for control mix (OR), R_{thix} and A_{thix} were found to be 0.93 Pa/s and 0.361 Pa/s respectively. In comparison, the OS mix showed increased values for both R_{thix} (1.01 Pa/s) and A_{thix} (0.486 Pa/s) indicating that the angular nature of SS enhances the inter-particle friction, thereby promoting greater resistance to breakdown under shear. Similarly, the mixes

with PSC binder (PR and PS) exhibited even higher R_{thix} and A_{thix} values. For the PR mix, the R_{thix} was 1.3 Pa/s, while A_{thix} was 0.631 Pa/s, underscoring the role of PSC fine particles and higher reactivity in strengthening particle interactions and contributing to a denser packed structure [120]. Notably, PS mix achieved the highest R_{thix} (1.92 Pa/s) and A_{thix} (1.12 Pa/s) values, confirming excellent thixotropic response for 3D printing applications. This enhancement can be attributed to the combined effects of PSC reactivity and the angular morphology of SS, which maximize internal cohesion and structural resistance, as evidenced by the steeper slopes in the bilinear plot.

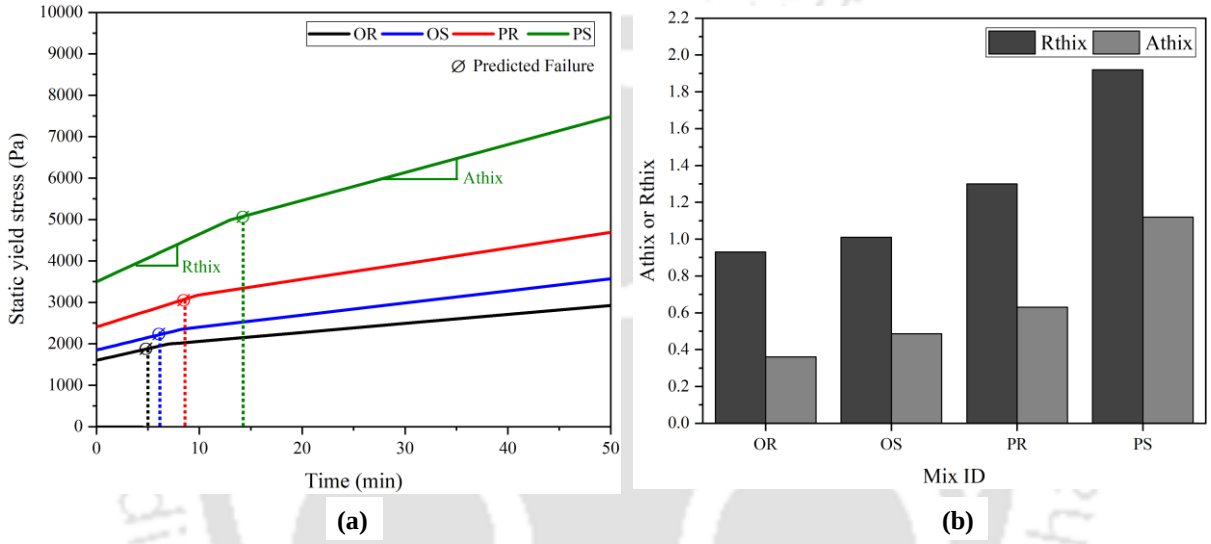

Figure 3.7 Effect of mix design on (a) static yield stress growth, (b) reflocculation and structuration coefficient.

The buildability test result (see **Figure 3.8**) revealed the control mix (OR) could build up to 30 layers, following which progressive slumping of each layer was observed. This phenomenon culminated in plastic collapse, leading to significant deformation in the top and bottom layer. The OS mix was successfully printed up to 39 layers, exhibiting similar failure mechanism. This can be attributed to the increased material strength (due to higher re-flocculation) as seen from **Figure 3.7(b)**. In contrast, the PR mix demonstrated sudden failure (at the top layer) after completion of 51 layers. In case of PS, no failure was observed up to 88 layers indicating higher buildability.

The experimental results were further analysed with theoretical buildability model proposed in [112]. The model predicts the number of buildable layers based on the building rate gradient and material-specific gradient criterion, as shown in **equation 7**.

$$N_L = \begin{cases} \dfrac{\tau_{d,i}}{\left(\frac{R_{thix}\cdot l_p}{\vartheta}\right)-\left(\frac{\rho\cdot g\cdot h_1}{2\cdot 10^{-3}\cdot F_{AR}}\right)} \; ; \; if \; \dfrac{\rho\cdot g\cdot h_1\cdot\vartheta}{2\cdot l_p\cdot F_{AR}\cdot 10^3} \geq \left(\dfrac{\tau_{s,i}\cdot R_{thix}}{\tau_{s,i}-\tau_{d,i}}\right) \\ \dfrac{\tau_{s,i}+\left(\frac{A_{thix}\times\left(\tau_{s,i}-\tau_{d,i}\right)}{R_{thix}}\right)}{\left(\frac{A_{thix}\times l_p}{\vartheta}\right)-\left(\frac{\rho\cdot g\cdot h_1}{2\cdot 10^{-3}\cdot F_{AR}}\right)} ; \; if \; \dfrac{\rho\cdot g\cdot h_1\cdot\vartheta}{2\cdot l_p\cdot F_{AR}\cdot 10^3} < \left(\dfrac{\tau_{s,i}\cdot R_{thix}}{\tau_{s,i}-\tau_{d,i}}\right) \end{cases} \quad (7)$$

Where, ρ is fresh state material density (in kg/m^3), g is acceleration due to gravity (m/s^2), h_1 is filament layer height (mm), N_L is number layers buildable (mm), l_p is circumference of one layer of cylindrical specimen (mm), ϑ is print speed (mm/s), F_{AR} is strength correction factor accounted for specific aspect ratio (0.33) of the printed filament.

Before failure				
No. of layer	30	39	51	88
After failure				No failure up to 88 layers
Mix ID	(a) OR	(b) OS	(c) PR	(d) PS

Figure 3.8 Effect of mix design on buildability study and its subsequent failure mode analysis.

The specific value of building rate gradient, material specific gradient, estimated and actual buildable height (prior to failure) is reported in **Table 3.5**. The model consistently predicted lesser buildable layers than actual, demonstrating its conservative lower bound nature. However, the maximum relative error was found within 10%, as observed in related studies [121].

Table 3.5 Different parameters of buildability estimation.

Mix ID	Fresh density (kg/m^3)	Building rate gradient	Material specific gradient	Estimated buildable height (mm)	Experimental buildable height (mm)	Relative error (%)
OR	2270	6.25	4.73	290	300	3.33
OS	2221	6.12	4.72	350	390	10.25
PR	2171	5.98	5.41	490	510	3.92
PS	2148	5.92	6.39	820	880	6.81

It was observed from the above table that the material loading rate for OR was significantly higher compared to other mixes. In case of OS, the building rate gradient decreased slightly due to the higher compact porosity of SS particles (see **Table 3.3**). However, the material-specific gradient remained nearly unchanged, resulting in a similar mode of plastic collapse as observed with the OR mix, with a minor increase in buildable height (60 mm). In contrast, for the PR mix, while the fresh stage density reduced (owing to lower specific gravity of PSC particles), its static yield stress growth was significantly higher which facilitated rapid strength development. This shift in behavior altered the failure mode from gradual plastic collapse to abrupt elastic buckling. Among all, the PS mix exhibited the highest material strength gradient, enabling it to resist deformation effectively under the weight of successive layers. This resistance was reflected in its lowest building rate gradient and as a result, the PS mix did not experience quick failure, and its estimated failure point shifted closer to the structuration curve in the bilinear plot, as shown in **Figure 3.7(a)**.

3.3.1.3 Green strength

To further investigate load-carrying capacity of the mixes, material green strength results were analyzed through the load-deformation graph and compression failure behavior at various time intervals. For specimens tested at early intervals (30 minutes and 60 minutes), the mixes

exhibited significant lateral deformation (bulging) with an ever-increasing load curve (see **Figure 3.9**). This behavior was particularly pronounced in the OPC based mixes (OR and OS), without a distinct peak in the load-deformation graph. In this context, the maximum load-carrying capacity was determined at a longitudinal deformation of 10%. Both OR and OS exhibited similar load-carrying capacities of approximately 0.01 kN at 30 minutes, however, at the 60-minute interval, OS demonstrated a slightly higher load-carrying capacity (0.03 kN) compared to OR (0.02 kN). Conversely, the PSC based mixes (PR and PS) exhibited different response with a clear peak that corresponds to the maximum load-carrying capacity. This behavior was further corroborated by failure mechanisms, where less bulging was observed for PR and PS mixes, compared to OR and OS (see **Figure 3.10**).

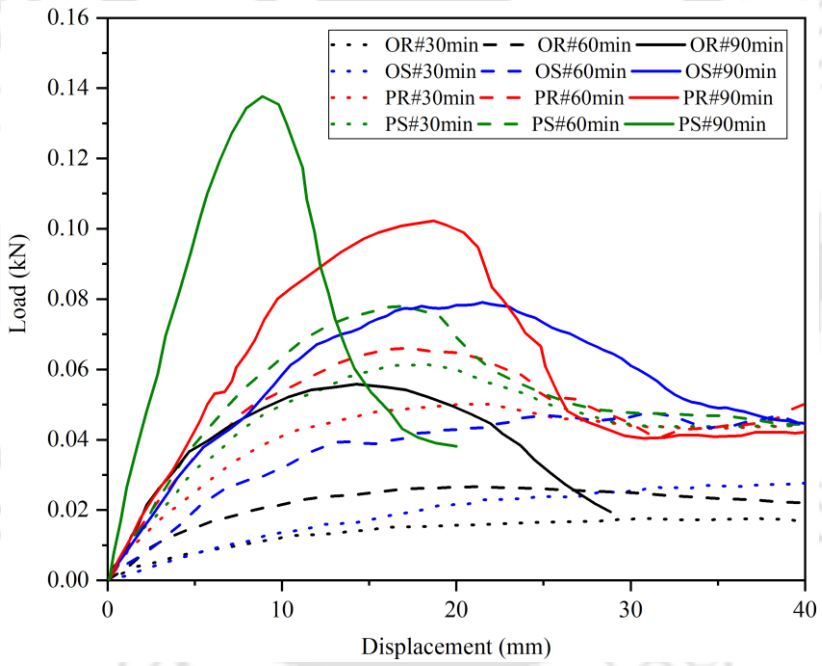

Figure 3.9 Effect of mix design on fresh stage load carrying capacity at different time interval.

With an increase in resting time up to 90 minutes, the PSC-based mixes exhibited higher peak loads, reaching 0.10 kN for PR and 0.14 kN for PS, with shear planes forming angles of 61° and 66°, respectively (see **Figure 3.10**). The increased shear angle and load capacity in PS and control mix reflect the superior structuration, where early age particle flocculation and physical interlocking strengthen the matrix. The structuration in slag-based mixes rapidly developed load-bearing capacity by creating a dense particle network, resulting in increased stability at early ages, often beneficial for 3D printing applications [122].

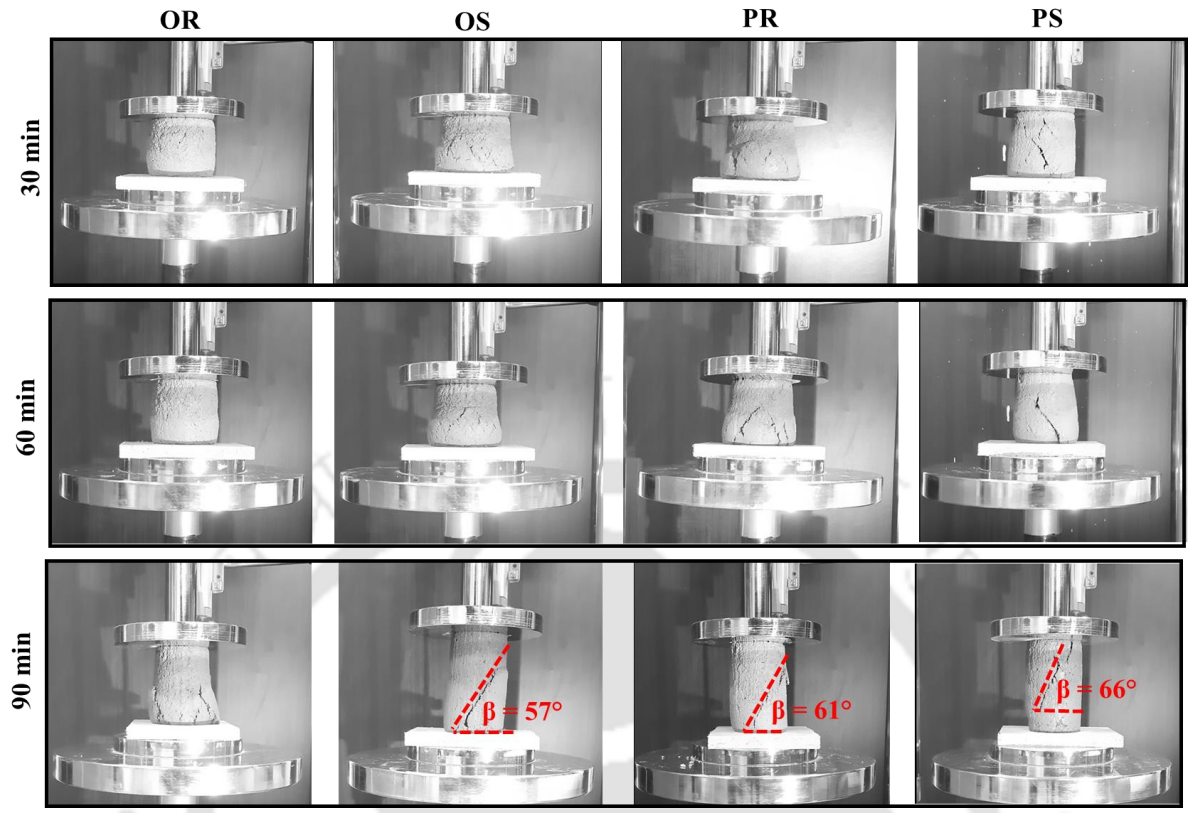

Figure 3.10 Compression failure behaviour of the mixes at different time interval.

3.3.2 Microstructural characterization

3.2.1 XRD analysis

The XRD plot (**Figure 3.11**) revealed significant insights into the mineralogical compositions of the studied mixes. Several crystalline compounds were identified in the XRD plot which include ettringite (ICDD # 00-034-0021), portlandite (ICDD # 00-033-0305), quartz (ICDD # 00-046-1045), and calcite (ICDD # 00-005-0586). In the OR mix, the XRD pattern is dominated by clear, intense crystalline peaks, particularly for quartz (at around 26.6°), portlandite and calcite. These strong peaks align with the well-ordered structure of hydration product of OPC [123] and inherently crystalline nature of RS (which contributes a crystallinity index of 59%). However, in OS mix, the XRD pattern shifted, with the quartz peak significantly diminished with a crystallinity index of 41%. This alteration arises from the amorphous nature of SS, produced by rapid quenching of molten slag. This is further verified in the XRD pattern of SS (see **Figure 3.3(b)**) and this amorphous structure also confirms SS increased reactivity potential, as discussed in previous section.

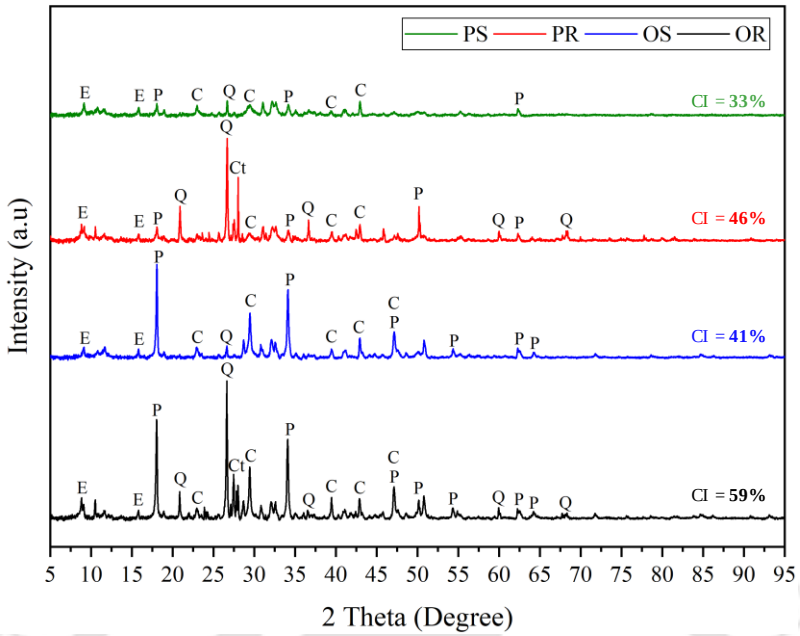

Figure 3.11 XRD plot of different mixes (Legend: Ettrengite(E), Portlandite (P), Quartz (Q), Calcite (C), Cristobalite (Ct)).

The XRD analysis indicated reduced intensities in both portlandite and calcite peaks, resulting in a crystallinity index of 46% for PR mix. This reduction in crystallinity (compared to OR) is directly influenced by the glassy content, which can be confirmed from the broader and less intense alite and belite peak of PSC [124] compared to the sharp, well-defined peaks of OPC (**Figure 3.3(a)**). The PS mix has lowest crystallinity index (33%) and substantial reduction in crystalline peaks was observed for quartz, portlandite, and calcite. The XRD pattern of PS reflects the glassy nature of both PSC and SS, and an increased potential due to secondary hydration reactions. The lack of portlandite peaks in PS is indicative of extensive pozzolanic reactions, which consume available calcium hydroxide and contribute to the formation of an amorphous C-S-H matrix.

3.2.2 TGA analysis

Thermo-gravimetric and derivative thermos-gravimetric analysis (TGA/DTG), as depicted in **Figure 3.12**, reveals distinct thermal decomposition behaviours of the mixes across three temperature ranges: 50-200°C, 400-500°C, and 650-750°C. Each range indicates specific phase transformations and decomposition events associated with hydration products and mineral phases, with corresponding mass loss percentages provided in **Table 3.6**. The first temperature range (50–200°C), primarily represents the dehydration of physically and chemically bound

water associated with different hydration products [125]. Despite differences in aggregate composition between OR and OS, both mixes exhibit similar mass loss percentages (~5.9%), suggesting comparable hydration product. However, in this specific temperature range, two distinct DTG peak highlights different form of water loss. The peak at 95°C is attributed to the loss of loosely bound and physically adsorbed water from ettringite, as confirmed by XRD data. The second peak around 140°C, correspond to the dehydration of chemically bound water from hydration products like C-S-H gel, which releases water at slightly higher temperatures due to its stronger binding nature. Additionally, the DTG signal of OS shows a broader and lower-intensity peak, suggesting a slower rate of decomposition and a more gradual mass loss, potentially due to the distributed bound water in its hydrated structure. For PSC-based mixes (PR and PS), the mass loss percentage is slightly lower (~5.3%) than OPC-based mixes (OR and OS), reflecting PSC's slower hydration characteristics. Moreover, the DTG signals of PR and PS were found similar which indicate that the type of aggregate has a reduced impact on the bound water release in PSC-based mixes.

Table 3.6 Mass loss details of mixes across three different temperature ranges.

Temperature range	Mass loss percentage			
	OR	OS	PR	PS
50 – 200°C	5.8907	5.9166	5.2089	5.5909
400 – 500°C	3.1914	2.7929	1.1975	1.1840
650 – 750°C	3.0855	2.7484	0.4164	0.4021

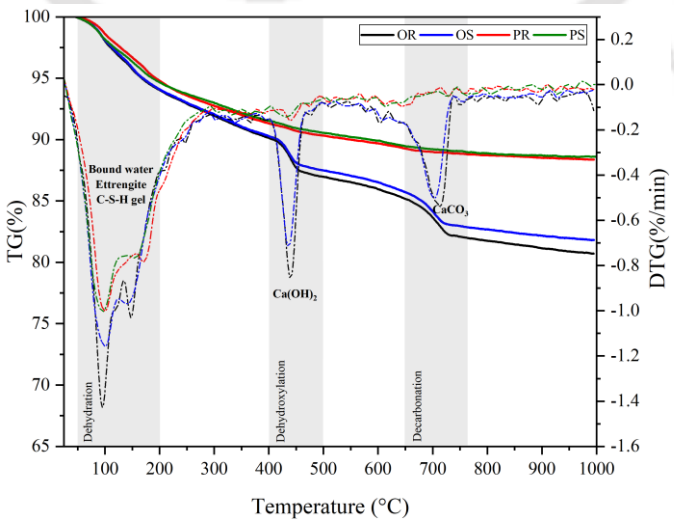

Figure 3.12 TGA/DTG plot of different mixes.

In the higher temperature ranges, thermal decomposition reflects the dehydroxylation of calcium hydroxide (400-500°C) and decarbonation of calcium carbonate phases (650-750°C) [125,126]. In OR mix, the mass loss percentage in both the temperature range were found to be significant (3.19% and 3.08% respectively) which indicate substantial amount of portlandite is present in the matrix even after the consumption of calcium in its decarbonation process. For OS mix, the mass loss percentage was slightly reduced to 2.79% and 2.74% respectively suggesting partial consumption of free portlandite by the amorphous SS, which contributes to secondary hydration. In contrast, the mass loss percentage of portlandite in PR and PS mix was found to be significantly reduced (~ 1.00%) due to latent hydraulic nature of slag which allows it to readily consume calcium hydroxide produced during hydration, thereby reducing the portlandite content available for dehydroxylation. Provided the decreased portlandite content, the mass loss due to decarbonation was further reduced (~0.40%) without any calcite peak in the DTG graph.

3.2.3 MIP analysis

From the MIP test results (see **Figure 3.13(a)**), the total porosity percentages were calculated for all printed specimens. The pore size distribution was analyzed across four distinct size ranges such as gel pores (<0.01 micron), small capillary pores (0.01 to 0.1 micron), large capillary pores (0.1 to 1 micron), and macropores (1 to 100 micron) as shown in **Figure 3.13(b)**. In the OR mix, the structure predominantly consists of larger pores, with 23% small capillary pores, 61% large capillary pores, and 16% macropores. In OS mix, though the total porosity was slightly higher, the pore distribution shifts towards smaller capillary pores (55%), with large capillary pores reduce to 33% and macropores to 12%. This indicates that the incorporation of slag sand refines the pore structure, with higher distribution of smaller capillary pores in the overall matrix. For PR mix, with higher total porosity percentage, the pore structure exhibits emergence of gel pores (25%) with major small capillary pores (64%), and a drastic reduction in large capillary pores to 8% and macropores to 3%. This shift toward smaller pore sizes reflects the reactivity of PSC, which promotes secondary hydration, thereby densifying the pore structure [120]. Compared to PR, the PS mix achieves a slightly lower total porosity and balanced distribution across gel pores (14%), small capillary pores (45%), large capillary pores (32%), and macropores (9%). This distribution indicates that PS benefits from both PSC and SS, achieving further refinement of the pore structure.

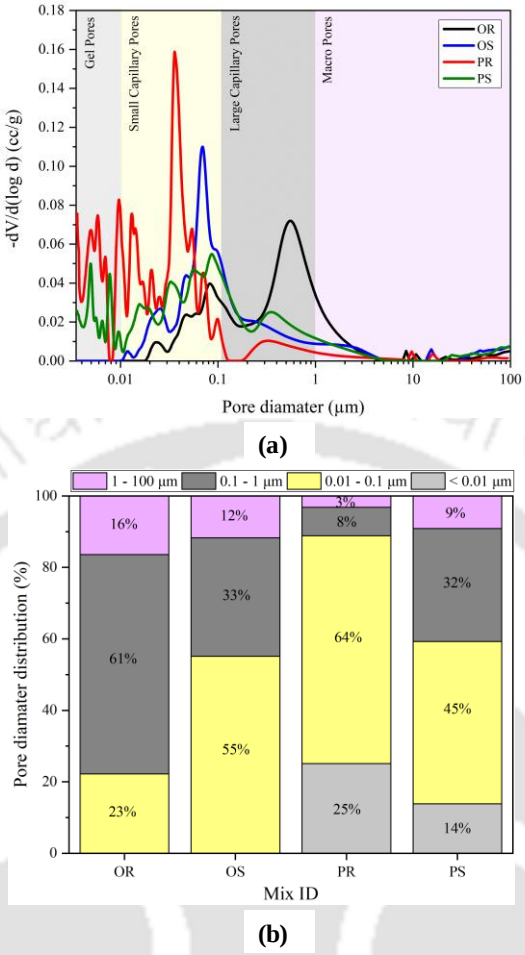

Figure 3.13 (a) Differential intrusion curve, (b) pore size distribution of different mixes.

3.3.3 Hardened state characterization

3.3.3.1 Compressive and flexural strength

The directional compressive strength of hardened specimens was determined at 28-day age and all printed specimens exhibited anisotropic behavior, with higher strength along the longitudinal (Lo) direction compared to the perpendicular (Pr) and lateral (La) directions. The Lo direction achieved highest compressive strength, attributed to the alignment of depositional and translational interfaces along the loading axis (which prevents relative slip between layers and enhances load-bearing capacity) [127]. Accordingly, the properties of different specimens were compared along the Lo direction, which offer a clear representation of the material's intrinsic compressive capacity, unaffected by interlayer shear weaknesses. From **Figure 3.14(a)** it was observed that OR exhibit highest compressive strength (60 MPa) corresponding

to its highest density (2254 kg/m^3) and lowest porosity (13.18%). This is closely followed by compressive strength of OS (58 MPa) where the density was reduced to 2201 kg/m^3 with slight increase in porosity (13.76%). The strength was further reduced to 51 MPa for PR mix with highest porosity of 16.57% and density of 2141 kg/m^3. This is followed by PS, where 48 MPa strength was observed with a slight reduction in density (2128 kg/m^3). This indicates the fact that as density decreases, the combination of higher porosity, reduced inter particle bonding, and the presence of amorphous phases contributes to lesser strength.

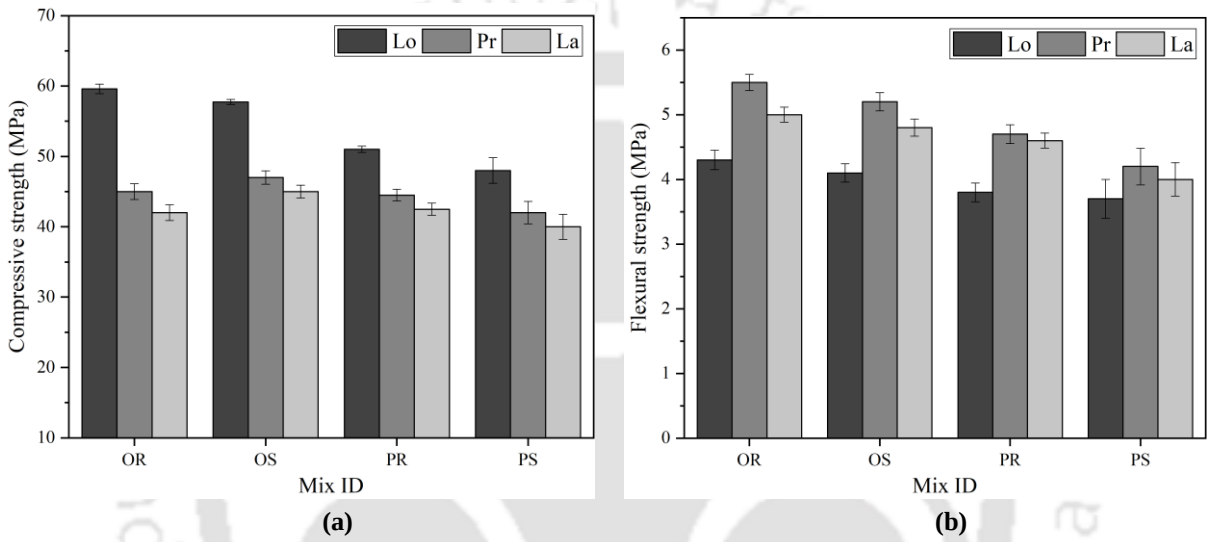

Figure 3.14 Effect of mix design on (a) compressive strength, and (b) flexural strength.

Additionally, it was observed that while the strength in the Lo direction decreases, the strengths in Pr and La directions does not vary much for different mixes. This consistency leads to an inverse trend with strength and significantly affect the anisotropy, where OR has maximum anisotropic index (0.38) followed by OS (0.27), PR (0.18) and PS (0.19). This indicates that, incorporation of slag increases the porosity, with more uniform distribution within the printed layers and along the interfaces. Similar strength and anisotropic pattern are observed in case of flexural loading (**Figure 3.14(b)**), however in this case, the highest strength was found in the Pr and La direction as it is unaffected by the tensile direction of any bonded interface [127].

3.3.3.2 Sorptivity result

Figure 3.15 presents time-dependent capillary absorption behaviour of the mixes. The water absorption rate was determined by analysing the slope of the linear regression between cumulative absorption (I) and square root of time. This absorption rate was subsequently

divided into initial sorptivity and secondary sorptivity, based on observed shifts in the slope. Results demonstrate that OR mix with a predominantly open pore network (comprising 61% large capillary and 16% macropores) exhibits the highest initial sorptivity (0.0135 mm/s$^{1/2}$), secondary sorptivity (0.0039 mm/s$^{1/2}$), and total absorption (5.568 mm). In the OS mix, though total porosity (13.76%) is slightly higher than that of OR (13.18%), initial sorptivity (0.0075 mm/s$^{1/2}$), secondary sorptivity (0.0017 mm/s$^{1/2}$), and total absorption (2.74 mm) were considerably lower. The reduction is predominantly observed in initial sorptivity level as it obstructs the early, rapid uptake of water through macro pore and large capillary pore which were significantly reduced to 33% and 12% respectively. It is important to note that though percentage of small capillary pores significantly increases (55%), it could not affect the sorption behaviour as smaller pores offer greater resistance to water ingress, dampening capillary action and slowing down the water absorption process.

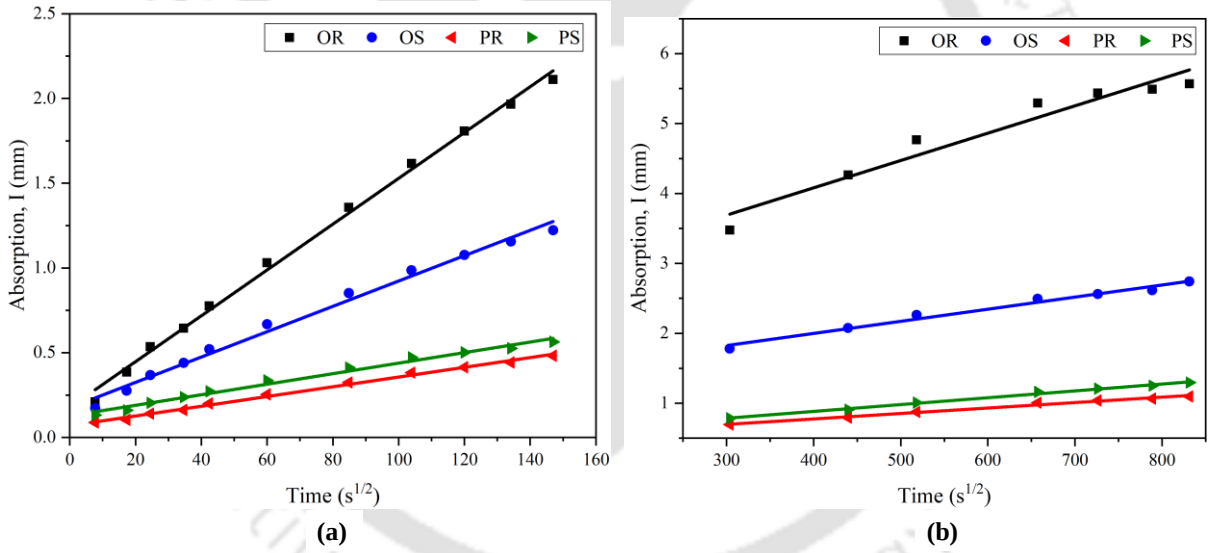

Figure 3.15 Effect of mix design on (a) initial, and (b) secondary sorption.

The PR mix with highest total porosity (16.57%), exhibits remarkably low initial sorptivity (0.0028 mm/s$^{1/2}$), secondary sorptivity (0.0007 mm/s$^{1/2}$), and total absorption (1.096 mm). This behavior can be attributed to the substantial reduction in macropores (3%) and large capillary pores (8%), which creates an effective barrier to water ingress during initial sorption, significantly limiting the opportunity for small capillary pores to contribute to secondary sorption. However, in the case of PS mix, a slight increase in total absorption (1.294 mm) was observed, indicating the simultaneous occurrence of densification (reduced total porosity) and

coarsening (increased fraction of macropores and large capillary pores). This effect is likely due to the hydration products of SS disrupting the close packing of gel pores (formed by PSC), resulting in the formation of coalesced, larger pores.

3.3.3.3 Thermal result

The thermal test result (**Figure 3.16**) shows that OR mix has the highest thermal conductivity of 1.52 W/mK which can be attributed to the crystalline hydration products of OPC and silica-rich composition of RS. In case of SS based mix (i.e. OS), thermal conductivity is drastically reduced to 0.91 W/mK which is attributed to the decrease in crystallinity (41%) of the mix. This is due to the fact that absence of definite crystal structure in SS causes phonon to scatter as there's no regular lattice to propagate. Aside this, additional microstructural defect (patched uneven surface along with micro-voids) on the surface of SS (as seen from **Figure 3.1(d)**) lead to greater phonon scattering and loss of energy, which further lower thermal conductivity of the mix [128,129]. However, in case of PR mix, thermal conductivity was reduced to an intermediate level (1.28 W/mK) corresponding to a CI of 46%. Here through the CI was comparable (to OS), the reduction in thermal conductance was minimal, as the crystallinity was reduced due to reduction in portlandite content in the mix which has minimal contribution to thermal conductivity [130]. In case of PS mix, the thermal conductivity was reduced to maximum 0.84 W/mK due to reduction of primary hydration product and strong crystalline peak of quartz. Nevertheless, porosity and density of the mix play a crucial role in influencing the thermal conductivity.

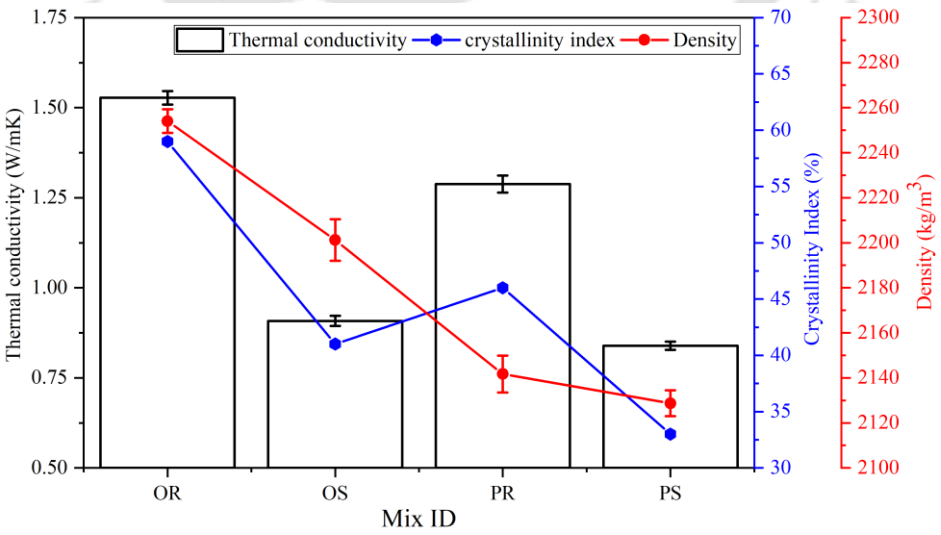

Figure 3.16 Effect of mix design on Thermal conductivity, crystallinity index and density.

3.3.4 Sustainability analysis

3.3.4.1 Carbon sequestration

The TGA and DTG of the early-age carbonated mixes revealed thermal decomposition patterns similar to control non-carbonated mixes, with detailed mass loss percentage calculation as shown in **Table 3.7**. Unlike earlier two distinct peaks in the low-temperature range (50-200°C), all carbonated mixes produce broad peak which typically indicates the presence of multiple thermal events occurring over a wide temperature range. The mass loss percentage in this temperature range was found to be reduced for all the mixes which indicates reduction in various hydration product due to carbonation. This is specifically reduced for PSC based mix (PR and PS) which may be attributed to decalcification of ettringite, C-S-H and other hydration product [131]. In contrast, the mass loss percentage in the intermediate temperature range (400 - 500°C) was found to be significantly reduced for OPC based mix (OR and OS), whereas there was no noticeable reduction for PSC based mix. This indicate that the carbonation of OPC based mix is largely due to consumption of calcium hydroxide, while decalcification of secondary hydration products is responsible for the PSC based mixes. These findings were further corroborated by the mass loss observed in the high-temperature (650-750°C) range, associated with the decomposition of calcium carbonate. Subsequently the carbon sequestration capacity was calculated based on the $CaCO_3$ content (calculated by multiplying mass loss to the molar mass of $CaCO_3$ and CO_2) for both carbonated and non-carbonated samples. The difference in both the value is represented as the net CO_2 uptake for different mix as shown in **Figure 3.17 (b) and** results show that the though OPC based mix has higher carbon potential, net CO_2 uptake of PSC based mix is significantly higher.

Table 3.7 Mass loss details of carbonated mixes across three different temperature ranges.

Temperature	Mass loss percentage			
	OR	OS	PR	PS
50 – 200°C	4.5231	4.0517	2.8550	3.1081
400 – 500°C	1.6660	1.6755	1.0030	1.0002
650 – 750°C	5.5601	4.8669	4.6775	4.1254

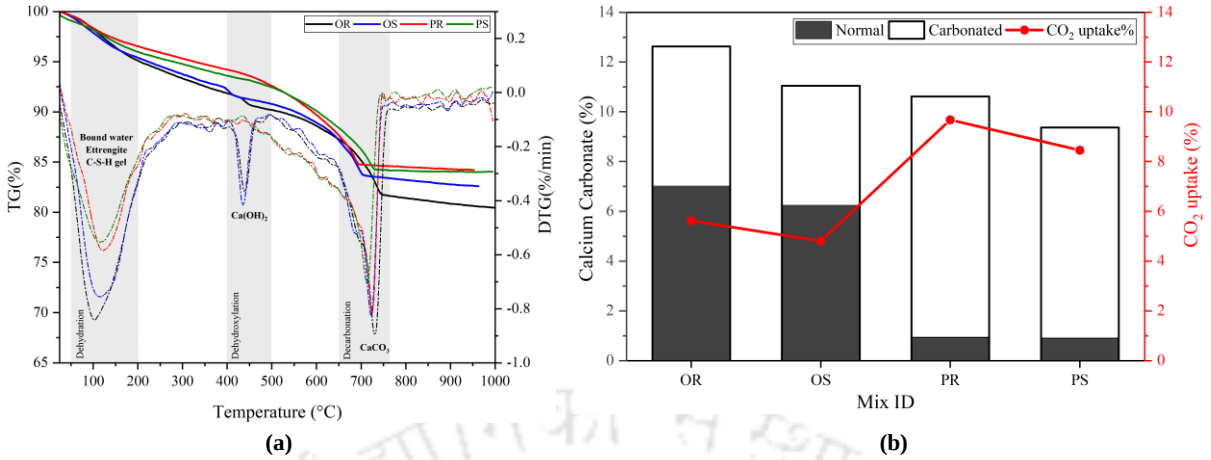

Figure 3.17 TGA/DTG plot of early age carbonated sample and (b) effect of mix design on CO_2 uptake.

3.3.4.2 Global warming potential and multi criteria efficiency evaluation

The Global Warming Potential (GWP) of the studied mix design was calculated with the equivalent CO_2 (eCO_2) values of commercially available raw material from different sources [132–136] as shown in **Table 3.8**. The eCO_2 of SS was calculated based on system boundaries of life cycle analysis study which comprise the secondary raw material extraction up to the finished product at the factory gate, as shown in **Figure 3.18**. As per one-year data of SS production at Vijayanagar (Karnataka, India) plant of JSW Cement limited, the carbon emission factor was calculated using the **equation 8** [137] .

$$eCO_2(SS) = \frac{1}{Q} \times [(E \times EF_e) + (F \times EF_f) + (D \times EF_t)] \quad (8)$$

Where,

Q is quantity of slag sand produced = 420 tonnes

E is electricity consumed for production process = 420000 kWh

EF_e is Emission factor for electricity = 0.817 kg CO_2/kWh (taken from CO_2 baseline database provided by ministry of power, Government of India)

FF is fuel consumed = 360000 litres diesel

EF_f is emission factor for diesel = 2.64 kg CO_2/litre (taken from India GHG programme database provided by ministry commerce and industry, Government of India),

D is inbound transportation distance = 3 km radius per trip (150 trip per day),

EF_t is emission factor for transportation = 0.593 kg CO_2/km (taken from India GHG programme database for medium duty vehicle).

This analysis yielded eCO_2 value of 0.0045 for SS, which is slightly lower (0.0051) than that of RS signifying the utilization of slag sand positively contributes to ecological sustainability by reducing dependency on natural resources and promoting recycling.

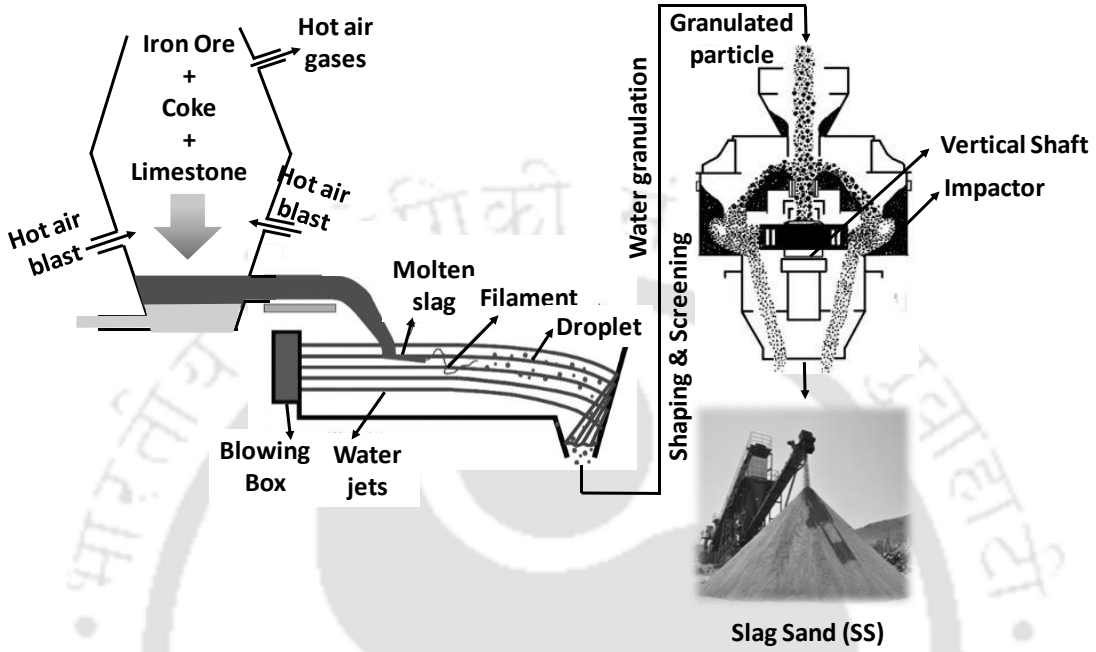

Figure 3.18 Schematic of slag sand production process.

Table 3.8 Equivalent CO_2 emission and cost of individual raw materials and their resulting mixes.

Raw material	eCO_2 (kg CO_2 /kg)	Cost (INR /kg)	OR		OS		PR		PS	
			eCO_2 (kg /m^3)	Cost (INR /m^3)	eCO_2 (kg /m^3)	Cost (INR /m^3)	eCO_2 (kg /m^3)	Cost (INR /m^3)	eCO_2 (kg /m^3)	Cost (INR /m^3)
OPC	0.959	9.10	961.50	9124.42	955.22	9064.14	-	-	-	-
PSC	0.325	7.20	-	-	-	-	321.04	7112.39	318.95	7066.10
RS	0.005	1.14	5.11	1143.06		-	5.04	1126.13	-	-
SS	0.004	5.46	-	-	4.48	5438.49	-	-	4.42	5358.46
Water	0.001	-	0.36	-	0.36	-	0.36	-	0.35	-
PCE	0.720	125.00	0.87	150.40	0.90	155.63	0.78	135.83	0.81	141.08
HPMC	2.640	638.40	2.65	640.11	2.63	635.88	2.60	630.63	2.59	626.53
Total			970.49	11057.99	963.59	15294.14	329.82	9004.98	327.12	13192.17

Based on the above data, GWP of mixes was calculated by multiplying the material quantities **(Table 3.4)** with the respective eCO_2 values of the individual raw material. The GWP analysis (see **Table 3.8**) revealed that PS has the lowest eCO_2 value at 327 kg/m³, demonstrating the effectiveness of utilizing PSC in combination with slag sand for lower carbon emission. Similar eCO_2 values were also observed for PR mix (330 kg/m³), however OR and OS mixes exhibited significantly higher (almost 3 times) values owing to highest carbon emission factor associated with OPC production. When compared to mixes incorporating other industrial by-products, such as fly ash (680 kg/m³) and silica fume (605 kg/m³), the eCO_2 values of the PS and PR mixes are approximately 50% lower and are comparable to those of geopolymer concrete mixes (295 kg/m³) where OPC was fully substituted [138].

To quantify the economic sustainability, cost analysis was also performed as shown in **Table 3.8**. Here the unit cost was considered as per the prevailing market price in Guwahati (Assam, India) where the actual production of concrete was done. It was observed that the PR mix was found to have lowest cost (9005 INR) followed by OR (11058 INR), PS (13192 INR) and OS (15294 INR). This shows that although slag sand has slightly lower eCO_2, its unit cost is higher owing to large transportation cost incurred. It is also to be noted that the eCO_2 of slag sand will be significantly increased if carbon emission for such long distance travel is accounted for while doing eCO_2 calculation. Hence it is suggested to use within 300-400 kilometres radius from its production site [139]. Based on the differentiated values for economic and environmental sustainability, a multi-criteria efficiency index (MEI) was calculated (See **Figure 3.19**), integrating environmental impact, economic cost, and multifunctional properties of the printable mixes as shown in **equation 9**.

$$MEI = \frac{Compressive\ strength \times buildabale\ height}{Cost \times eCO_2 \times Thermal\ conductivity} \quad (9)$$

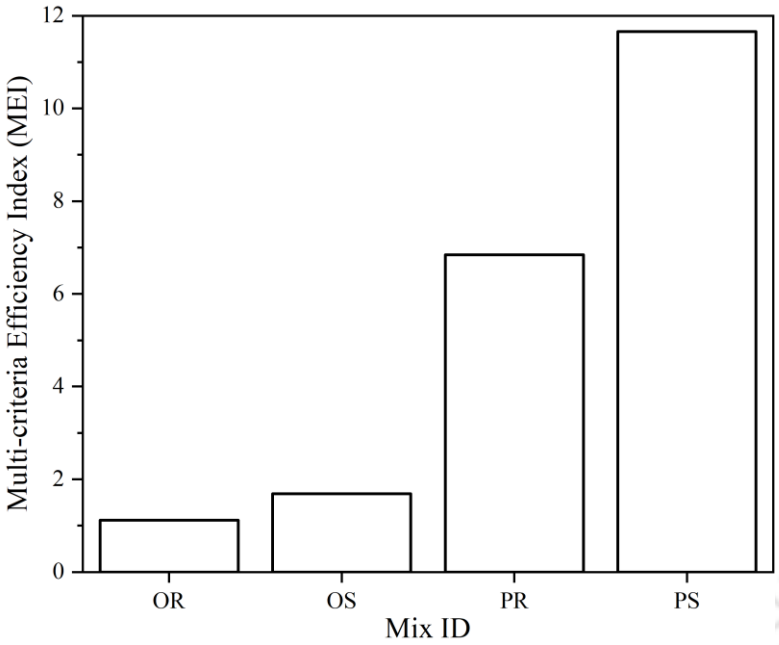

Figure 3.19 Effect of mix design on multi-criteria efficiency index.

This indicator, inspired by the framework proposed by Faleschini et al. [140], evaluates embodied carbon (kg CO_2/m^3) and cost (INR/m^3) in relation to material compressive strength (MPa). For 3D-printable mixes, buildable height (mm) was considered in the numerator and thermal conductivity (W/mK) in the denominator to emphasize the importance of energy efficiency in 3DCP projects. From **Figure 3.19**, it is observed that the PS mix has the highest MEI value (11.65), which highlights the feasibility of substituting PSC and SS with PC and RS to produce low carbon, high performance 3D-printable mixes. The PR mix, with an MEI value of 6.84, also demonstrates a favourable choice for thermo-mechanical performance, where trade-offs between environmental impact and economic cost are acceptable. In contrast, despite higher mechanical strength, MEI values for the OR and OS mixes were significantly lower (close to 1.5). This is attributed to the high embodied carbon and cost of raw materials, coupled with their poor buildability.

3.4 Summary

This chapter investigates sustainable utilization of slag-based materials in 3D concrete printing by substituting natural river sand with slag sand and Portland cement with slag cement. Early- and later-age fresh-state properties were assessed through rheology and green strength measurements. The inclusion of slag significantly improved rheological properties, with static yield stress, dynamic yield stress, and thixotropy increasing by up to 150%, 118%, and 18%,

respectively. Additionally, time-dependent rheological behaviors, such as static yield stress evolution, were identified as critical to ensuring structural buildability. Mechanically, slag-based mixes (OS, PR and PS) demonstrated more uniform strength across different built orientations, reducing anisotropy compared to control mixes, which achieved the highest longitudinal compressive strength (60 MPa). The OS and PS mixes exhibited lower conductivity (~0.87 W/mK), irrespective of the binder combination which is attributed to reduced crystallinity and enhanced microstructural defects of slag sand. Pore structure analysis revealed improved matrix densification in slag-based mixes, attributed to increased gel and small capillary pores. Early-age carbonation indicates higher CO_2 sequestration capacity in PSC mixes (PR: 9.67%, PS: 8.45%) compared to OPC mixes (OR: 5.61%, OS: 4.80%). While slag sand's transportation cost affects economic sustainability, its lower carbon footprint (eCO_2: 0.0045) resulted in mixes with PSC achieving the lowest GWP (327 kg/m^3) and the highest efficiency index (11.65), confirming their sustainable viability in 3D concrete printing.

CHAPTER 4

Flexural performance of 3D printed concrete structure with lattice infill configurations

This chapter investigates the flexural performance of 3D-printed lattice beams in vertical (layer deposition direction) and transverse (layer translation direction) loading directions. Extensive experimental investigation was performed to study the effects of infilled lattice configurations on peak load, maximum mid-point displacement, stiffness, and flexural deformation resistance capacity. A multiscale finite element (FE) model was developed and experimentally verified to analyze stress distribution and fracture modes in the 3D printed beams. The validated FE model was used to predict the flexural capacity of modified lattice beam configurations, which is further improved through parametric optimization.

A portion of this chapter has been published in:

Dey, D., Van, V. N., Xuan, H. N., Srinivas, D., Panda, B., & Tran, P. (2023). Flexural performance of 3D printed concrete structure with lattice infills. Developments in the Built Environment, 16, 100297. https://doi.org/10.1016/j.dibe.2023.100297.

4.1 Introduction

Large-scale 3D printed concrete structures with lattice infill will result in lightweight components with high mass-specific strength, and faster fabrication, compared to conventional casting methods. However, the mechanical performance of various infill patterns remains underexplored, as noted in Chapter 2. This study addresses this gap by investigating the flexural behavior of 3D-printed beams with lattice and triangular infill patterns under two distinct loading directions. The infill patterns were digitally designed with a constant volume fraction, and a multiscale finite element (FE) model was developed to capture the anisotropic behavior of fiber-reinforced cementitious mortar, overcoming the limitations of conventional beam theory. The FE model was experimentally validated using load-displacement curves and subsequently employed to analyze stress distribution and fracture modes in the beams. Following validation, the FE model was utilized to predict the load-bearing capacity of newly designed infill patterns and further parametric studies were performed to improve the structural performance. This comprehensive approach offers valuable insights into optimizing infill designs, paving the way for enhanced structural efficiency and performance in 3D-printed concrete components.

4.2 Beam design, fabrication, and experimental testing procedure

4.2.1 Beam design with infill patterns

This section describes the design and print paths of 3D-printed beams with four infill patterns namely lattice, triangular, lattice-triangular, and sinusoidal pathways. All the printed beams in this work have the same size: 290 mm x 200 mm x 890 mm (width x height x length). The lattice (**Figure 4.1(a)**), triangular (**Figure 4.1(b)**), and lattice-triangular (**Figure 4.1(c)**) beams are labeled as LBeam, TBeam, and LTBeam respectively.

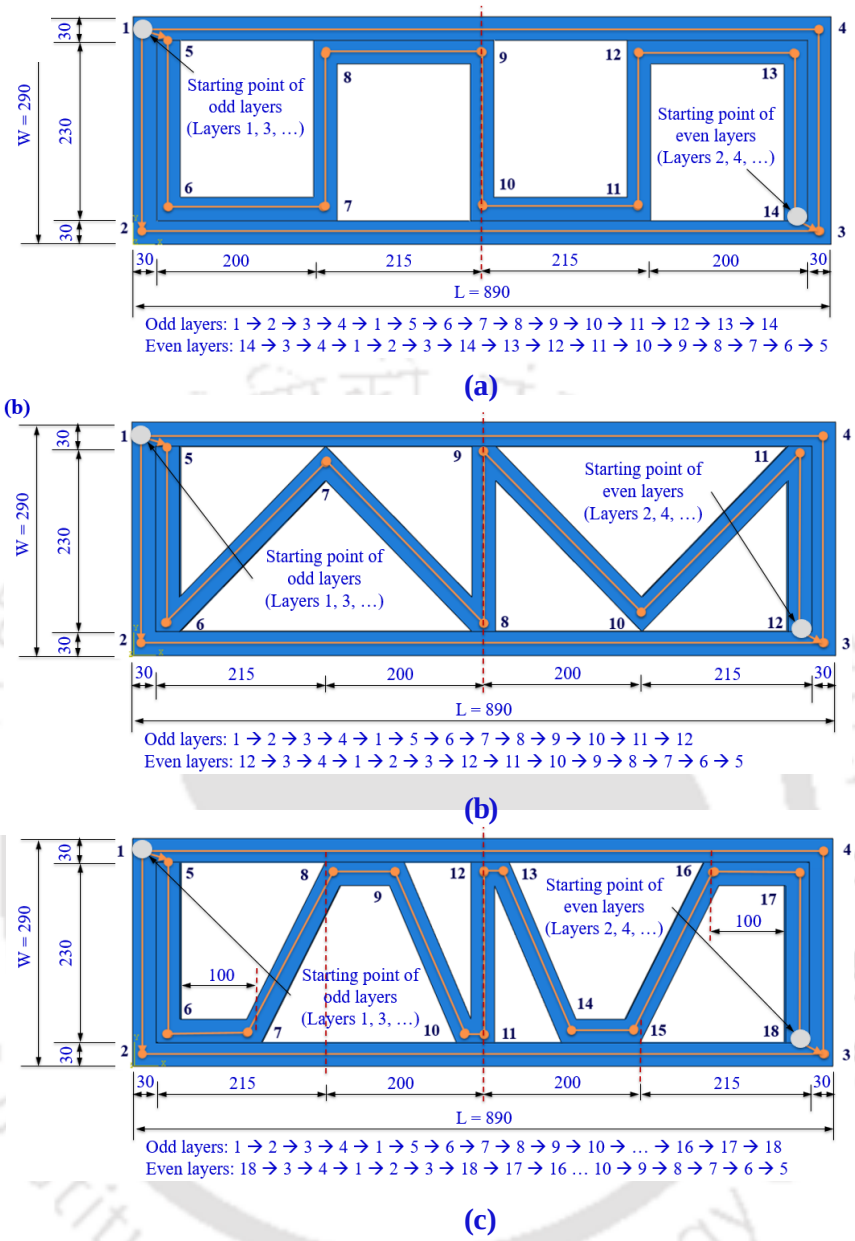

Figure 4.1 Different infill patterns: (a) LBeam, (b) TBeam, and (c) LTBeam (Unit: mm).

The infill patterns of the beam used in this study were digitally designed with nearly equal volume fraction, contour length (see **Table 4.1**), so that the comparative performance analysis was made based on final strength (instead of strength-to-weight ratio). The print path is prescribed by the preprogrammed Gcode file, which follows the heartline of the extruded filaments, as displayed in the brown lines in **Figure 4.1**. As a design rule, the toolpath trajectories (brown lines) in each beam must follow a continuous print path to ensure the structural integrity of the printed objects. Herein, the print path starts at point 1 (the grey circle

on the left-hand side of **Figure 4.1**), followed by points 2, 3, 4, and finally ends at point 1. From point 1, the tool path traversed to point 5 to print the infill patterns of the odd layers, i.e., layers 1, 3, 5, etc. Similarly, the even layers (layers 2, 4, 6, and so on) were printed in a reverse way.

Table 4.1 Configuration description of 3DPC beams

	LBeam	TBeam	LTBeam
Length of contour path	4190 mm	4169 mm	4346 mm
Volume fraction	46.33%	45.25%	47.04%

4.2.2 Materials and 3D printing of the beams

In this study, a printable fiber-reinforced mortar mix (modified OR) was prepared by blending natural river sand and cement-based binder in a ratio of 1:1.5. The binder system comprises 43-grade portland cement, conforming to IS 8112:2013, and densified silica fume (SF), meeting the requirements of ASTM C1240. The specific gravity of OPC and SF is 3.15 and 2.17, respectively. In case of aggregate, Zone-II river sand having a maximum particle size of 2.36 mm, specific gravity of 2.65, and fineness modulus of 2.75 is used. Methyl-cellulose-based viscosity modifying admixture and PCE-based SP were further added to the mixture. Chopped PVA fibers, 12 mm long and 0.04–0.06 mm in diameter, were used as fiber reinforcement. The mix design and characteristics of the PVA fibers (obtained from supplier) are listed in **Table 4.2** and **Table 4.3**, respectively.

Table 4.2 Cementitious mix design and raw materials

Sand /binder	Water /binder	OPC /binder	SF /binder	SP /binder	VMA /binder	PVA Fibers (% Vol.)
1.5	0.35	0.90	0.10	0.58	0.12	0.25

In order to get homogeneous mix, a laboratory-scale planetary mixture (from Hobart, Germany) was utilized for batch mixing. At first, all of the dry components, including OPC, SF, sand, and VMA were mixed at 107 rpm for one minute. Then, half of the total water was added to the dry mix and mixed at 198 rpm for 2 min, followed by a half minute of scraping. The SP was dispersed in the rest of the water and mixed with mortar at 361 rpm for 1 minute to get a consistent mix. The PVA fibers were introduced (in 4 batches) in the final stage of

mixing at a time interval of 1 minute and continuously mixed at a slow speed (198 rpm) to avoid the fiber clotting.

Table 4.3 Properties of polyvinyl alcohol (PVA) fibers

Characteristics	Values
Diameter, d_f (mm)	0.04
Length, L_f (mm)	12
Aspect ratio (L_f/d_f)	300
Volume fraction	0.0025
Young's modulus (GPa)	42.8
Tensile strength (MPa)	1060
Poisson's ratio	0.42- 0.48
Density (g/cm^3)	1.300

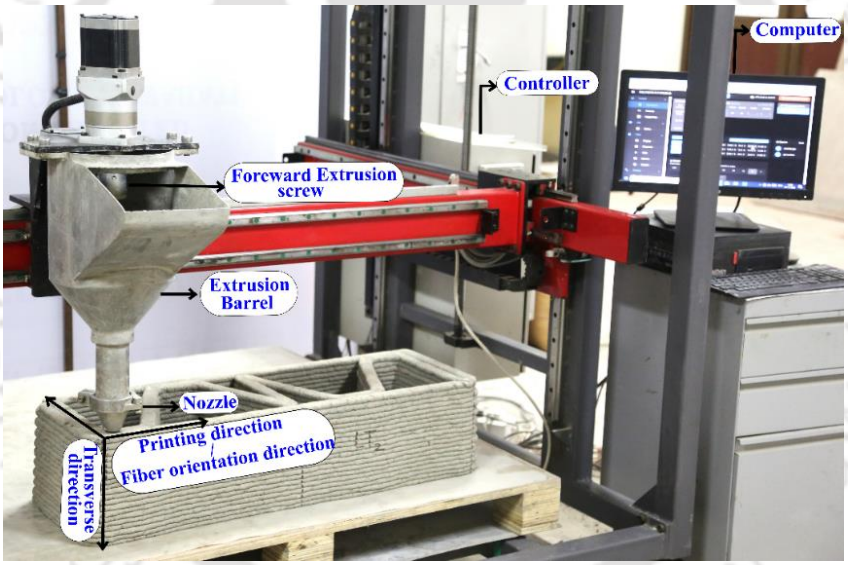

Figure 4.2 3D concrete printing of the LT lattice beam.

The lattice infilled beams were 3D printed using an extrusion-based concrete printer. A circular nozzle, 20 mm in diameter, was used to print filaments of layer height 10 mm and width 30 mm. The geometry of the beams was first modelled using Solidworks 3D CAD and then the 3D model was sliced into layers. The sliced model was used to create G-code data that specifies the line of printing path. The stand-off distance of 10 mm and a layer width of 30 mm are selected to improve the concrete filament stability and inter-layer adhesion between consecutive layers and adjacent filaments. The 3D-printed beams were printed at a constant speed of 2,400 mm/min and moist-cured for 28 days prior to three-point bending tests.

4.2.3 Three-point bending tests

The three-point bending tests for the 3D-printed lattice beams were performed using a double-ended, double-acting, heavy-duty actuator (MTS 244.31) that operates on a closed-loop servo-hydraulic system. The load was moved using hydraulic pressure, and a closed-loop servo valve manifold system (with an inbuilt linear variable displacement transducer (LVDT) sensor within) which gives accurate positioning control. The actuator includes two hydraulic chambers on either end that allow the load to be moved in both directions. When hydraulic pressure was given to one of the chambers, the hydraulic fluid drives the piston attached to a lead screw. The lead screw translates the load in a linear motion. At the same time, the opposite chamber's hydraulic fluid was released, allowing the load to travel freely in the opposite direction.

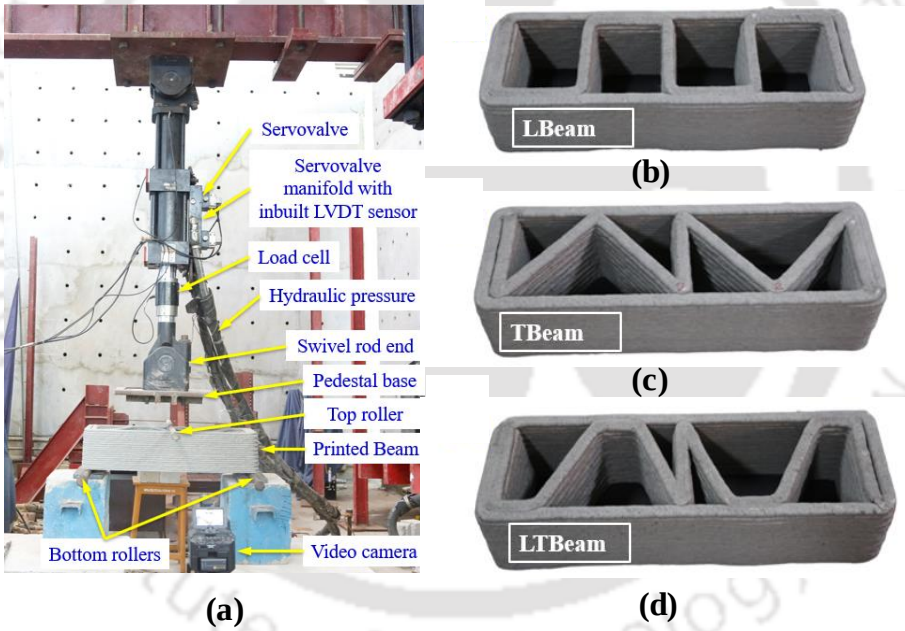

Figure 4.3 (a) Experimental setup for three-point bending tests; 3D printed concrete beams with different infill patterns: (b) LBeam, (c) TBeam, (d) LTBeam.

A feedback device, such as an LVDT or encoder, was used in the servo-hydraulic system to provide positional feedback to the servo controller. The servo controller then adjusts the hydraulic pressure and flow to maintain precise control over the actuator's motion. The different parts of the actuators are shown in **Figure 4.3(a).** In the current study, 3-point bending tests were first conducted on the LBeam and TBeam, examining their structural response in

both vertical and transverse loading directions. The experimental investigation of LTBeam and SBeam performance was conducted under vertical loading, while numerical simulation was used to predict the performance in transverse loading direction. During bending, the load was applied at the center of the beam at a constant loading rate of 1 mm/min, and the crack propagation was recorded using high-definition digital camera from both sides of the beam. In the transverse loading case, the beams were loaded in areas supported by vertical wall.

4.2.4 Material characteristics for FE modeling

The FE model uses material characteristics derived from the uniaxial compressive stress-strain response of plain and fiber-reinforced cementitious mortar (modified OR). To evaluate the hardened properties of 3D-printed mortar, two types of block sizes were prepared (see **Table 4.4**). The dimension of the first block (Block A) and the second block (Block B) are 500 mm (l) × 180 mm (w) × 70 mm (h) and 240 mm (l) × 240 mm (w) × 70 mm (h), respectively. From Block A, twelve cubic specimens of dimension 50 mm (l) × 50 mm (w) × 50 mm (h) were extracted for compressive and splitting tensile test. Similarly, three prism specimens of dimensions 175 mm (l) × 50 mm (w) × 50 mm (h) were extracted from Block B for flexural tests, as shown in **Figure 4.4(a, b)**. Uniaxial compression test, and flexural testing splitting tensile test were performed in a servo-controlled hydraulic universal testing machine (UTM BiSS ®) equipped with MTL-32 2020 software in accordance with ASTM C109, NEN-EN 12390-6 [33], ASTM C348 [34] respectively. The loading was applied in position-controlled mode (accuracy of ≤ ±1%) with a constant displacement rate of 1 mm/min. The flexural crack development within the shear span of reinforced beam is often caused by inclined cracks [35]. In general, flexural stress is the governing strength for a long beam, whilst a short beam mainly creates shear stress. The typical stress distribution of shear and flexural stress in a reinforced concrete beam is shown in **Figure 4.4(c)**. For a rectangular beam, the following formula (see **equation 10**) defines the shear stress [35]:

$$f_v = \frac{VQ}{Ib}, \tag{10}$$

where V is the maximum load applied to the beam, Q is the moment of area (= $0.5bh^2$), I is the moment of inertia about the neutral axis (= $\frac{bh^3}{12}$), b is the width of the beam.

Table 4.4 Types and tests applied for block specimens

Name	Material	Dimension L x W x H	Number of specimens	Shape of specimen	Tests applied	Expected results
Cast Block	Plain cementitious mortar	50 mm × 50 mm × 50 mm	03*	cube	Compressive Test (Single direction of loading)	Stress-strain curves; Uniaxial compressive strength
Printed Block A	Fiber-reinforced cementitious mortar	500 mm × 180 mm × 70 mm	03	cube	Compressive test (Vertical loading)	Stress-strain curves; Uniaxial compressive strength
			03		Compressive test (Transverse loading)	Stress-strain curves; Uniaxial compressive strength
Printed Block A		500 mm × 180 mm × 70 mm	03	cube	Split tensile test (Vertical loading)	Maximum tensile stress; displacement at failure
			03		Split tensile test (Transverse loading)	Maximum tensile stress; displacement at failure
Printed Block B		240 mm × 240 mm × 70 mm	03	prism	Three-point bending test (Vertical loading)	Mid-point load vs displacement curve; flexural strength
			03		Three-point bending test (Transverse loading)	Mid-point load vs displacement curve; flexural strength

** In case of casting, cube specimens were mold cast not extracted from any larger block*

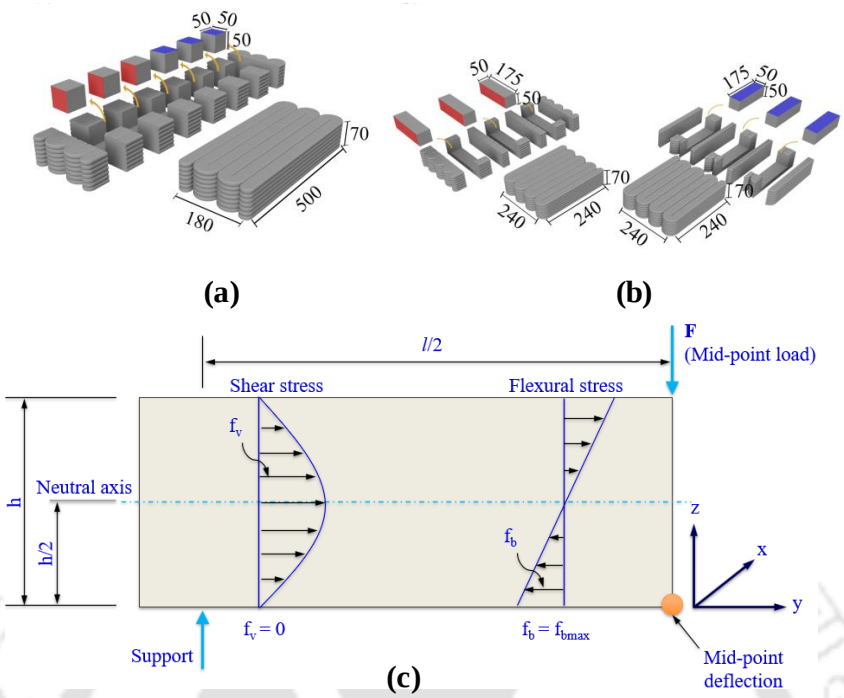

Figure 4.4 Schematic of 3D printed blocks and extraction of prism specimens for hardened properties testing: (a) cubes for uniaxial compressive and tensile tests, (b) beams for three-point bending tests (unit: mm, red-colored face shows loading along the printing direction and the blue plane shows loading along the transverse direction), and (c) shear stress and flexural stress distribution within the shear span.

4.3 Modeling approach

4.3.1 From micro to macro scale models

Multi-scale models were employed to simulate the mechanical behavior of 3D-printed lattice beams in this study. In the micromechanical model, a representative volume element (RVE) was used to analyze the interaction between PVA fibers and cementitious mortar. To portray the anisotropy of the composite material, a set of homogeneous properties was obtained from the post-processing of micromechanical model analysis [27, 36]. To be specific, two modifiable materials of interest that contain fibers and matrix properties were provided after creating the RVE. Herein, the mechanical properties of PVA fibers and plain cementitious mortar were used to generate the composite characteristics. The model was coded as a plugin in Abaqus software. **Figure 4.5** represents the homogenization method, in which the homogeneous solid element was obtained from a heterogeneous composite with two phases (fibers and plain cementitious mortar). In the macro model, Hill's anisotropic yield criterion was employed to capture the hardening-softening response in compression.

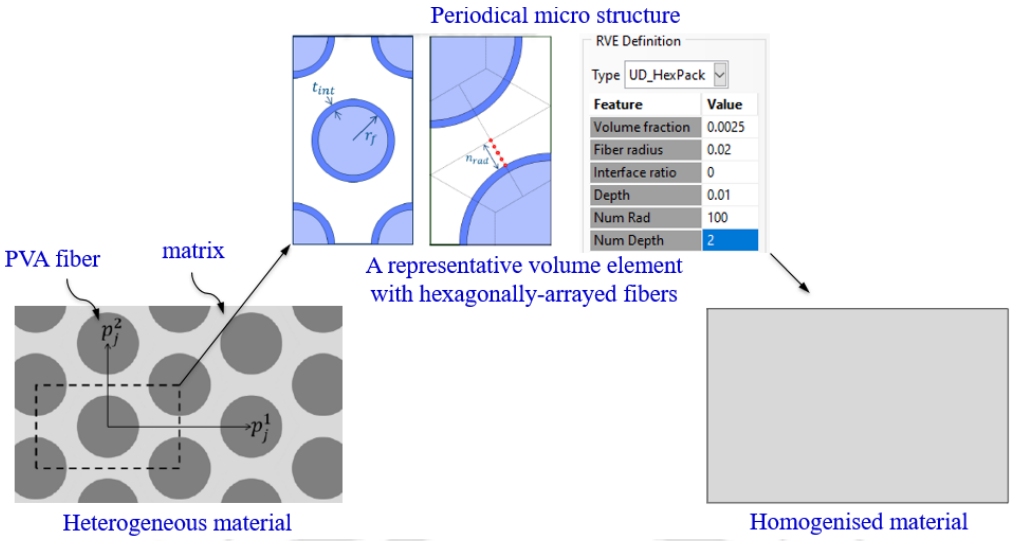

Figure 4.5 From heterogeneous to homogeneous materials [27, 37].

In the macro-scale model, homogenized parameters that take the contribution of fibers and cementitious mortar into the post-processing analysis were used. Expectedly, the homogenized material exhibits anisotropy due to the presence of fibers. Therefore, orthotropic elastic behavior was adopted to model the anisotropic characteristics of the material. Equation (11) displays the relation between elastic strain ε_{ij} and stress σ_{ij}. Nine parameters, i.e., poisson's ratios (ν_{ij}), three shear moduli ($G_{1\text{-}3}$), and young's moduli ($E_{1\text{-}3}$), are provided.

$$\begin{Bmatrix} \varepsilon_{11} \\ \varepsilon_{22} \\ \varepsilon_{33} \\ \varepsilon_{12} \\ \varepsilon_{13} \\ \varepsilon_{23} \end{Bmatrix} = \begin{bmatrix} 1/E_1 & -\nu_{21}/E_2 & -\nu_{31}/E_3 & & & \\ -\nu_{12}/E_1 & 1/E_2 & -\nu_{32}/E_3 & & & \\ -\nu_{13}/E_1 & -\nu_{23}/E_2 & 1/E_3 & & & \\ & & & 1/G_{12} & & \\ & & & & 1/G_{13} & \\ & & & & & 1/G_{23} \end{bmatrix} \begin{Bmatrix} \sigma_{11} \\ \sigma_{22} \\ \sigma_{33} \\ \sigma_{12} \\ \sigma_{13} \\ \sigma_{23} \end{Bmatrix}, \quad (11)$$

Since the fiber-reinforced cementitious mortar was considered a perfectly plastic solid after the occurrence of yield [24], Hill's anisotropic yield criterion was employed for the computational model. In this study, Hill's yield criterion was employed to evaluate and anticipate the deformation and material anisotropy of 3DPC beams under three-point bending tests. Other input parameters (anisotropic yield stress ratios) that need to be provided for the material model were obtained from the mechanical testing on hardened samples. The Hill's potential function was determined based on six yield stress ratios (R_{11}, R_{22}, R_{33}, R_{12}, R_{23}, R_{13}). As an additional option in the plastic regime, these six ratio components are defined below (**equation 12**):

$$\begin{cases} R_{11} = \frac{\sigma_{11}}{\sigma^0} \\ R_{22} = \frac{\sigma_{22}}{\sigma^0} \\ R_{33} = \frac{\sigma_{33}}{\sigma^0} \\ R_{12} = \frac{\sigma_{12}}{\tau^0} \\ R_{13} = \frac{\sigma_{13}}{\tau^0} \\ R_{23} = \frac{\sigma_{23}}{\tau^0} \end{cases}, \quad (12)$$

where σ_{12}, σ_{13}, σ_{23} are shear stress, and σ_{11}, σ_{22}, σ_{33} are direct stress in the printing direction. $\tau^0 = \sigma^0/\sqrt{3}$ is reference shear stress, and σ^0 is the reference yield stress. In this work, σ^0 was assumed as maximum stress of the fiber-reinforced cementitious mortar in the printing direction.

4.3.2 Numerical simulation

4.3.2.1 Finite element analysis

A commercial FE analysis software ABAQUS FEA was used to simulate both vertical and transverse loading conditions. The experimental setup and numerical model of the TBeam in both loading directions are illustrated in **Figure 4.6(a)** and **Figure 4.6(b)** respectively. In all instances, linear eight-node continuum solid elements (C3D8R) were used for 3D-printed filament (see **Figure 4.6(c**)), in which the element size is 10 mm x 10 mm x 10 mm. This mesh size was obtained through the implementation of mesh sensitivity. The option of tied constraints was used in this study for layer-to-layer connection. This contact pair includes contact-based interactions (mutual contact characteristics).

For the boundary condition and loading, maximum mid-point displacement of up to 10 mm was assigned to the upper roller to make the bending load (see **Figure 4.6 (a, b**)). Meanwhile, the other two rollers at the bottom (two sides of the beam) were defined as fixed boundary conditions. General contact was used to indicate the interaction between 3D-printed beams and rollers. A small friction coefficient of 0.15 was assigned between the 3D-printed lattice beams and rollers to prevent unrealistically large lateral movement of the beam, in the case of an ideal frictionless contact [27].

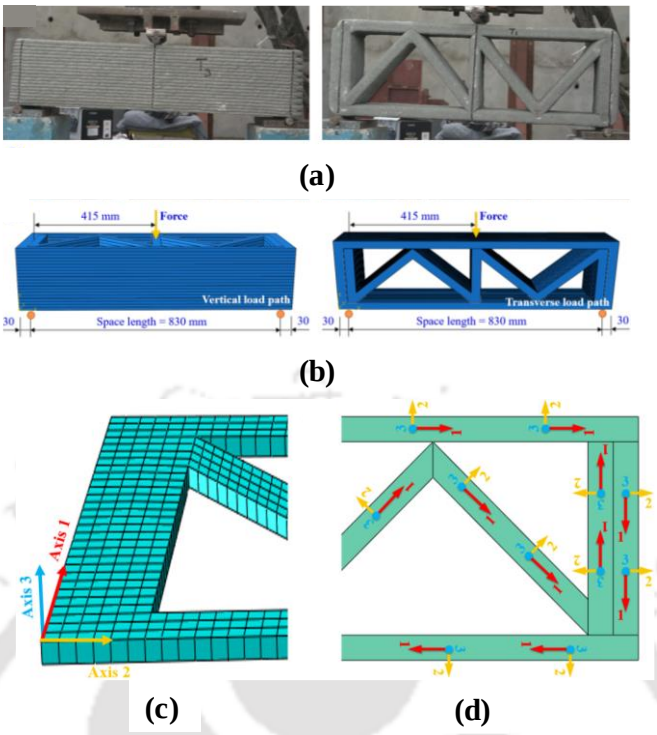

Figure 4.6 (a) Experiment setup and (b) numerical model of TBeam under three-point bending test with vertical load path (left) and transverse load path (right); (c) mesh size of a typical 3DPC layer (10 mm x 10 mm x 10 mm), (d) material orientation in each layer.

4.3.2.2 Constitutive material models

As the accuracy of multi-scale simulation relies on experimental attempts, various mechanical testing programs were employed (section 4.2.4) to determine different material parameters for the constitutive models. The plain cementitious mortar mix properties (see **Table 4.5**) were used as input parameters for the micromechanical model in form of matrix. For including the fiber role, PVA properties shown in **Table 4.3** is used in the modelling. The outcomes of the micromechanical model analysis consist of homogenized attributes which are handy for adding to macro mechanical models later on. When the modulus of elasticity of the homogenized composite material is selected as a type of engineering constant in the post-processing step, nine material parameters indicated in Eq. (5) are provided. As expected, the micromechanical model shows the anisotropy in the material's elastic phase, in which transverse directions give out smaller values in comparison with those in the printing directions (see first four parameters in **Table 4.5**). The density and young's modulus obtained from the micromechanical models were validated with the data attained from the hardened testing series. In the plastic regime of the concrete and fiber composite, different mechanical testing procedures including uniaxial

compression, splitting tension, and three-point bending tests (see Section 2.4) were carried out to obtain compressive, tensile, and shear stress versus strain data, respectively. Six parameters of Hill's yield criterion mentioned in Eq. (5) were also obtained, as listed in **Table 4.5**.

Table 4.5 Constitutive material parameters for numerical simulation

Plain cementitious mortar					
Max. compressive stress (MPa)	Poisson's Ratio, ν		Modulus of Elasticity, E (MPa)		Density, ρ (kg/m3)
40.00 ± 3.00	0.18		34500.00 ± 50.00		2029.00 ± 5.00
Fiber-reinforced cementitious mortar (Modified OR)					
			Printing direction		Transverse directions
			From micromechanical models		
Density, ρ (kg/m$^{3)}$			2050.00		
Modulus of Elasticity, E (MPa)			35500.50		34600.34
Shear Modulus, G (MPa)			14688.60		14664.10
Poisson's Ratio, ν			0.18		0.18
			From hardened testing series		
Density, ρ (kg/m3)			2036.60 ± 8.50		
Modulus of Elasticity, E (MPa)			35989.10 ± 60.55		34876.23 ± 61.50
Max. tensile stress (MPa)			3.38 ± 0.15		2.87 ± 0.10
Displacement at failure (mm)			0.52 ± 0.35		0.42 ± 0.20
Max. shear stress (MPa)			10.04 ± 0.30		7.19 ± 0.50
Max. compressive stress (MPa)			44.22 ± 2.5		28.86 ± 2.0
Hill's yield ratio					
R11	R22	R33	R12	R13	R23
1.00	0.65	0.65	0.52	0.38	0.38

4.4 Results and discussion

4.4.1 Experimental load deformation analysis and numerical model validation

4.4.1.1 Vertical load path

The load-deformation curves of LBeam and TBeam under vertical load path are shown in **Figure 4.7**. It was observed that the peak flexural load of LBeam reached 8 kN, whereas TBeam exhibited a peak load of 11.53 kN, indicating 29.75% increase in load-bearing capacity. Additionally, the mid-point displacement at the peak load was found to be 1.73 mm for TBeam, which is almost two times less than the displacement observed in LBeam (i.e. 3.85 mm). It is noteworthy to mention that the TBeam exhibited a steep slope (7.488 kN/mm) in the force

versus displacement curves, whereas a gentle slope was observed in the case of LBeam (5.584 kN/mm). One potential explanation for this stiffness difference can be the load-bearing capability of the 3D printed beam. It can be seen (**Figure 4.9**) that the central vertical wall serves as the primary load-bearing element which transmits the flexural load to the supporting rollers on either side. In LBeam, the sharp intersection between the vertical and horizontal walls at the mid-span plays a role in load transmission to both ends. However, this region is susceptible to fracture under bending load, resulting in the formation of cracks (both front and rear) close to the vertical central wall (as shown in **Figure 4.10**). On the other hand, the TBeam with both horizontal and triangular infill patterns demonstrate superior load sharing when connected to the central wall. This can be observed from **Figure 4.10** where the rear crack in TBeam shifts approximately 17.7 mm away from the vertical central wall, while the front crack remains near the central wall (2 mm).

Considering the three critical parameters mentioned above (peak load, maximum mid-point displacement, and stiffness), the flexural deformation resistance capacity of both LBeam and TBeam was evaluated by integrating the area under the load-deformation curve up to the peak point. It was found that the LBeam exhibited higher (+17.7%) deformation resistance capacity despite having significantly lower values in peak load and maximum mid-point displacement compared to the TBeam.

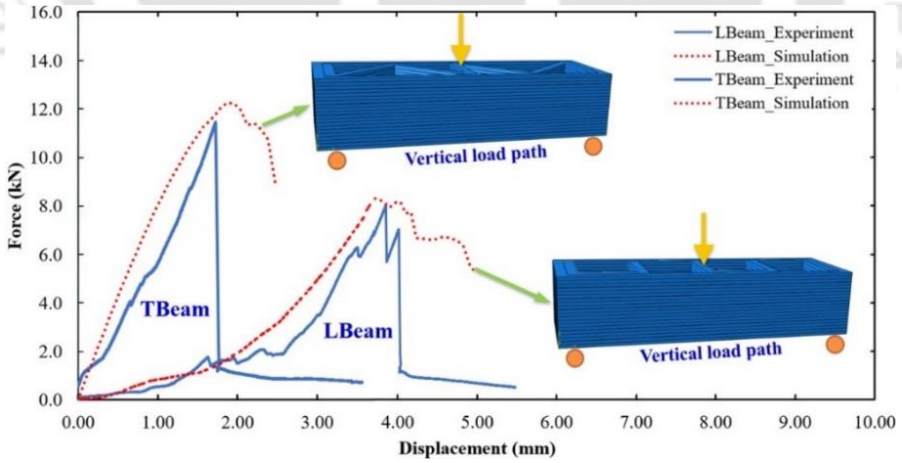

Figure 4.7 Comparison of bending load and midpoint deflection under vertical load path in LBeam and TBeam.

4.4.1.2 Transverse load path

A notable disparity between flexural strength of the LBeam and TBeam was witnessed in transverse loading direction. The load-deformation curves of LBeam and TBeam under the

transverse load path are presented in **Figure 4.8**. It was observed that the load bearing of TBeam increased significantly to 26.05 kN, which is more than twice (+125%) compared to vertical load path. Furthermore, the maximum mid-point displacement at the peak load was also considerably enhanced (+148%), from 1.73 mm to 4.30 mm. In contrast, the bending capacity of LBeam was marginally reduced due to a change in loading direction. In such a case, the peak load and maximum mid-point displacement of LBeam decreased from 8 kN to 5.46 kN (a reduction of 46.52%) and 3.84 mm to 2.67 mm (a reduction of 43.82%) respectively. This indicates that the load path is key, affecting the bending behavior of 3D printed lattice beams.

While considering the same loading direction, TBeam outperforms LBeam in terms of peak load and maximum mid-point displacement. The peak load of TBeam exhibits an increase of 377%, while the maximum mid-point displacement increases by 61%. With a substantial shift in the peak load, the flexural deformation resistance capacity of TBeam surpasses that of LBeam by approximately 500%. This can be experimentally observed from the crack pattern of the TBeam (**Figure 4.10(b**)), where upper cracks were formed close to the central wall, and the lower crack originates right at the intersection of the triangular and horizontal walls at the bottom. However, it is important to note that despite a higher load-bearing capacity of TBeam, it fails catastrophically at the peak load. Nevertheless, no sign of catastrophic failure was observed for other beams under vertical or transverse loading.

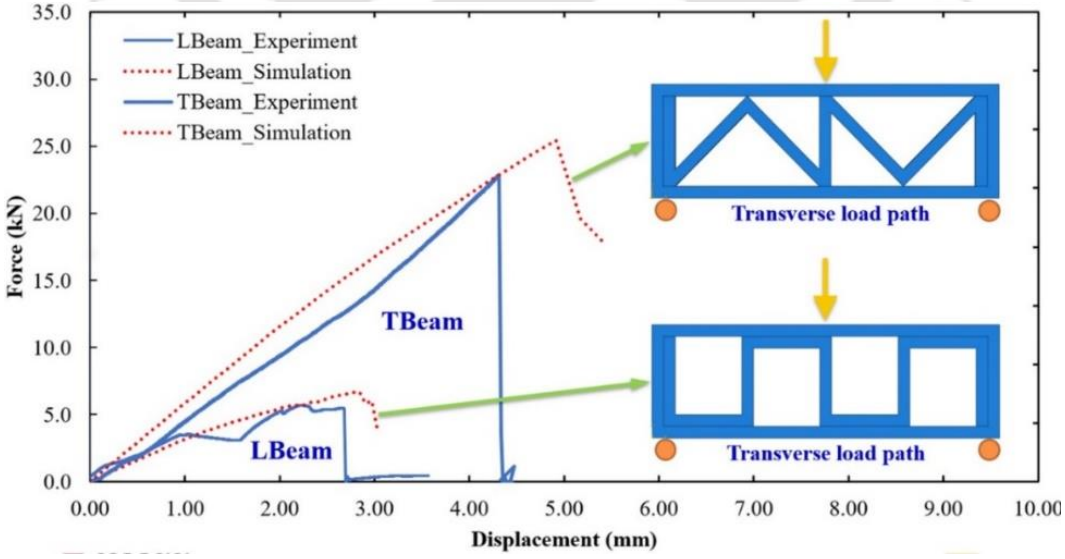

Figure 4.8 Comparison of bending load and midpoint deflection under transverse load path in LBeam and TBeam.

4.4.1.3 Model validation

It is clear from the FE results shown in **Figure 4.7** and **Figure 4.8** that a good agreement exists between experimental and numerical predictions in terms of peak load, and maximum mid-point displacement. However, there were slight discrepancies observed, including overestimation in the peak load and its corresponding displacement by the numerical model. Apart from overestimation, the post-crack behavior between experimental and numerical curves was also found to be different. It is important to note that the Hill yield criterion model employed in this study assumes fiber-reinforced cementitious mortar is a perfectly plastic solid after reaching the peak load. Therefore, this model is not designed to capture the behavior of the material beyond the peak point. Aside from this, the observed mismatch between numerical and experimental results is ascribed to several possible reasons. Firstly, in the numerical simulations, the beams were modeled as perfect printed layers without considering the presence of air voids within each filament. However, experimental studies by Chen and Das et al. [38, 39] have demonstrated the existence of air voids in 3D-printed concrete specimens and their characterization. The content, distribution, size, and shape of air void in printed samples can significantly affect the mechanical behavior of the printed beam. In other words, air voids within each printed layer can lead to non-uniform material distribution, altering the stiffness and deformation characteristics of the beam. Secondly, the print quality (standoff distance) and the method of material deposition, such as extrusion versus pumping, can have a significant impact on the behavior of 3D-printed concrete beams. Imperfections in the printing process, including gaps between layers, can indeed affect the load-bearing capacity and overall performance of the beams, which is shown in the authors' previous work [40]. Thirdly, the variations in the testing setup, including the boundary conditions and loading configuration, may also introduce such discrepancies.

4.4.2 Stress distribution

The total principal stress distribution (S1) was adopted to investigate and identify critical areas of stress concentration in the 3D-printed beams. The total principal stress distribution shown in **Figure 4.9** is mathematically written into a scalar quantity, which was calculated based on the material model. Generally, high equivalent stress was distributed around the mid-span region and its vicinity under vertical load paths. However, the stress concentration tends to spread to the whole beam when the direction changes from a three-point bending load to the

transverse load path. Herein, the highest stress represented by the red color is mainly concentrated in several corners and it can be observed that a higher value of maximum stress on the TBeam is reported on the left sidebar (see **Figure 4.9**). To be specific, the TBeam under the transverse load path experiences the highest equivalent stress, reaching a magnitude of 44 MPa. This is followed by the same beam subjected to the vertical load path, where the highest stress magnitude was measured at 39 MPa. Meanwhile, the magnitude of the principal stress in the LBeam only reaches magnitudes at around 32 MPa and 34 MPa for the vertical and transverse load paths, respectively. This indicates that the TBeam has (three times) higher bending capacity (see previous discussion) than LBeam.

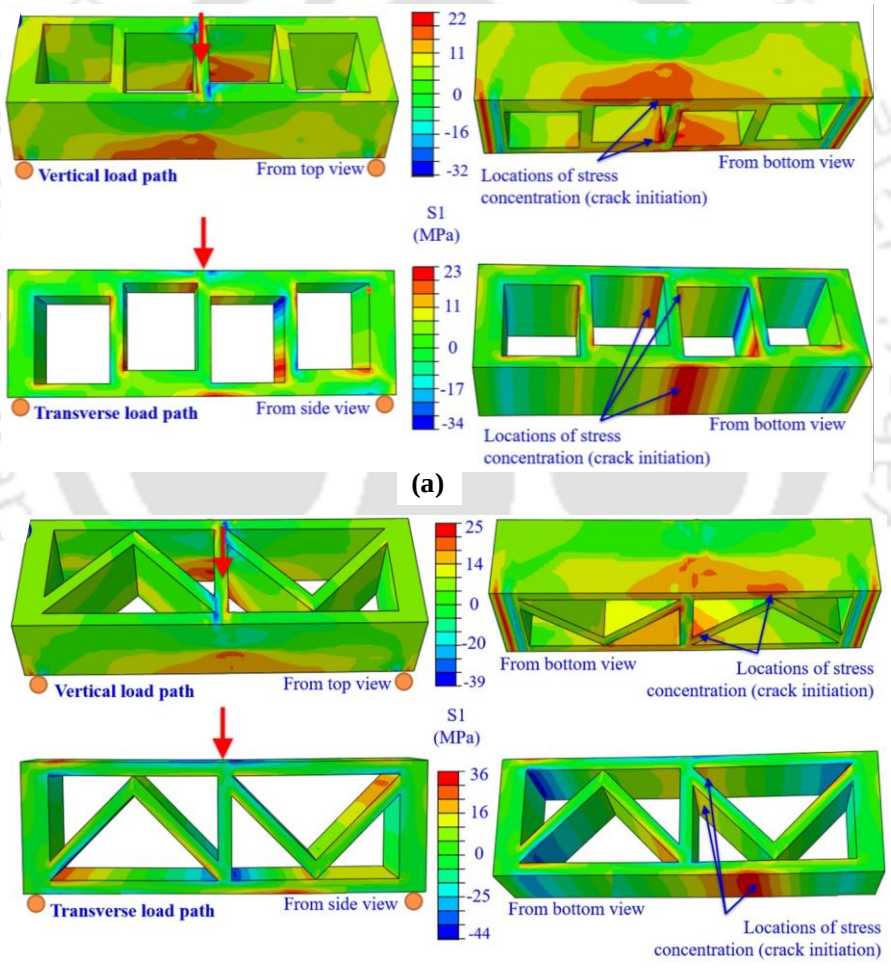

Figure 4.9 Total principal stress distribution (S1) on 3D-printed concrete beams with (a) lattice-infilled (LBeam) and (b) triangular-infilled (TBeam) pathways under vertical and transverse load path (From the bottom view of the beam on the right-hand side, red co color represents the locations of stress concentration from which cracks begin to propagate).

The intrinsic mechanism of stress distribution between the two beams (TBeam and LBeam) lies in transmission path of the flexural load to two supporting rollers on either side. The stress concentration mainly occurs on the middle wall of LBeam under transverse load path. When the beam starts to deform, the sharp edges at the mid-span (where the vertical and horizontal walls intersect) witness high-stress concentration. This is due to the bending load transmitted via the vertical center wall and this area may be prone to damage under the bending load. Meanwhile, the TBeam including both horizontal and triangular infill patterns show an even stress distribution as subjected to transverse load path. The flexural load transmits from the top to the bottom rollers via both vertical middle walls and triangular printing patterns. In this case, the region connecting the triangular and horizontal path indicates high-stress distribution.

4.4.3 Modes of fractures

In this section, fracture modes of the LBeam and TBeam were experimentally investigated. There were two typical fracture modes observed in the 3D printed lattice beams under a three-point bending load, i.e., straight-line and in-plane shear fracture (diagonal crack) [27, 41].

Under the vertical load path, the front and rear cracks in both 3D-printed beams exhibit different characteristics. The LBeam shows shear-like fracture pattern in the front crack and straight-line crack in the rear surface. The crack propagation occurs on the left-hand side of the midline in the LBeam, with crack tips located near the central line (**Figure 4.10(a**)). In contrast, the cracks appear and propagate on the opposite side of the TBeam under the same load path (see **Figure 4.10(b)**). Thus, the TBeam undergoes hybrid crack pattern, with the front crack indicating straight-line fracture and rear crack pointing towards an in-plane shear fracture. Moreover, the distance between the crack tips and midline differs for both front and rear surfaces of the TBeam.

Under the transverse load path, both LBeam and TBeam experience similar failure patterns. The crack location in the LBeam occurs in top and bottom surfaces but the TBeam was fractured to the right-hand side, in which the upper cracks are close to central wall, and the lower crack is located at the intersection of triangular and horizontal walls at the bottom surface (see **Figure 4.10(b)**). It implies that the triangular infill patterns in the TBeam facilitate a change in the load transmission direction from the upper roller to two bottom roller supports. In other words, the bending load was mainly transmitted through the triangular infills in the

TBeam, whilst the middle wall in LBeam supports the maximum bending load under vertical load path.

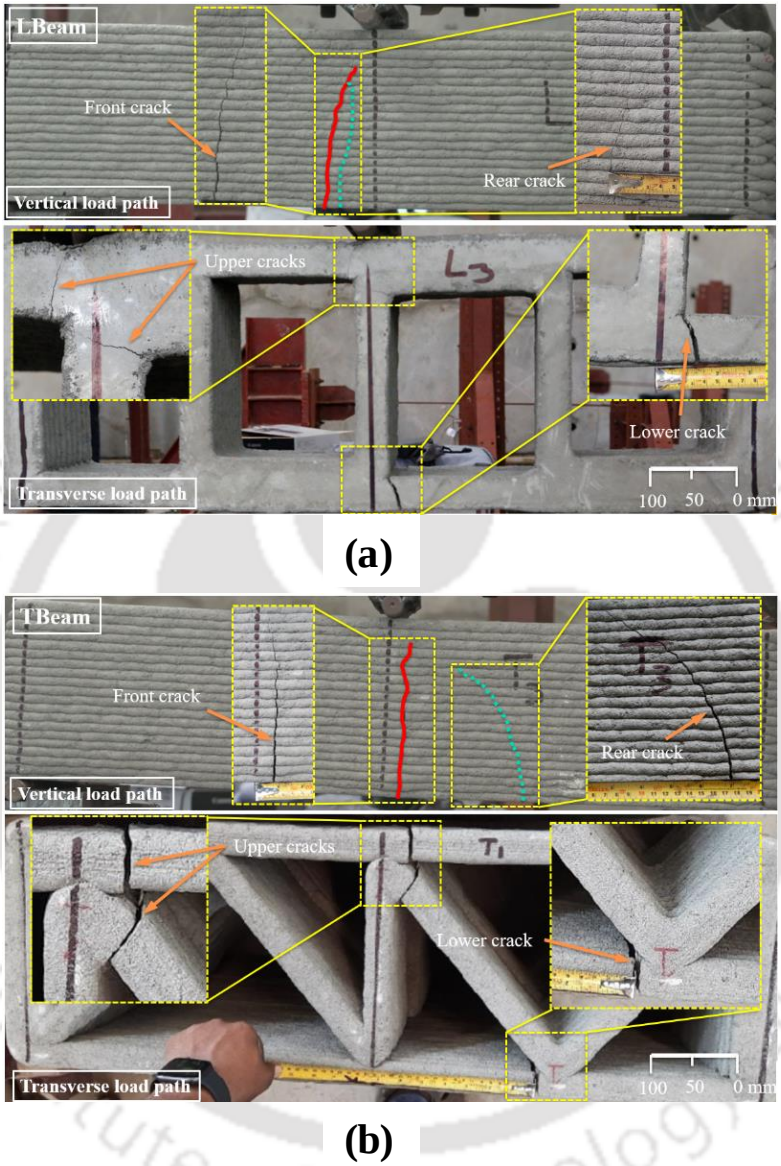

Figure 4.10 Fracture modes of hollow 3D-printed concrete beams with (a) lattice-shape (LBeam) and (b) triangular-shape (TBeam) infill patterns subjected to three-point bending load in vertical (first row) and transverse (second row) load path.

4.4.4 Effect of lattice configurations

In this section, the validated FE model was employed to predict the load-bearing capacity of LTBeam. **Figure 4.11(a)** shows bending capacity of all the beams under vertical and transverse load paths. During vertical loading, the peak load of all the 3D printed lattice beams was found

to be consistant with a variance(σ^2) of 2.04 kN^2, however a noticiable discrepancy (σ^2 of 86.65 kN^2) was found among those beams when subjected to transverse load path. The results shown in **Figure 4.11(a)** reveal that, under transverse load path, the TBeam outperformed in terms of the peak load compared to their counterparts (LTBeam and LBeam). Meanwhile, the LBeam still exhibits poor performance as the bending load hits the peak at 7.7 kN. The bending capacity of TBeam, and LTBeam in the transverse direction improved significantly (more than two times) compared to the vertical load path. The peak loads of TBeam (29.1 kN) was found to be around 250% higher than LBeam. This difference in the maximum bending load shows that the infill pattern of 'triangular' shapes can make lightweight concrete beams with higher bending load capacity than the 'lattice' shape. In other words, the direction of bending load has a major influence on the load-bearing capacity of beams with triangular infill. For the printed beams with lattice infill patterns, the load path direction has marginal influence on the peak load.

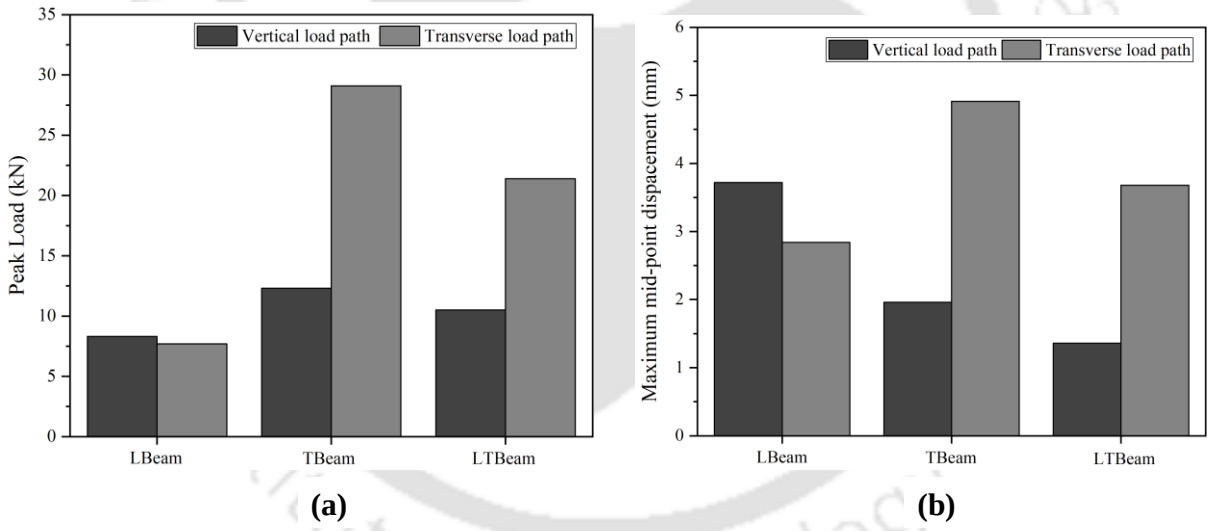

Figure 4.11 Maximum numerical bending load and (b) midpoint displacement of LBeam, TBeam, and LTBeam, under vertical and transverse load path.

While comparing the mid span deflection at break under vertical load path (see **Figure 4.11(b)**), the LBeam provides the highest value of maximum mid-point deflection at 3.72 mm. The other three beams (TBeam, LTBeam, and SBeam) deflect less. However, the LBeam failed under transverse load path when the beam deflects only at 2.84 mm (see the orange bars in **Figure 4.11(b**). In that direction, the TBeam, SBeam, and LTBeam not only have better load-bearing performance but also deform more. Specifically, the deformations at the break of TBeam and

SBeam are 4.91 mm and 5.06 mm, respectively, while the LTBeam reaches its peak at roughly 3.7 mm. These values are almost three to four times higher in case of vertical load path.

Based on the experiment and FE simulation results, it manifests that the transverse loading in hollow 3D-printed concrete beams with triangular-shape infills can have a better mechanical performance compared to vertical loading. To further improve the performance, new simulation-based designs were proposed to further investigate the bending performance of lightweight 3D-printed lattice beams. These new infill patterns are based on the results of the topology optimization problem of three-point bending beam [42], as shown in **Figure 4.12(a, b)**. To make the beam comparable, the beam size was kept constant. Generally, TBeam shows the highest bending performance compared to other beams as discussed in previous sections. Hereafter, the TBeam's bending performance under the transverse load path (peak load, printing contour length, and maximum mid-point displacement) was used as a reference for the comparison. Only the infill printing patterns were altered, while the border printing path was kept constant (see **Figure 4.12(c**)). For simplification, half of the beam is shown within this section due to symmetry.

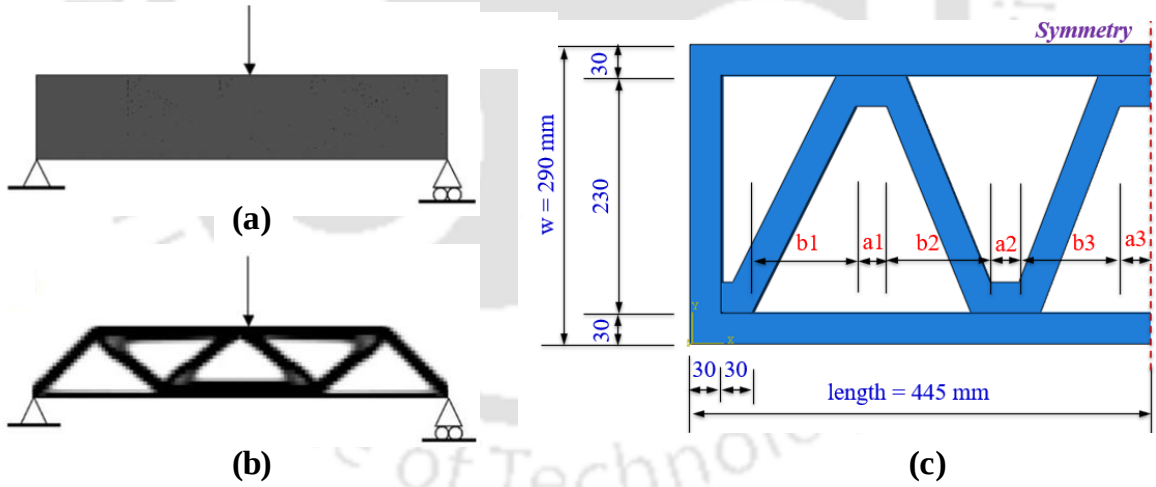

Figure 4.12 Example of topology optimization of a three-point bending beam: (a) full design domain, (b) resulting deterministic topology optimized beam [42], (c) proposed pattern-based topology optimization model for 3D-printed concrete beams (symmetric beam).

The infill printing patterns were proposed according to the outcome of the topology-optimized beam (see **Figure 4.12(b)**). There is often high-stress distribution at the intersection between infill printing patterns and outer border printing path as witnessed in Section 4.4.2. Therefore,

the horizontal to the triangular ratio of printing patterns (γ) was taken into consideration in order to elucidate the influence of sharp edges on the bending performance of 3D-printed beams. As listed in **Table 4.6**, different infill patterns (10 cases) were investigated. The ratio (γ) increases from 0 to 0.638 (from case 1 to case 10). Herein, there was an increment in the total length of horizontal printing patterns, while the total width of triangular printing patterns decreased. In short, a topology optimization model was employed with an objective function aimed at maximizing the flexural performance of a 3D-printed beam under transverse loading condition. The optimization was performed within a fixed design domain defined by the outer contour to control material usage. The design variable was the material distribution within the infill region, represented through ten distinct lattice configurations derived from prior experimental and numerical findings (Sections 4.4.1–4.4.3).

Table 4.6 Different proposed pattern-based topology optimization models for 3D-printed beams

Parameters	Case 1	Case 2	Case 3	Case 4	Case 5	Case 6	Case 7	Case 8	Case 9	Case 10
a1 (mm)	0	15	30	30	30	0	30	60	30	30
a2 (mm)	0	30	30	30	30	60	30	30	30	90
a3 (mm)	0	15	15	15	30	30	30	15	60	30
a = a1 + a2 + a3 (mm) (*)	*0*	*60*	*75*	*75*	*90*	*90*	*90*	*105*	*120*	*150*
b1 (mm)	130	120	100	115	100	100	85	110	70	90
b2 (mm)	130	120	100	115	100	100	85	110	70	90
b3 (mm)	125	85	110	80	95	95	125	60	125	55
b = b1 + b2 + b3 (mm) (**)	*385*	*325*	*310*	*310*	*295*	*295*	*295*	*280*	*265*	*235*
γ = a/b (***)	*0*	*0.185*	*0.242*	*0.242*	*0.305*	*0.305*	*0.305*	*0.375*	*0.453*	*0.638*
Contour length (mm)	3820	3888	3903	3906	3921	3921	3924	3945	3965	4001

Note: * *Total length of horizontal printing patterns*

** *Total width of triangular printing patterns*

*** *Horizontal to triangular ratio of printing pattern*

The results of different infill patterns are illustrated in **Figure 4.13** (cases 1, 3, 5, 7, 9) and **Figure 4.14** (cases 2, 4, 6, 8, 10). As reported in the previous section, the peak load of TBeam was 29.10 kN (under the transverse load path) and therefore, the red dash-line indicates the value of 29.10+0.0 kN, thus taken as baseline for comparison. Herein, the case provides a lower performance compared to the TBeam's performance as indicated by the brown bar. Meanwhile, the blue bars manifest higher performance.

In general, case 1 without horizontal infilled patterns exhibit lower bending performance. The peak load starts to increase as the horizontal infills get bigger. It is, however, not the case when longer horizontal printing. This is because there is a gradual decrease in the maximum bending load in the beams with high value of horizontal printing patterns. The highest bending load (+60%) were witnessed in case 3 and 4, in which the total lengths of horizontal and triangular infill patterns are 75 mm and 310 mm, respectively (see **Table 4.6**). In this case, the horizontal-to-triangular ratio of the printing pattern (γ) is 0.242 (about 25%), in which the lengths of each horizontal printing (a1, a2, and a3) are equal to the width of printed filament (30 mm). Within 10 proposed cases, there are only three cases exhibiting lower bending performance compared to the TBeam's performance. In such cases, it can be seen that sharp edges between triangular and horizontal pathways (see case 1 and case 6) and long horizontal infill length near the mid-span (see case 9) can be the reasons for lower performance.

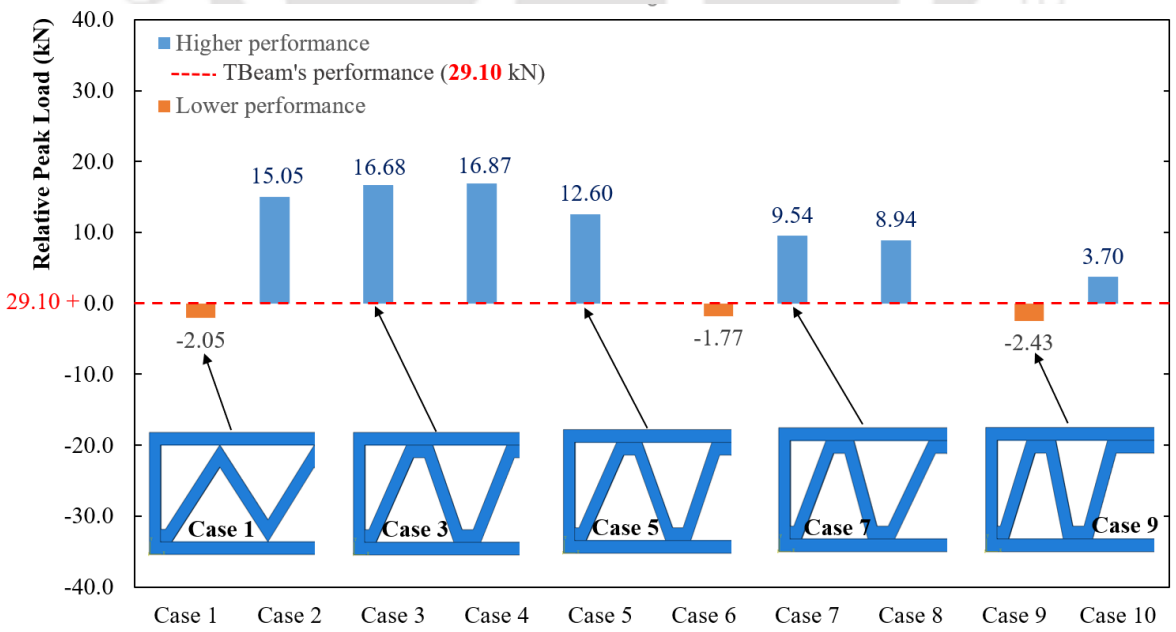

Figure 4.13 Relative peak loads in different cases compared to TBeam's peak load (red dash-line represents the peak load of TBeam (29.10 kN)).

In terms of maximum midpoint displacement (see black line in **Figure 4.14**), case 1 provides the highest value (6.42 mm) followed by case 6 (5.80 mm). Apart from those two cases, cases 3 and 4 also give high midpoint displacement, while 4.91 mm displacement was recorded in case of the TBeam (see red dash-line in **Figure 4.14**). The midpoint displacement in other cases were lower than the TBeam, among which the displacement in case 5 was the lowest (i.e. 4.06 mm). When considering both factors (i.e., peak bending load and maximum midpoint displacement) the case 3 and 4 show best performance, in which the horizontal to triangular ratio of the printing infill pattern (γ) is about 0.24 (see **Table 4.6**).

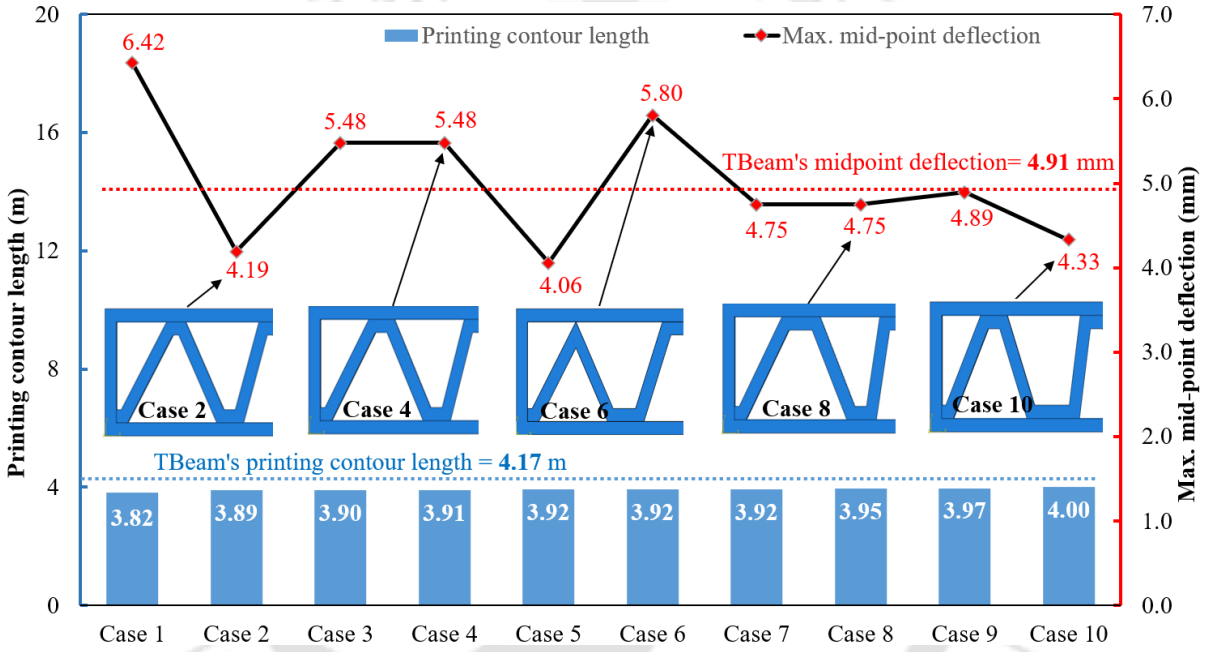

Figure 4.14 Printing contour length (blue bars) and maximum mid-point deflection (black line) of different cases compared to TBeam's results (blue and red dash-line, respectively).

It is also interesting to note that the printing contour length in each proposed case is always lower than the TBeam, as illustrated in blue bars in **Figure 4.14**. This leads to the reduction of weight of 3D printed lattice beams. In other words, 3D-printed lattice beams become lighter when reducing the horizontal length of infill patterns. It can be also deduced that the 3D-printed lattice beams with infill patterns based on the topology optimization (see **Figure 4.12(b)**) perform better than the TBeam and other beams (LBeam, LTBeam, and SBeam) under three-point bending test. Based on the results of the study, 3D printed beam infilled by patterns proposed in case 3 and 4 (the horizontal to triangular ratio of the printing pattern is about 25%) could be the optimal shape for structures subjected to three-point bending loading.

4.5 Summary

This chapter investigates the impact of infill patterns on the flexural strength and deformation behavior of 3D-printed lattice beams subjected to two distinct loading directions. Experimental studies were conducted on two infill patterns, with a focus on their effects on peak load, midpoint displacement, stiffness, and flexural deformation resistance. The results revealed that under transverse loading, the TBeam outperformed the LBeam, achieving a substantial 377% increase in peak load, 61% higher midpoint displacement, and approximately 500% greater flexural deformation resistance. In contrast, under vertical loading, the LBeam exhibited a 17.7% higher flexural deformation resistance, despite having a lower peak load and midpoint displacement compared to the TBeam. FE models, accounting for material anisotropy, successfully simulated the mechanical behavior observed in the experiments, providing accurate predictions of failure. The FE model was subsequently employed to predict the load-bearing capacity of the lattice-triangular infill pattern. Based on the understanding developed, further parametric studies were performed by varying the ratio of horizontal to triangular printing pattern length. This optimization led to a substantial improvement in peak load (60%) and a maximum midpoint displacement (12%), all while reducing the printing contour length. These findings underscore the critical role of infill design and loading direction in determining the mechanical performance of lattice beams, positioning lightweight, optimized 3D-printed beams as viable solutions for advanced construction applications.

CHAPTER 5

Thermal performance of 3D printed concrete wall with lattice infill configurations

A comprehensive investigation into the thermal performance of 3D-printed lattice infilled walls was performed in this chapter. Through 3D and 2D CFD numerical modelling, the underlying mechanism, direction and magnitude of heat flow affecting thermal transmittance (U value) of lattice walls were first analysed. The proposed numerical model demonstrates strong alignment with 3D printed prototype wall experimental results. Based on the model derived physical phenomena, novel composite lattice wall was later configured with insulation material demonstrating superior performance (minimum U-value of 0.79 W/m²K), surpassing the studied lattice configurations.

A portion of this chapter has been published in:

1. **Dey, D.**, Panda, B., Shukla, Y., & Rawal, R. (2025). A comprehensive assessment of thermal performance of 3D printed concrete lattice walls. Progress in Additive Manufacturing, 1-18. https://doi.org/10.1007/s40964-025-01042-3.
2. **D. Dey**, B. Panda, Y. Shukla, R. Rawal. 2024. Process for making concrete 3D printed walls with diverse lattice designs. Indian Patent, filed February 08, 2024. Patent filed. Patent Application No.: 202431008465 (PUBLISHED).

5.1 Introduction

This chapter presents a comprehensive study combining numerical modelling and experimental validation to evaluate the thermal performance of 3D printed lattice infilled walls (refer to **Figure 2.14**). The study systematically integrates factors such as wall geometry (aspect ratio), material properties, and computational fluid dynamics (CFD) modeling in 2D and 3D frameworks. This approach improves the predictive accuracy of the numerical models and provides a deeper understanding of the complex heat transfer mechanisms inherent in lattice wall. Building on these insights, modified lattice wall configurations incorporating insulation materials were proposed and evaluated for their thermal performance and cost-effectiveness.

5.2 Experimental methods and numerical model

5.2.1 Lattice wall design and material properties

The scope of this study is centred on 3D printed lattice wall configurations with outer dimensions fixed at 900 mm × 300 mm × 900 mm (length × width × height). The selection of such dimension serves as framework, thus enabling a systematic investigation of lattice wall configuration as described in section 3.3. The aspect ratio of the wall (ratio of height to width) and length to width ratio affects both the natural convection patterns and the radiation exchange within the enclosure. Hence in order to capture the realistic long wall configuration, the width was considered significantly less compared to its length and height. The case study considered in this work is classified under vertical cavity with side wall heating (see **Fig. 5.1(a))**, where opposing sides of the walls were maintained at different temperatures and other parts of the walls are insulated from the surroundings to analyse the steady-state 1D heat transfer problem [141].

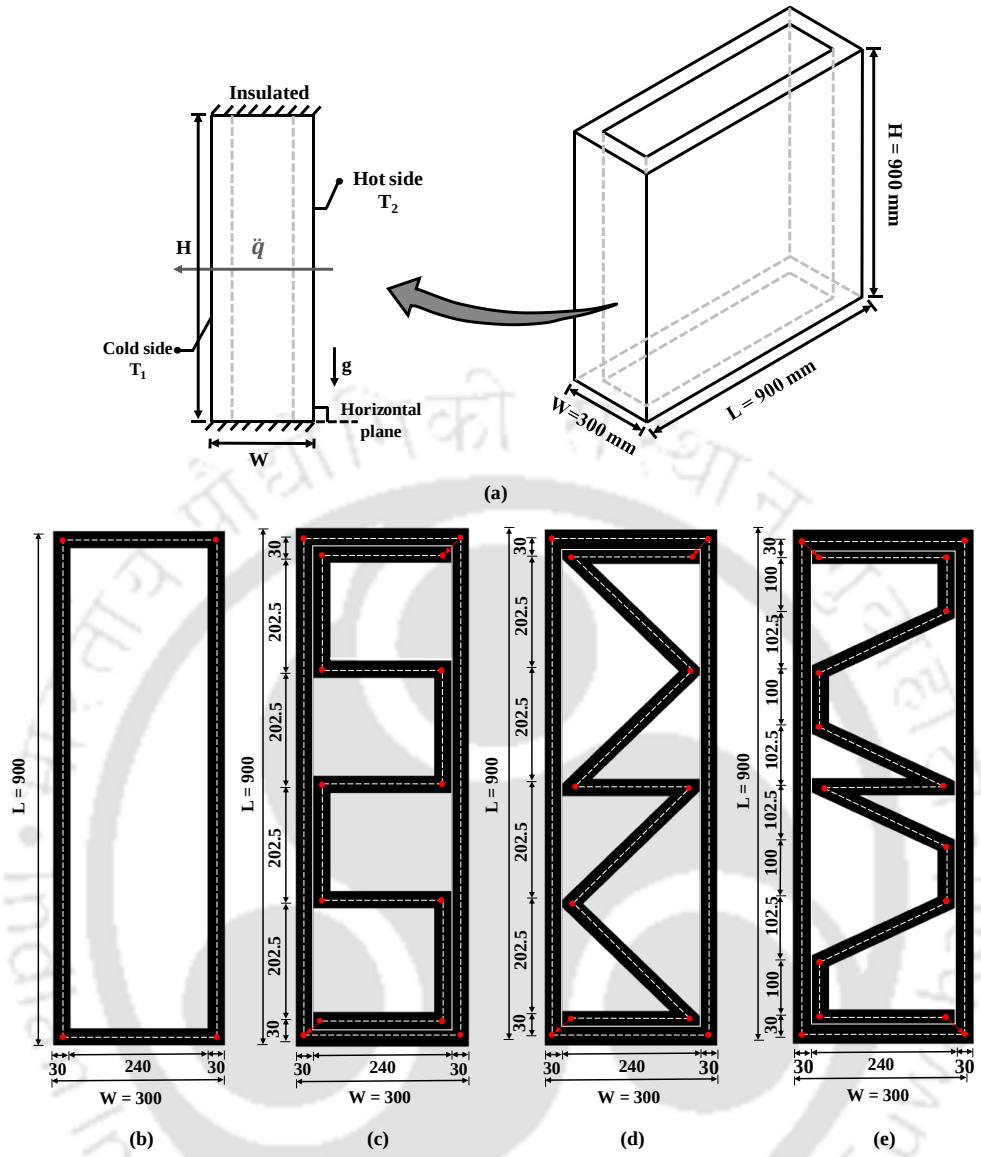

Figure 5.1 (a) 3D representation of cavity wall with side wall heating and 2D geometrical details of (b) RH, (c) L, (d) T, and (e) LT lattice wall configurations (all dimensions are in mm).

In the present study, thermal performance of rectangular hollow (RH) along with three most commonly used lattice wall configurations namely L, T and LT were studied, where the RH configuration was considered as base model for comparative analysis. It is important to highlight that L, T, LT lattice walls are designed with a constant cavity percentage of 54% and these configurations were earlier studied for their mechanical performance in **Chapter 4**. The detailed 2D geometry of the lattice walls are presented in **Fig. 5.1(b-e)**, where the dotted line represents the print path and arrow mark delineated the continuous print path which are fed into the 3D printer in form of G-code.

5.2.2 Materials

The load-bearing 3D printable material (modified OR mix), characterized in Chapter 4, was employed to print the lattice walls. The thermo-physical properties of the concrete, insulation material, and air, which are essential for the numerical simulation model, are presented in **Table 5.1**.

Table 5.1 Thermo-physical properties of the materials

Material	Dry Density (kg/m^3)	Thermal Conductivity (W/mK)	Specific Heat (J/kgK)	Emissivity	Viscosity (kg/m.s)
Concrete	2050	1.6115	780	0.9	-
Extruded Polystyrene (XPS)	24	0.0350	1340	-	-
Air	Ideal gas	0.0263	1007	-	1.789E-05

5.2.3 3D concrete printing and testing of thermal properties of lattice wall

The selected mix was printed using the gantry-based 3D printer with a circular nozzle of 20 mm diameter. The stand-off distance was kept at 10 mm and layer width of 30 mm was selected to improve the stability and inter-layer bonding. The geometry of the T configuration (as depicted in **section 5.2.1**) was modelled in Fusion 360 platform and the 3D model was then sliced into layers followed by G-code preparation. Resistance temperature detectors (RTDs) were placed (at four quadrants and two triangular cavities) during printing in three different stages as depicted in **Figure 5.2**. The printing was completed at a constant speed of 3,600 mm/min and wall prototypes were moist cured for 28 days in laboratory conditions. Subsequently, the printed walls were exposed to sunlight for three days to ensure complete drying for the thermal testing using Guarded Hot Box (GHB) apparatus.

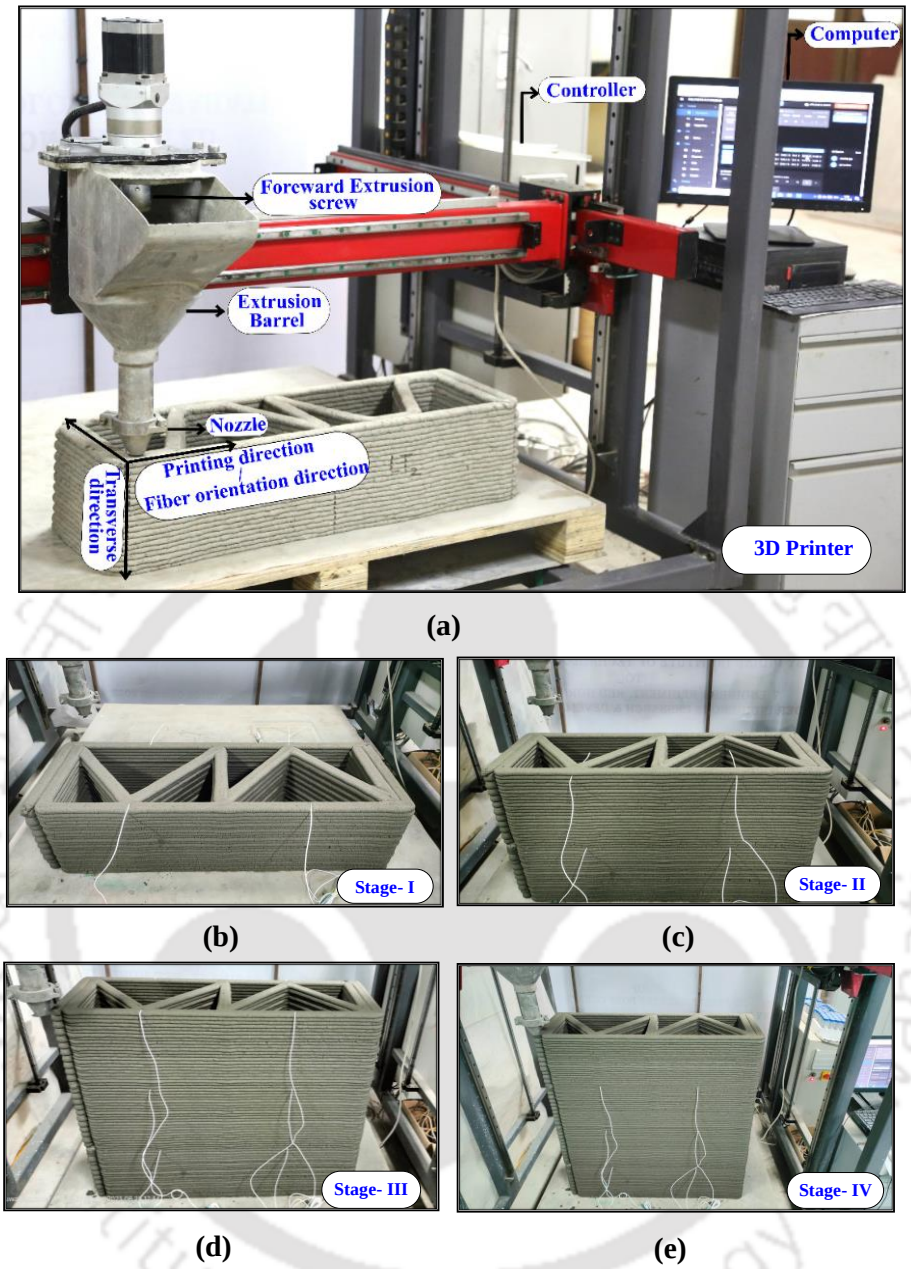

Figure 5.2 (a) 3D concrete printer set up and (b-d) sensor integration steps during 3D printing.

The GHB apparatus was custom-made to operate within a range of 0.1 to 5.0 W/m²K in accordance with ASTM C1363 [142]. The sectional illustration of the apparatus is shown in **Figure 5.3(a)** where the specimen frame is sandwiched between the guard chamber (inter-connected with metering chamber) and climate chamber. The 3D printed wall specimen was placed in the specimen frame with the gaps filled with Extruded Polystyrene (XPS) insulation strips sealed using silicone sealant as shown in **Figure 5.3(b)**. To maintain the steady-state, environmental condition on both sides of the specimen was held constant with average

temperature of 35 ℃ (308 K) on the hot side and 15 ℃ (288 K) on the cold side. The specimen was kept under observation for 48 hours to stabilize the temperature across the specimen followed by the measurement of heat flow through the wall specimen. Further details of the GHB set up, its calibration and losses calculation can be found in [142].

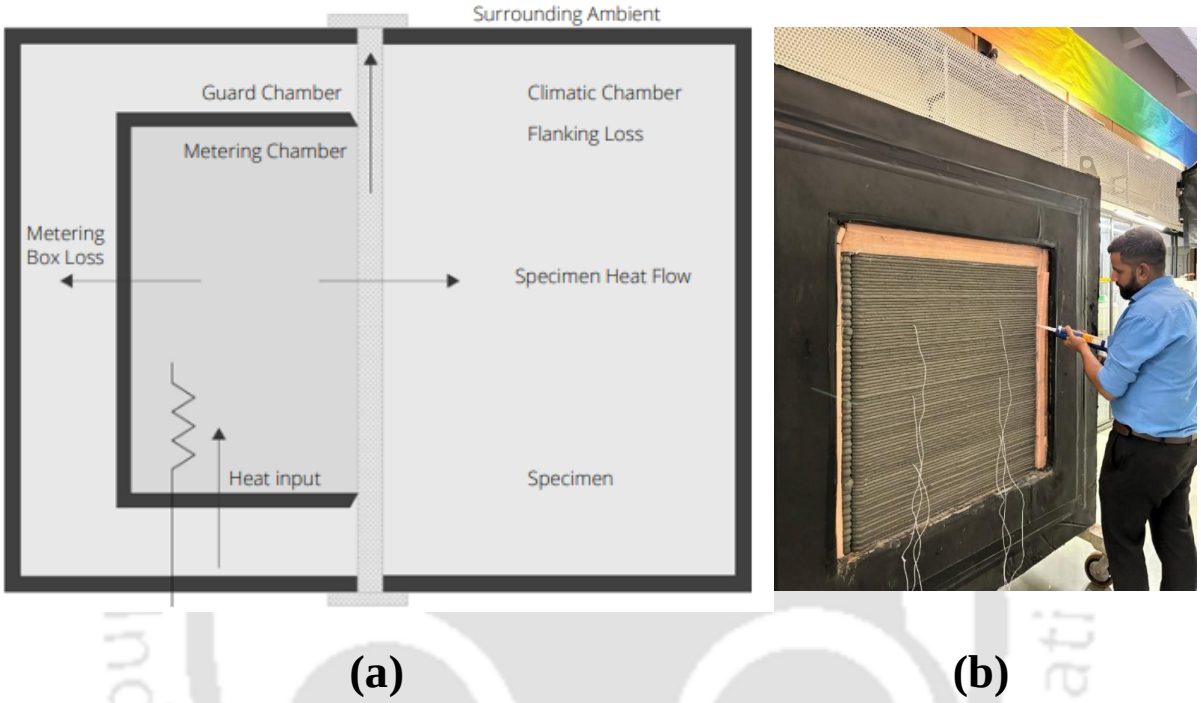

Figure 5.3 Experimental method for concrete wall thermal property measurement: (a) sectional illustration of the Guarded Hot Box apparatus [143], (b) example of 3D printed lattice wall mounted in the testing frame of GHB.

5.2.4 CFD model and experimental validation

A steady-state thermal analysis of the 'T' configuration lattice wall was carried out by commercial finite volume method using ANSYS Fluent workbench. Original 3D and 2D part geometries were created, with the part assigned as solid or fluid regions as per the design. Grid independence test was done varying the mesh size as input parameter and output as the heat flux for both 3D and 2D simulation case. In case of 3D simulation, it was noticed that there was a significant reduction in the heat flux value up to 8 mm mesh size. With further reduction, the deviation was less than 0.1% (see **Figure 5.4**). Hence a mesh size of 6 mm was chosen for the 3D analysis. In case of 2D simulation, the grid convergence was found to be at 0.6 mm owing to its smaller size.

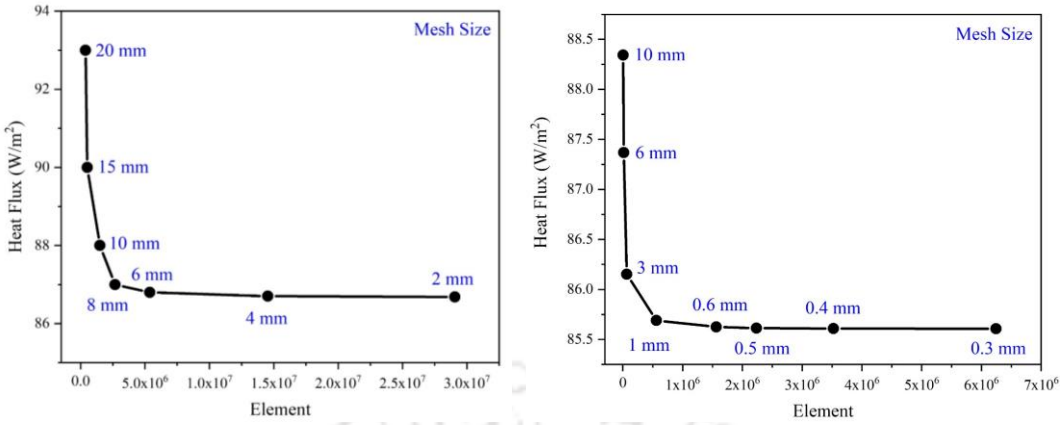

(a) **(b)**

Figure 5.4 Mesh convergence result of T configuration for (a) 3D model and (b) 2D model.

Followed by proper meshing, discretized elements were then shifted to the CFD solver with double precision accuracy for the simulation. A pressure-based solver, suitable for fluid flow and heat transfer problems was chosen with gravity given along the negative Z direction (height) for 3D geometry and negative Y direction (length) for 2D geometry. The fluid (air) inside the cavity was assumed to be Newtonian and incompressible with constant physical properties except for it's density. To account conduction and convection phenomena, energy and laminar flow model (with ideal gas assumption) was activated, which solves continuity equations, Navier–Stokes equations, and the energy equations (1), (2), (3) [101].

$$\frac{\partial \rho}{\partial t} + \frac{\partial (\rho u_i)}{\partial x_i} = 0 \tag{13}$$

$$\frac{\partial (\rho u_i)}{\partial t} + \frac{\partial (\rho u_i u_j)}{\partial x_j} = \frac{\partial P}{\partial x_i} + \frac{\partial \tau_{ij}}{\partial x_j} - \rho g \delta_{ij} \tag{14}$$

$$\frac{\partial}{\partial t}\rho\left(C_v T + \frac{u_i u_i}{2}\right) + \rho u_j \left(C_v T + \frac{u_i u_i}{2}\right) = -\rho g u_2 - \left(P \frac{\partial u_j}{\partial x_j} + u_j \frac{\partial P}{\partial x_j}\right) - \frac{\partial q_i}{\partial x_i} + \frac{\partial (u_i \tau_{ij})}{\partial x_j} \tag{15}$$

where ρ (kg/m^3) is the density, t (s) is the time, u_i (m/s) is the velocity vector in the i direction, T (K) is the temperature, P (Pa) is the pressure, g (m/s^2) is the gravitational acceleration, C_v (J/(kg.K)) is the specific heat at constant volume; and τ_{ij}, q_i; and K are the viscous stress tensor in (N/m^2), heat flux q along i direction in (W/m^2), and the thermal conductivity in (W/(m.K)) respectively which are defined in **equations (16) – (18)** respectively.

$$\tau_{ij} = \mu\left(\frac{\partial u_i}{\partial x_j} + \frac{\partial u_j}{\partial x_i} - \frac{2}{3}\delta_{ij}\frac{\partial u_k}{\partial x_k}\right) \tag{16}$$

$$q_i = -K\frac{\partial T}{\partial x_i} \tag{17}$$

$$K = \rho \alpha C_p \quad (18)$$

Where μ the dynamic viscosity (kg/(m s)), δ_{ij} is the kronecker delta, α is the thermal diffusivity (m^2/s), and C_p is the specific heat at constant pressure (J/(kg K)).

In conjunction with convection, discrete ordinates radiation model (DORM) was employed to consider the radiation inside the cavity [144]. Subsequently, Neumann-Dirichlet type boundary conditions were used at various cross sections of the wall. A constant temperature of 308 K and 288 K was applied in the two outer wall surfaces i.e. hot and cold side (Fig.1(a)) respectively to create a temperature difference (ΔT) of 20 K as per ISO regulation. The boundary condition at the internal solid-fluid interface was coupled and no slip condition was given for the fluid near the cavity wall. All other wall boundaries were insulated, neglecting the heat flux in any other directions.

A comprehensive model was employed in this study including three most common heat transfer modes: conduction (energy equation active), convection (laminar flow model with the ideal gas assumption), and radiation (discrete ordinate radiation model active). Upon convergence of the governing equations, the weighted average heat flux of the hot wall was considered to calculate U value of the lattice walls. The U value in case of 3D and 2D simulation were found to be of close approximation to each other (with a minimal deviation of 0.16%), which is attributed to the adherence of the high aspect ratio of the 3D model. The temperature at different locations of the 3D printed specimen were captured from the GHB testing and compared with the temperatures generated through numerical simulation. The results shown in **Figure 5.5** confirmed the agreement between the FE simulations and experimental data with an average error of 0.34%.

Following this, the thermal resistance of the wall specimen was calculated (using the heat balance **equation 19**), based on the data obtained from the GHB apparatus (see **Table 5.2**).

$$Q_{aux} + Q_{mw} + Q_{fl} = Q = (A.\ \Delta T)/R \quad (19)$$

Where,

Q_{aux} = Net heat flow due to the fan, heater, and cooling coil ($Q_c + Q_{h1} + Q_{h2} + Q_f$), in W

Q_{fl} = Flanking loss ($Q_{fl,\ m\text{-}g} + Q_{fl,\ m\text{-}c}$), in W

Q = Heat flow through the specimen, in W

R = Thermal resistance of the specimen, in m^2K/W

U = Thermal transmittance (1/R), in W/m^2K

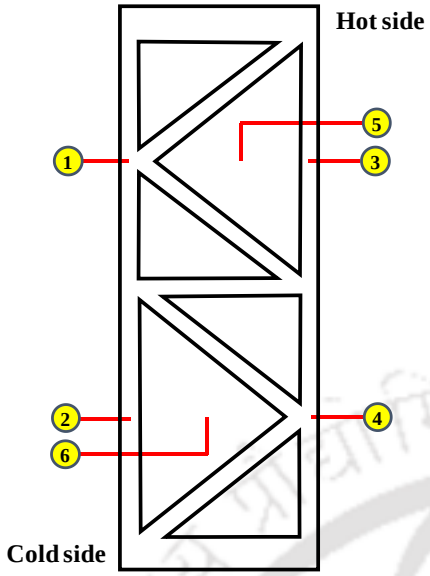

Layer number	Thermocouple position	Experimental temperature (K)	Simulated temperature (K)
23	1	288.1	288.5
	2	288.0	288.5
	3	307.8	307.1
	4	307.8	307.1
45	5	298.2	300.0
	6	298.1	294.8
68	1	288.0	288.8
	2	288.0	288.8
	3	307.8	307.2
	4	307.7	307.2

Figure 5.5 Experimental vs simulated temperature at different location of the 3D printed lattice wall.

Table 5.2 Variables used for the calculations experimental U value in the GHB set up.

Symbol	Description	Value	Unit
Q_c	Net heat removed by the heating coil	0	W
Q_{h1}	Net heat added by the air heater (to maintain temperature in the metering chamber)	16.17	W
Q_{h2}	Net heat added by the plate heater (to maintain temperature in the metering chamber)	39.34	W
Q_f	Net heat added by the fan	1.23	W
Q_{mw}	Metering box wall loss (edge loss)	0.14	W
$Q_{fl,\ m\text{-}g}$	Flanking loss from the metering chamber to the guard	0.12	W
$Q_{fl,\ m\text{-}c}$	Flanking loss from the metering chamber to the climate chamber	0.18	W
A	Metered area of heat flow	0.980	m^2
ΔT	Surface temperature difference across the specimen	20	℃

The thermal resistance is inverted to find thermal transmittance (U-value), which is equal to 2.92 W/m²K and in comparison with the simulated U-value (= 3.025 W/m²K (detailed analysis provided in Section 5.3.1)) it shows a very good alignment with maximum deviation less than 5%. It is thus clear that the proposed model could effectively evaluate the thermal performance of lattice wall with sufficient accuracy. The marginal disparity between the numerical and experimental outcomes may be ascribed to the material and/or printing imperfection, heat losses from the specimen frame to the metering chamber, climate chamber and other variation in the testing set up which could not be captured in the calibration and heat loss measurement.

5.2.5 Costing analysis

The costing analysis of 3D printed walls with varying lattice configurations and insulation infill strategies was conducted by considering both material and operational expenses. The raw material quantities for each mix design were converted to kilograms per cubic meter (kg/m^3), and the total material cost was computed by multiplying the quantity of each raw material by its respective market price, as presented in **Table 5.3**. The 3D printing process utilized a customized gantry-based 3D printer, supported by an 80-liter concrete pan mixer and a cavity pump as auxiliary equipment. Since the equipment represents a one-time capital investment, its cost was excluded from the analysis. However, the electricity consumption of these components was calculated based on their current and voltage ratings, along with the mixing and/or printing duration, using the prevailing electricity tariff rates in the Indian market (see **Table 5.4**). The operation of the 3D printer and associated equipment required one highly skilled operator and two semi-skilled personnel, with labour costs of 108 INR/h and 84 INR/h, respectively. Additionally, the XPS insulation material, priced at 27,268 INR per cubic meter, along with its installation cost of 806.67 INR per cubic meter, was incorporated into the analysis. By integrating material costs, energy consumption, labour charges, and insulation expenses, the total costs for each lattice configuration, with and without insulation infill, were calculated and are detailed in the appendix A. Additionally, the Cost Performance Index (CPI) was calculated to quantify the cost incurred for each unit of thermal performance improvement. The CPI is expressed as:

$$CPI = {}^{\Delta C}/_{\Delta U} \tag{20}$$

Where, ΔU represents the reduction in thermal transmittance, and ΔC is the incremental cost associated lattice configuration change and insertion of insulation material relative to the RH2M configuration, which serves as the reference.

Table 5.3 Material cost calculation.

Raw material	Raw material Cost (INR/kg)	Material used (kg/m^3)	3D printable material cost (INR/m^3)
OPC	9.10	745.44	6783.47
River sand	1.14	1242.39	1416.33
SF	37.60	82.83	3114.27
HPMC	638.40	1.24	793.14

SP	125.00	5.80	724.73
PVA fiber	95.00	2.5	237.50
TOTAL			13069.46

Table 5.4 Power requirement for calculation of electricity consumption.

Machine	Manufacturer	Power ratings	Electricity tariff (INR/kWh)
Concrete 3D printer	Custom made	32A, 230 V	8.60
Mixer	AIMIL (80-liter)	5 HP	
Pump	MAI international	1500 W	

5.3 Results and Discussions

5.3.1 Thermal transmittance analysis of 3D printed lattice walls

Figure 5.6 presents the U value of rectangular hollow (RH) configuration along with three lattice configurations (L, T, LT configuration), as obtained using the proposed numerical model. The RH configuration exhibits highest U value (4.69 W/m²K) and among lattice configurations, the T configuration exhibits lowest U value (3.02 W/m²K) followed by LT (3.35 W/m²K) and L configuration (3.50 W/m²K). The results have shown that a change in the configuration of wall cavities could decrease the thermal transmittance up to 35.60%. To further elucidate these findings, detailed heat transfer study was conducted considering the three heat transfer modes.

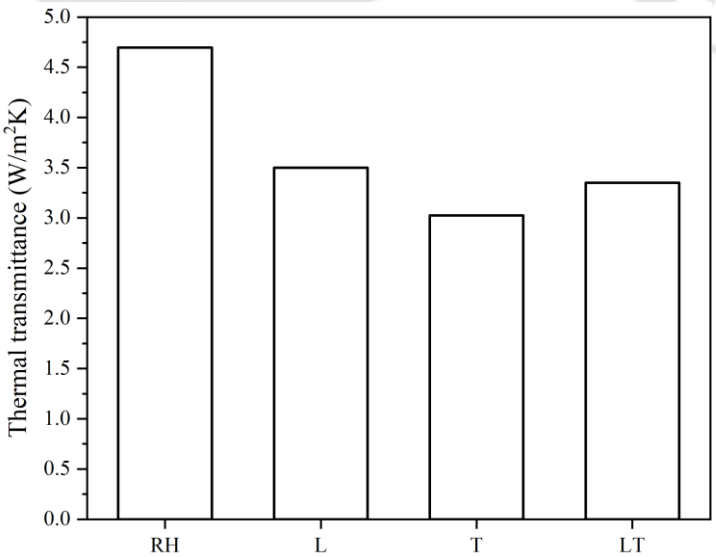

Figure 5.6 Thermal transmittance of RH, L, T, and LT configurations.

Figure 5.7 shows the heat flux distribution of four configurations and from the contour graph, it can be seen that the heat flux is concentrated significantly near the boundary of the cavities and hot/cold side of the wall. As anticipated from the measured U value, the RH configuration was found to have highest heat flux of 93.92 W/m^2 followed by L, LT and T configuration with heat flux of 70.00 W/m^2, 67.00 W/m^2, and 60.50 W/m^2 respectively.

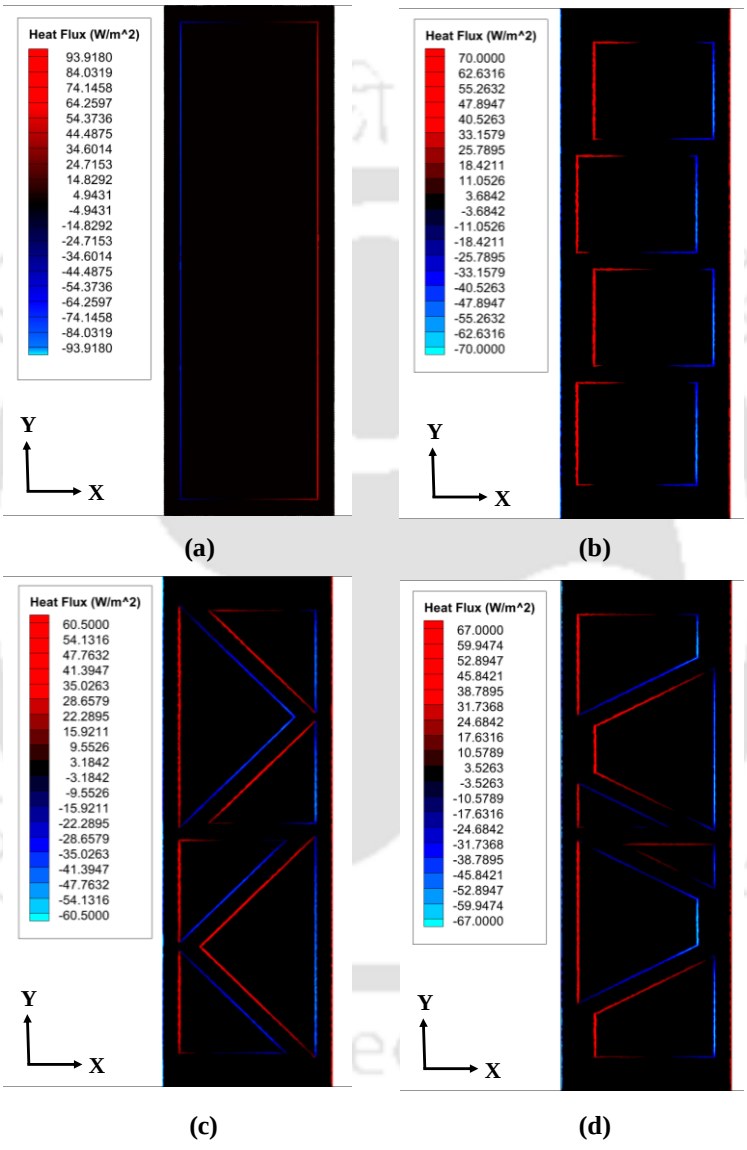

Figure 5.7 Heat flux distribution of (a) RH, (b) L, (c) T, and (d) LT configurations.

The Temperature contour lines generated from the temperature distribution graph is presented in **Figure 5.8**. For solid concrete in the lattice wall, constant temperature lines were observed perpendicular to the direction of heat flow which confirms that solid matrix is the domain of conductive heat flow in the walls and such vertical isotherms were observed only near to hot

and cold side of the wall. But as the isotherms run close to the cavities, the temperature isotherms exhibit sudden change in heat flow path indicating an alteration in the mode of heat transfer from conduction to convection and/or radiation. This bending of temperature lines was found exactly near to the boundary wall indicating maximum temperature variation occurs at the solid fluid interface. It is important to note that the temperature contours in the cavity of different configurations were horizontal, thus indicating constant temperature within the cavities and effect of such temperature gradient is further discussed using velocity and streamline maps.

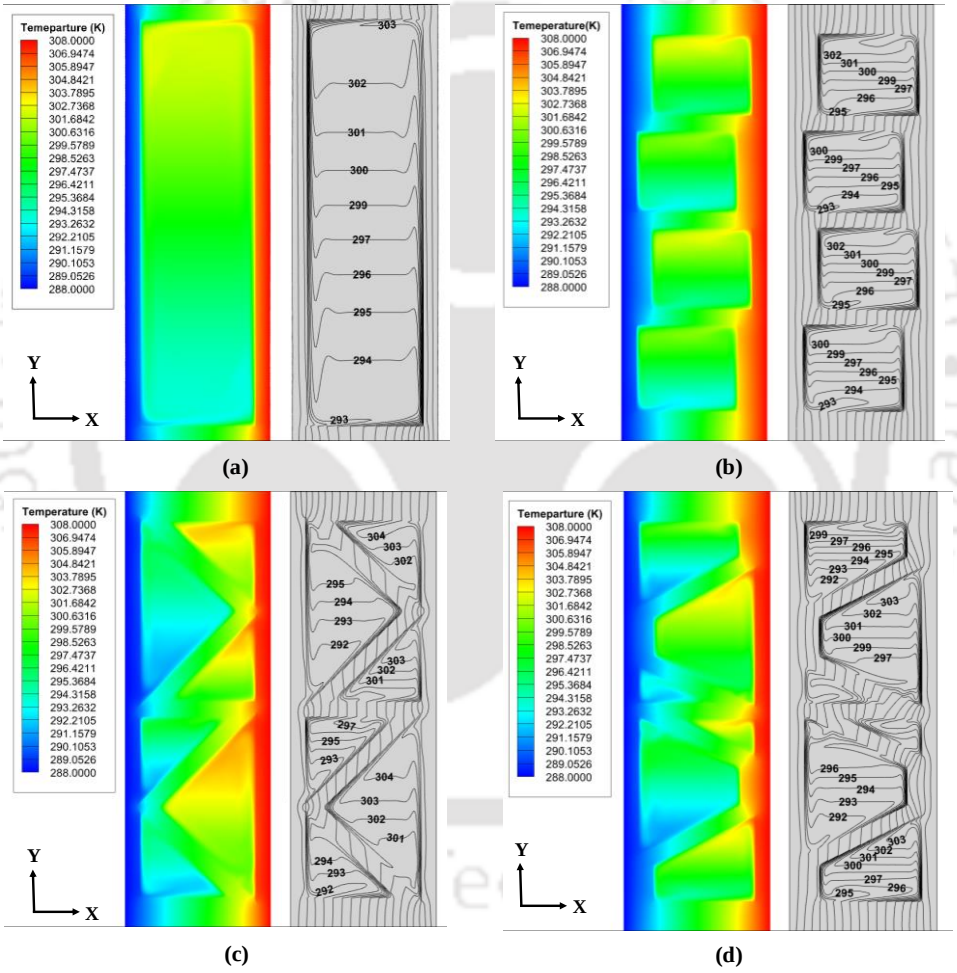

Figure 5.8 Temperature distribution and isotherms of (a) RH, (b) L, (c) T, and (d) LT configurations.

It is seen from **Figure 5.9** that convective heat transfer is primarily influenced by the cavity geometry and the flow is driven by the temperature gradient, resulting in peak velocities near the boundary. The streamlines within the cavity offer a compelling visualization of the flow dynamics, unveiling a distinctive path wherein air adjacent to the hot wall undergoes heating,

leading to expansion and reduced density. This lower-density air tends to rise up and gain velocity due to pressure difference between the hot and cold sides. This heated air eventually reaches the colder boundary region and starts to cool down (making it heavier), while creating a circulation pattern. Such circular pattern was particularly seen close to the outer boundary region, but as it moves towards the central region, the flow path changes and follows a straight line path, which indicate stagnant velocity of air at those positions [141]. This was further confirmed by the velocity map, which shows zero flow velocity in the central region.

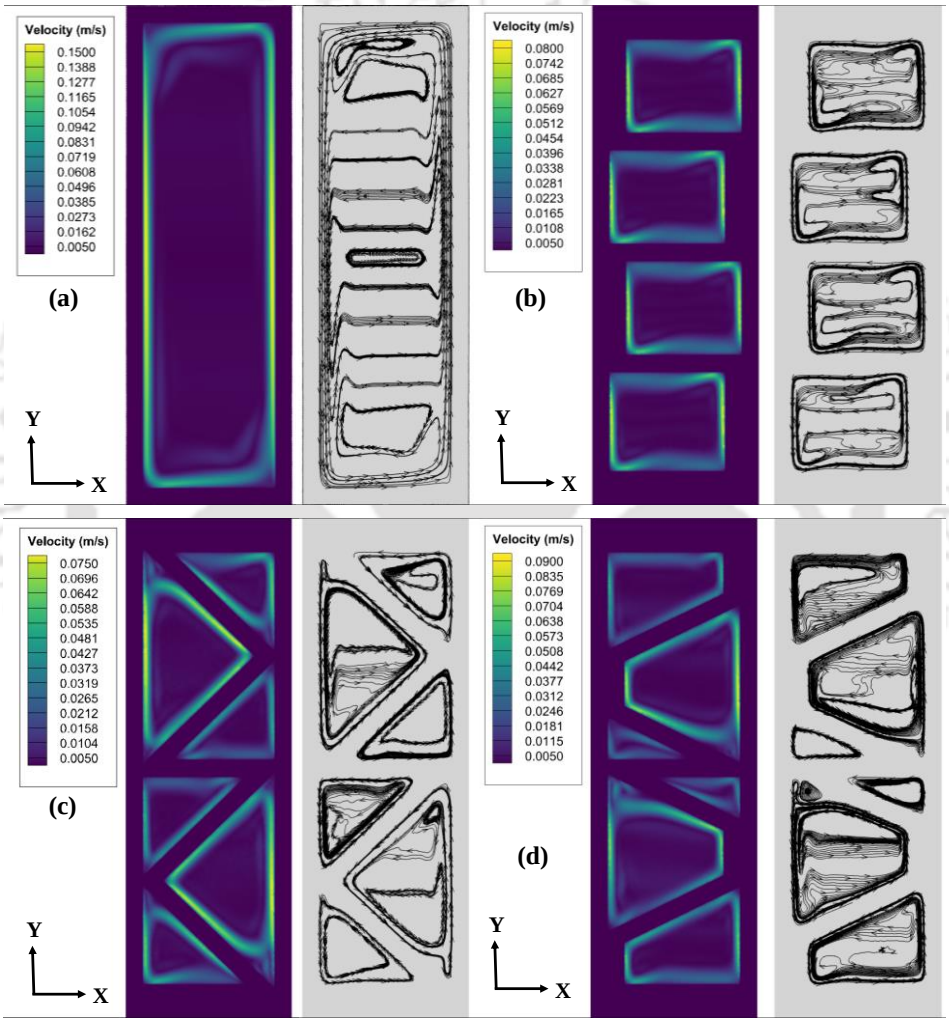

Figure 5.9 Velocity distribution and streamline map of (a) RH, (b) L, (c) T, and (d) LT configuration.

When comparing the peak velocity, the RH configuration has shown the highest air velocity (0.15 m/s), followed by LT (0.090 m/s), L (0.080 m/s), and T configuration (0.075 m/s). As the air flow inside the cavity is purely driven by the buoyancy, the velocity was found to be less and is not reliable (as it is not a function of heat transfer) for natural convection case. To analyse

intensity of convection inside the cavity, a dimensionless parameter i.e. Rayleigh number (Ra) (**equation 21**) is calculated using Grashof number (Gr) and Prandtl number (Pr) as expressed in **equation 22** and **23**.

$$Ra = (g\beta\Delta T\ L^3) / \nu\alpha, \quad (21)$$

$$Gr = (g\beta\Delta T\ L^3) / \nu^2, \quad (22)$$

$$Pr = {}^{\nu}/_{\alpha},\ L = {}^{A_c}/_{P} \quad (23)$$

Where g is the acceleration due to gravity, β is the volumetric thermal expansion coefficient, ΔT is the effective temperature difference calculated between the left and right vertical walls bounding the air layer, L is a characteristic length, A_c is cross sectional area, P is perimeter, ν is the kinematic viscosity, and α is the thermal diffusivity.

Table 5.5 Heat flux and Raleigh number of different wall configurations.

Configurations	Characteristics length (L_c)	Temperature difference(ΔT)	Raleigh Number (Ra)	Heat Flux (W/m^2)
RH	0.3733	10.0000	4.7086×10^7	93.9180
L	0.1879	7.0000	4.2019×10^6	70.0000
T	0.1667	5.0000	2.0947×10^6	60.5000
LT	0.1849	7.0000	4.0035×10^6	67.0000

The Ra number for RH (**Table 5.5**) configuration was in the order of 10^7, which indicates the heat flow in transitional regime. However, in case of L, T and LT configurations, the Ra value was in the order of 10^6 indicating under boundary layer flow regime, where natural convection dominates over conduction in specific cavities. This difference is primarily attributed to the size of different cavities. The Ra number calculations reveal that larger cavity lengths, such as those in the RH configuration, allow for substantial airflow development, which can be reconfigured via different lattice geometries. As Ra number was used as a quantitative gauge for heat transfer, it was also compared with heat flux data and found to be following the same trend (see **Table 5.5**). Among all lattice configurations, the Ra number was highest for the rectangular cavity (L configuration), followed by trapezoidal cavity (LT configuration) and triangular cavity (T configuration). Interestingly, despite identical temperature differentials for L and LT configurations, the Ra number was highest for L configuration, underscoring the

significant influence of cavity geometry on facilitating airflow development. The triangular cavity (T configuration) exhibited the lowest Ra number due to its smallest characteristic length and temperature gradient, resulting in weaker conduction and convection compared to the rectangular and trapezoidal cavities. In other words, while rectangular air cavities provide insulation, the horizontal lattice connection in the RH cavity facilitates heat transfer from hot to cold wall with minimal obstruction, thus leading to higher thermal bridging and highest heat flux. Conversely, the T configuration, with its triangular geometry and smaller cavity size, exhibited lower thermal bridging and heat flux values. The effect of distinct mode of heat transfer is analysed in the following section in order to optimise the lattice configuration suitable for high thermal resistance (or low U) value.

5.3.2 Effect of heat transfer modes

Figure 5.10 provides a comprehensive overview of the heat flux associated with different lattice configurations while considering conduction, convection, and radiation modes. It was found that when only radiation is ignored, a substantial reduction in heat flux (~ 40%) was observed followed by the case when convection is ignored along with radiation (~65%). This signifies that all heat transfer modes are intricately linked and thermal radiation is the most significant effect among all. The reason is attributed to the high emissivity of the concrete surfaces (0.90), which emit and absorb thermal radiation, thus enabling effective radiative heat exchange between walls within the cavity. Such results are in line with the previous study where researchers have suggested usages of low emissivity coating to reduce energy consumption in buildings [145–147].

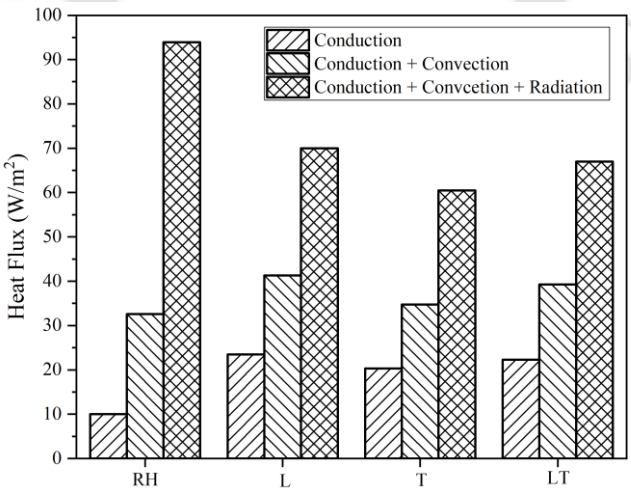

Figure 5.10 The effect of heat transfer modes on heat flux of different lattice walls.

Furthermore, the T configuration was considered to unveil the effect of heat transfer modes on temperature contours within the cavity. In case of pure conduction (i.e. when air inside the cavity is assumed to have constant density), the air does not experience any significant mixing or redistribution of heat. As a result, the temperature remained relatively uniform (without any significant temperature gradients) throughout the cavity, which led to horizontal temperature contours that run parallel to the heated and cooled surfaces in the lattice configurations (see **Figure 5.11**).Though the assumption of constant air density does not make much sense for analysis of physical lattice walls as studied in the past [104], this study indicates the repercussion of different modes of heat transfer for practical applications of lattice walls, where convection and radiation phenomena cannot be ignored.

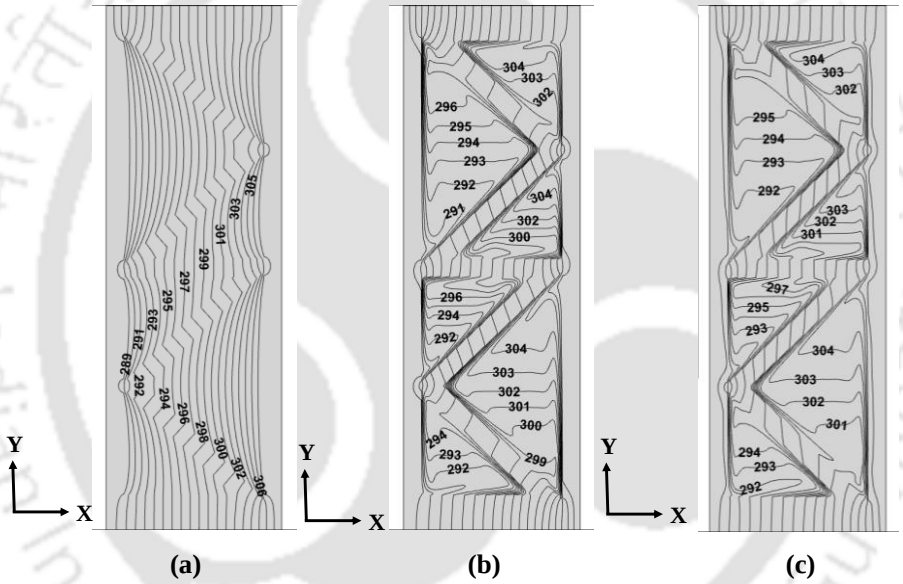

Figure 5.11 Isotherms of T configuration considering (a) conduction (b) conduction and convection, and (c) conduction, convection and radiation.

5.3.3 Modified RH configuration to reduce the heat transfer

The RH configuration has inherently large cavity and to reduce the U value, cavity heat transfer was decreased via the lattice configurations as it divides the larger rectangular area in to smaller cavities. However, while reducing cavity size, solid vertical connections were introduced that facilitate the heat transfer from hot to cold wall. The modified RH configurations are named as RH1 (where the rectangular cavity is divided with a single vertical partition) and RH2 configuration (with two identical vertical partitions). The detailed geometry of RH1 and RH2 configurations is shown in **Figure 5.12**.

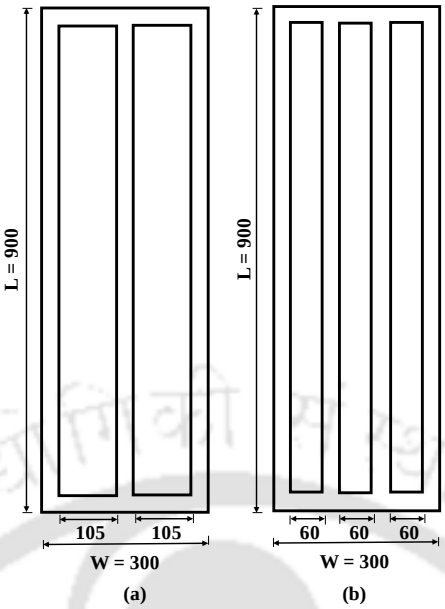

Figure 5.12 2D geometry of modified RH configurations (a) RH1, and (b) RH2 (all dimensions are in mm).

It is seen from **Figure 5.13** that the modification via addition of single vertical partition (i.e. RH1) resulted a drastic reduction (44% in U value) in the thermal transmittance and this impact was more pronounced (58% in U value) in case of two vertical partitions (RH2) with an excellent U value of 2.03 W/m^{2}K. It was also noticed that with similar cavity percentage (i.e. 57%), U value of the RH2 configuration is much lower (~37%) than the L, T and LT configurations. This signify that U value is not a direct function of the material/cavity, rather it depends on the nature of cavity and position of the partition wall which can influence the thermal resistance due to the interactions between conduction, convection and thermal radiation.

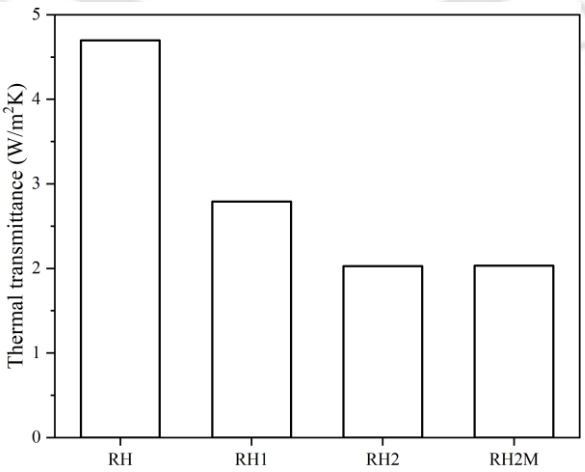

Figure 5.13 Thermal transmittance of the modified RH configurations.

In comparison to the RH wall, the addition of vertical partitions in RH2 resulted in a lengthier conductive path, which is shown by the vertical temperature lines near the partition boundary wall and bending of temperature lines inside the cavity (**Figure 5.14(a)**). This confirms higher lenience of the RH2 configuration towards the heat transfer by conduction mode. The addition of vertical partitions mainly divides the large cavity area into smaller cavities, thus confining air movement as shown in the velocity streamlines (**Figure 5.14(b)**). It is interesting to note that though the peak velocity increased up to 0.095 m/s, the convective heat transfer is reduced (Ra number was in the range of 10^5 compared to that of RH (10^7) and T (10^6) configuration) which is attributed to reduced characteristics length and temperature difference (4 K) of the air velocity inside individual rectangular cavities. Furthermore, these vertical partitions also act as a radiation shield Hence the improvement in thermal performance of RH2 configuration can be reckoned as a result of simultaneous inhibition of the three heat transfer modes.

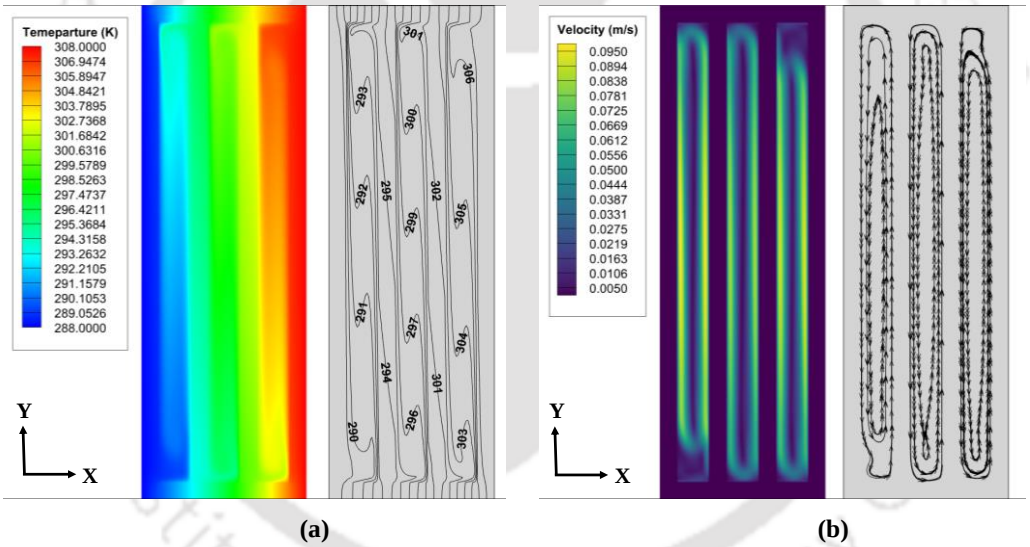

Figure 5.14 (a) Temperature distribution and isotherms, (b) Velocity distribution and streamline map of RH2 configuration.

Despite improvement in the thermal performance, further addition of vertical partitions is not possible due to the limitation of the wall width and width of a typical 3D printed layer. We therefore further modified the RH2 configuration and renamed as RH2 modified (RH2M), where the vertical connections are positioned closer to their respective hot and cold walls with maximum possible gaps (i.e. 30 mm) as depicted in **Fig. 5.15**. Due to similar cavity percentage as of earlier configurations, the U value of RH2M configuration was unchanged (Fig. **5.13)**.

The shifting of vertical partitions only redistributed the convection and radiation component in the confined side rectangular cavity and central rectangular cavity. It is observed in **Fig. 5.16** that the bending of temperature lines shifts towards horizontal near the side rectangular cavity and it became vertical near the central cavity region. This clearly indicate that, though the convection current is greatly reduced in the side rectangular cavity, this effect is counteracted with stable convection and radiation near the central region.

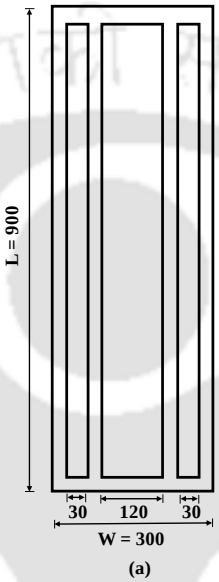

Figure 5.15 2D geometry of RH2 modified (RH2M) configuration (all dimensions are in mm).

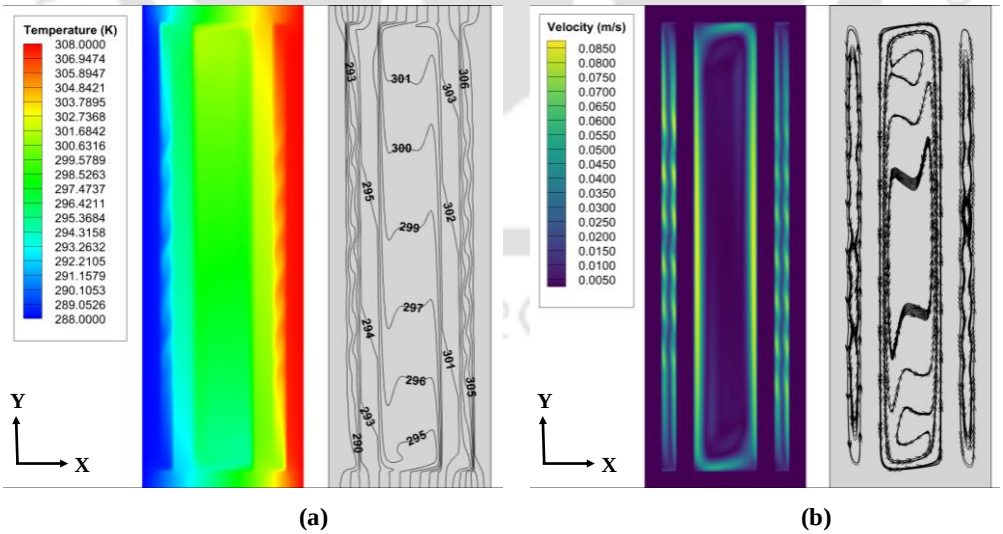

Figure 5.16 (a) Temperature distribution and isotherms, (b) Velocity distribution and streamline map of RH2M configuration.

5.3.4 Proposed composite lattice walls with hybrid configuration and insulation material

The abovementioned analysis indicates that further enhancement of thermal performance can be achieved by subdividing the central rectangular cavity of the RH2M configuration with vertical partitions. However, such vertical partition designs often lack the mechanical stiffness required for structural integrity [148]. Therefore, hybrid configuration is proposed in this study by filing the central rectangle cavity of RH2M with the T type configuration, which has the lowest U value among the three lattice configurations reported in section 3.1. This hybrid configuration is named as RT2 where the numeric 2 denotes the number of loop used in the T configuration. The effect of number of loops was studied via RT1 and RT3 configurations and their details are given in **Figure 5.17**.

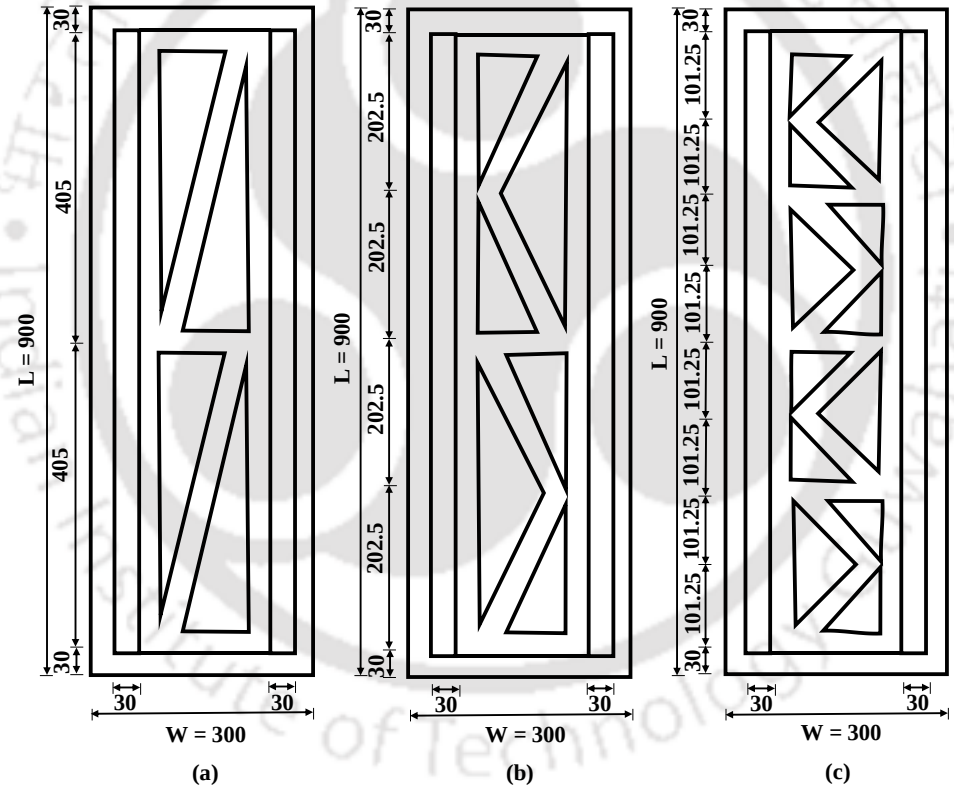

Figure 5.17 Geometry of hybrid configurations (a) RT1, (b) RT2, (c) RT3 (all dimensions are in mm).

The thermal transmittance of hybridized lattice walls was plotted in **Fig. 5.18**. It is observed that in case of RT2 design, the U value was found to be decreased from 2.03 to 1.73 W/m^{2}K. The reduction in the U value is primarily attributed to the division of the central rectangular cavity into smaller triangular cavities, which effectively diminishes the convection and radiation components of heat transfer. However, it is crucial to recognize that this cavity

division process inadvertently leads to an increase in footprint volume and reduces the cavity percentages (see **Table 5.6**), which increases the conductive component of heat transfer. To further investigate the specific effect of the cavity percentage and looping effect, RT2 is compared to that of RT1 and RT3 configurations. It is clear from **Table 5.6** that addition of more than two loops T configurations increases the U value (4%) whereas the presence of one loop T configuration reduces the final value by 1.15%. The reduction in the U value is primarily attributed to the division of the rectangular cavity into smaller triangular cavities, which effectively reduces the convection and radiation components of heat transfer. However, further division of area via RT3 configuration inadvertently leads to an increase in the footprint volume and reduces the cavity percentages (see **Table 5.6**) to 39%. This resulted increase in U value due to increase in the conductive component of heat transfer.

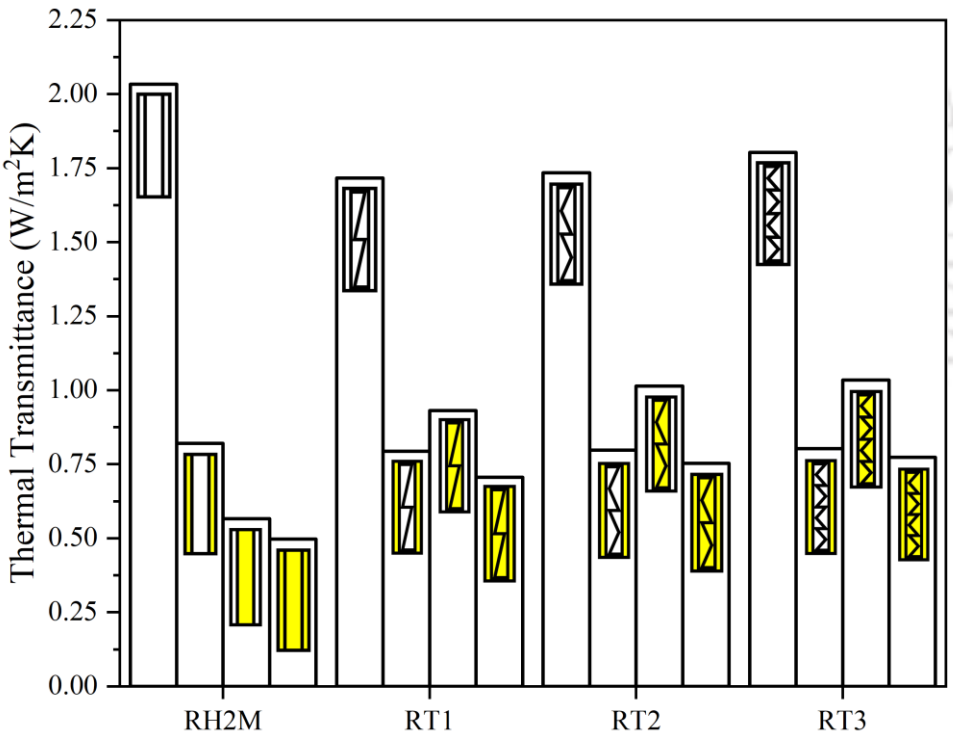

Figure 5.18 Thermal transmittance of RH2M and hybrid RT configurations with and without insulations (insulation is marked in YELLOW).

Given the recommendation of ECBC regulation [149], we have further studied the effect insulation material to lower the U value by filling it with (i) complete insulation (CI), (ii) insulation at side rectangular cavity (ISR), and (iii) insulation at central triangular/rectangular cavity (ICT/ICR). The results of numerical simulations of composite lattice wall in terms of U

value is plotted in **Figure 5.18**. It was found that in case of full insulation, the U value was lowest (0.50 W/m^{2}K) for RH2M configuration followed by RT1 (0.70 W/m^{2}K), RT2 (0.75 W/m^{2}K) and RT3 configuration (0.77 W/m^{2}K). In case of selective placement of insulation, it was observed that for RH2M configuration insulation at the central rectangular cavity reduced the U value to 0.56 W/m²K, whereas insulation at the side rectangular cavity increased the U value to 0.82 W/m²K. In contrast, for all three hybrid configurations (RT1, RT2 and RT3) presence of insulated side rectangular cavity gave lower U value in comparison to the insulated central triangular cavity. This discrepancy is primarily attributed to the nature of cavity that is being insulated for example in case of RH2M configurations, all the cavities are rectangular and the overall resistance increased with increase in extent of insulation. However, in case of hybrid configurations with both rectangular and triangular cavities, the thermal resistance values were considerably altered.

Table 5.6 Details of the RH2M configuration and hybrid RT configurations with and without insulations.

Name	Cavity Volume		Footprint Volume	Insulation Volume (m^3)	Cavity %	Insulation %	U value (W/m^{2}K)
	Rectangular cavity (m^3)	Triangular cavity (m^3)					
RH2M	0.1361	-	0.1069	-	56.0082	0.0000	2.0338
RH2M_ISR	0.0907	-	0.1069	0.0454	37.3251	18.6831	0.8204
RH2M_ICR	0.0454	-	0.1069	0.0907	18.6831	37.3251	0.5657
RH2M_CI	-	-	0.1069	0.1361	-	56.0082	0.4978
RT1	0.0454	0.0603	0.1373	-	43.4979	0.0000	1.7159
RT1_ISR	-	0.0603	0.1373	0.0454	24.8148	18.6831	0.7936
RT1_ICT	0.0454	-	0.1373	0.0603	18.6831	24.8148	0.9309
RT1_CI	-	-	0.1373	0.1057	-	43.4979	0.7059
RT2	0.0454	0.0590	0.1387	-	42.9630	0.0000	1.7339
RT2_ISR	-	0.0590	0.1387	0.0454	24.2798	18.6831	0.7973
RT2_ICT	0.0454	-	0.1387	0.0590	18.6831	24.2798	1.0145
RT2_CI	-	-	0.1387	0.1044	-	42.9630	0.7530
RT3	0.0454	0.0500	0.1477	-	39.2593	0.0000	1.8024
RT3_ISR	-	0.0500	0.1477	0.0454	20.5761	18.6831	0.8023
RT3_ICT	0.0454	-	0.1477	0.0500	18.6831	20.5761	1.0345
RT3_CI	-	-	0.1477	0.0954	-	39.2593	0.7735

It can be noted from **Figure 5.18** that in case of insulated side rectangular cavity, the U value was nearly constant at 0.79 W/m^{2}K irrespective of the configuration, while the U value of the composite wall slightly increased (from 0.93 to 1.03 W/m^{2}K) with increase in the number of loops. This indicate that the side rectangular cavities (when insulated) were able to provide higher resistance and inner triangular cavities have very less or no effect. However, when the central triangular cavities were filled with insulation, the angular struts act as thermal bridge and provides path for heat flow. As a result, the side rectangular cavities are found to have higher resistance at lower insulation percentage (18%) while the central triangular cavities needs comparatively more insulation (~22%). These findings highlight the complex interactions between geometric configurations and insulation distribution within the composite lattice wall.

5.4 Further discussions

5.4.1 Cost effectiveness analysis

The economic efficiency of the proposed 3DCP lattice wall configurations was evaluated using Cost Performance Index (CPI), based on the material and processing cost (see **Table 5.3**) incurred for each unit of thermal performance (U value) improvement. It is clear from **Figure 5.19** that while developing new lattice designs by adding more material into the RH2M configuration, the U-value reduced with minimal CPI value of 1747 to 1937 for RT1 and RT2 configurations, whereas for RT3 configuration the CPI value was increased to 3321 as both cost and U value increased. In contrast, with addition of insulation, the CPI was found to be minimum for insulation at side rectangular cavity (RH2M_ISR) over central triangular/rectangular cavity or even complete insulation. This suggests critical insulation material position inside the lattice configuration to attain a cost optimal solution. It is important to highlight that though the RH2M_ISR configuration has lowest CPI value, proposed hybrid configuration (RT2_ISR) has been identified as most efficient, as it provides better structural (higher mechanical linkages) and thermal requirements (lower U value) with minimal increase in CPI value.

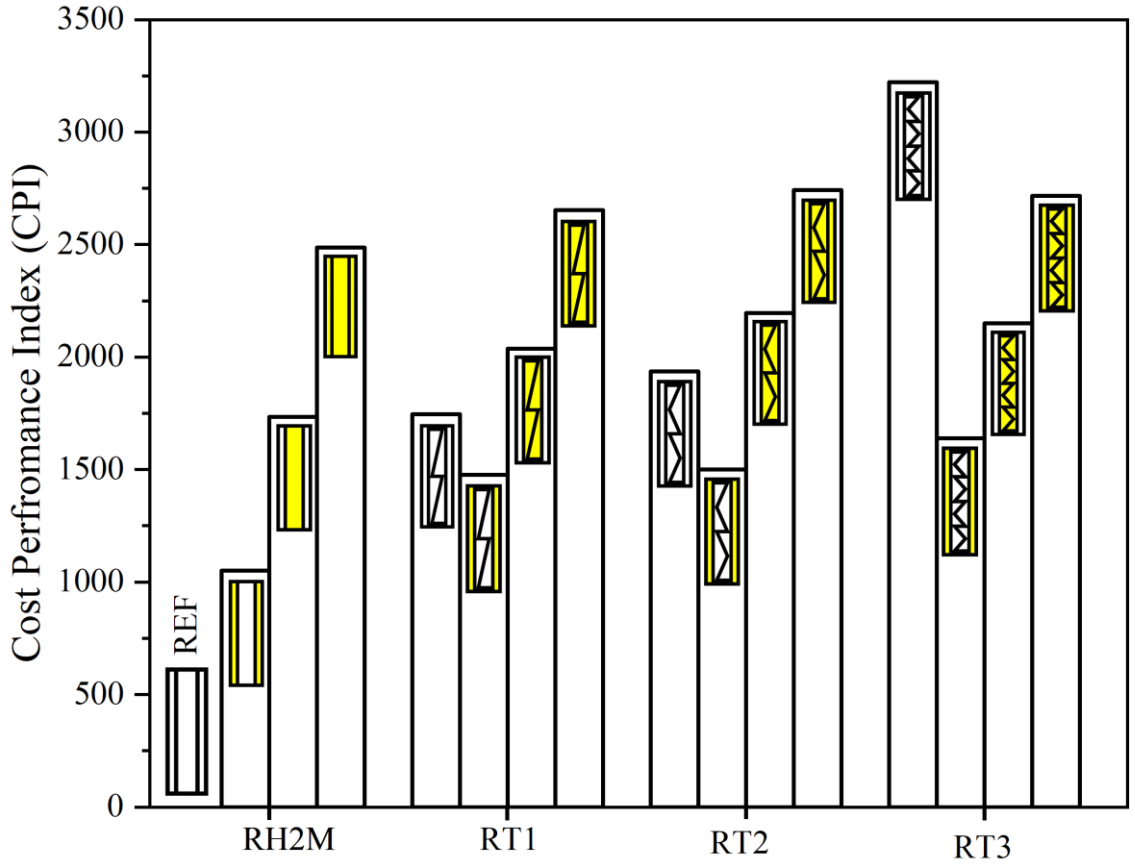

Figure 5.19 Cost Performance Index (CPI) of proposed lattice configuration (insulation is marked in YELLOW and RH2M configuration without insulation was taken as REF).

5.4.2 Effect of concrete thermal conductivity

Here, the effect of material thermal conductivity is investigated for RT2_ISR wall configuration to attain a target U value (i.e. 0.4 W/m^{2}K) as per the ECBC building code. The design and addition of insulation resulted in reduction of both convection and radiation components of RT2_ISR wall from ~ 45 – 65 % to ~ 3 – 8 % range respectively (**Fig. 5.20 (a)**). Since further reduction will lead to decrease the cavity percentage below 20%, an attempt has been made to reduce the conductive heat flux by using low thermal conductive material. In this regard, numerical simulation was performed with thermal conductivity (K) value ranging from 1.61 to 0.41 W/mK and the results (**Fig. 5.20 (b))** indicate possibility of attaining the target U value for K equal to 0.41 W/mK. However, printability, structural properties of such material with modified thermo-physical properties need further investigation and beyond the scope of this study.

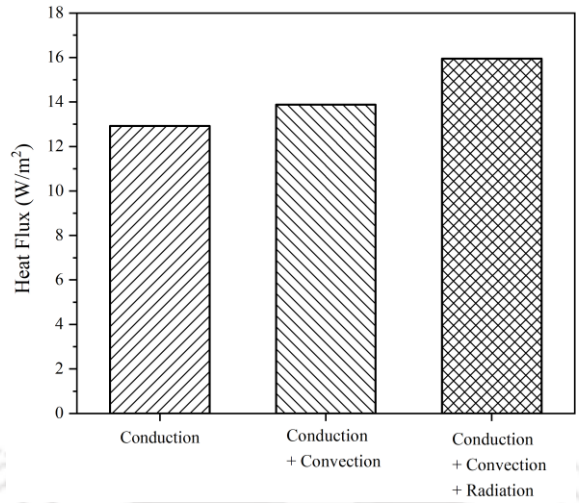

(a)

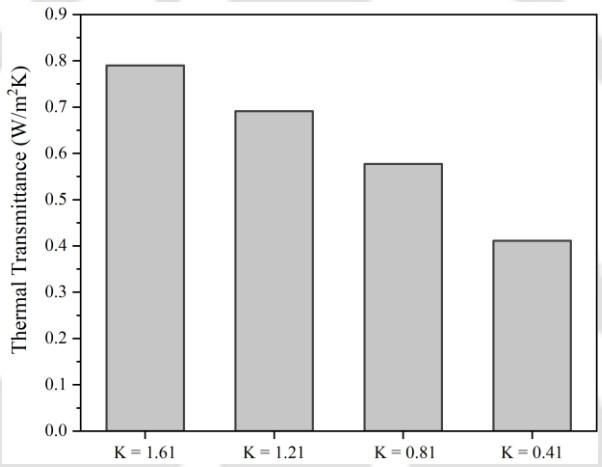

(b)

Figure 5.20 (a) Thermal properties of RT2_ISR configuration wall: (a) Heat flux (b) thermal transmittance as a function of material thermal conductivity.

5.5 Summary

This study provides significant insights into the thermal behaviour of 3D printed lattice wall envelopes by seamlessly combining CFD models and industrial-scale experimental data. Initially, extrusion-based 3D-printed lattice walls with four distinct configurations (rectangular hollow, L, T, and LT) were numerically analyzed under steady-state conditions. The findings reveal that lattice configurations and parent concrete properties significantly influence heat flow and thermal performance, with all studied configurations exhibiting higher U-values that exceed ECBC limits due to substantial convection and radiation within large cavities. Later, CFD guided new composite lattice wall configurations were introduced using hybrid lattice

pattern and insulation material. The complete filling of insulation material (42%) resulted lower U value as expected nevertheless key findings highlight the significant influence of appropriate cavity selection, as selective filling of insulation material (18%) resulted comparable thermal performance with U value reaching as low as 0.79 W/m^2K in composite lattice walls. The study further emphasizes the importance of incorporating low thermal conductive 3D printable materials, such as PS mix, to enhance the energy efficiency of printed structures. These findings underscore the potential of lightweight; high-strength lattice walls as energy-efficient building envelopes for sustainable construction.

CHAPTER 6

Conclusion and future scope

This chapter outlines the key conclusions and significant findings of the study, along with suggestions for future research directions.

6.1 Influence of Portland slag cement and slag sand on sustainability and performance of 3D printable mortar

In this study, a comprehensive investigation was undertaken to systematically examine the influence of (i) substitution of river sand with slag sand (ii) substitution of OPC with slag cement, and (iii) combined effect of both slag sand and cement to enhance the sustainability and 3D printability of the mixes along with mechanical, thermal properties, and carbon sequestration capability. Based on the results and discussion, following conclusions can be drawn:

- The combination of PSC and SS exhibited remarkable buildability, achieving up to 88 printed layers compared to the early collapse at 30 layers for the control mix. However, this enhancement was accompanied by a reduced open time of 20 minutes compared to 40 minutes, indicating a trade-off between early-age performance and workability.
- The enhanced buildability and early-age stability observed in this study can be attributed to the angular morphology of SS, which improved inter-particle friction and shear resistance, coupled with the finer particle size and higher reactivity of PSC.
- In terms of hardened state properties, while the control mix achieved the highest longitudinal compressive strength (60 MPa), slag-based mixes (OS, PR, PS) demonstrated more uniform strength across orientations, reducing anisotropy.
- Furthermore, control mix exhibited the highest conductivity at 1.52 W/mK, while the OS and PS mixes showed notably lower values (~0.87 W/mK). This reduction can be attributed to the lower crystallinity and increased microstructural defects in SS, which affect heat transfer properties.
- The pore microstructure reveals that although the control mix has the lowest total porosity (13.18%), it contains largely open pore structure macro pores (16%) and large capillary pores (61%). In contrast, slag-based mixes exhibit slightly higher porosity but with increased gel and small capillary pores, enhancing matrix densification. This shift highlights the role of PSC and SS in optimizing pore size distribution for improved sorption behavior.
- Early age carbonation analysis reveals that PSC mixes (PR: 9.67%, PS: 8.45%) exhibit higher CO_2 sequestration compared to OPC mixes (OR: 5.61%, OS: 4.80%), primarily due to the decalcification of ettringite, C-S-H, and other hydration products in the early

temperature range.

- Although SS exhibits a lower carbon footprint (eCO_2 value: 0.0045) compared to river sand (eCO_2 value: 0.0051), its higher transportation cost affects economic sustainability. Nonetheless, mixes incorporating slag sand and PSC achieved the lowest global warming potential (327 kg/m^3) and the highest multi-criteria efficiency index (11.65), showcasing an optimal balance of environmental impact, economic feasibility, and material performance, making them highly suitable for sustainable 3D printing applications.

6.2 Flexural performance of 3D printed concrete structure with lattice infill configurations

This study firstly examined the effect of infill patterns on the flexural strength of 3D printed lattice beams in two loading directions. The effect of different infill patterns on peak load, maximum mid-point displacement, stiffness and flexural deformation resistance capacity was experientially investigated. Multi-scale models considering material anisotropy were employed to simulate the mechanical behavior of fiber-reinforced cementitious mortar. A parametric investigation was also conducted to understand the influence of infill patterns based on the topology optimization scheme. The key findings from this work are listed below:

- In case of transverse loading condition, the TBeam outperforms LBeam with a notable increase in the peak load (+377%) and maximum mid-point displacement (+61%) exhibiting substantial increase (by approximately 500%) in the flexural deformation resistance capacity. However, under vertical loading direction, the LBeam demonstrated higher flexural deformation resistance capacity (+17.7%) despite its lower peak load and maximum mid-point displacement compared to the TBeam.
- Based on simulated results, the bending load necessary to cause fracture in the 3D-printed lattice beams was relatively consistent with a variance of 2.04 kN², when it is subjected to vertical load path. In contrast, for transverse loading, a substantial variation in the peak load was observed with variance up to 86.65 kN². Therefore, transverse loading was selected for further optimization with respect to the best-performing TBeam configuration.
- Designing lightweight 3D-printed concrete beams with infilled printing patterns based on topology optimization led to a better bending performance (+60% higher peak load,

+12% maximum midpoint displacement). The optimal design of infill patterns was obtained when the horizontal infill length was equal to quarter (25%) of the width of triangular infills.

It is thus ascertained from this study that the infill printing pathways and direction of loading significantly affect mechanical performance of the lattice beams. The enhanced flexural capability of optimized infill design makes the lightweight beam as potential candidates for building and construction applications.

6.3 Thermal performance of 3D printed concrete wall with lattice infill configurations

This study provides significant insights into the thermal behaviour of 3D printed lattice wall envelopes by seamlessly combining CFD models and experimental data. CFD model was proposed to understand the exact heat transfer mechanism through velocity and temperature distribution plots. Based on the results and discussion, the following key conclusions can be drawn:

- Typical rectangular hollow configurations and lattice configuration exhibit thermal inefficiency with U values surpassing the required regulations due to substantial convection and radiation within large cavities. This highlights the pressing need for effective mitigation strategies.
- By comprehending heat flow directions through simulations and embracing hybridization concepts, a novel vertical partition-based lattice configuration has been proposed. This innovative approach significantly reduces the U value to 1.73 W/m^2K by strategically positioning infill patterns to create smaller cavities with greater solid resistance against heat flow.
- To achieve the U value near to the required regulation, filling of insulation material was found justified. However, in case of hybridized configuration, simulation-based selection of appropriate cavity location was seen more beneficial as it provides comparable performance (0.79 W/m^2K) at lesser insulation extent (18%).

6.4 Future scope and recommendations

The findings and limitations of this research provide a foundation for future studies aimed at advancing 3DCP. The following points outline the critical areas for future investigation:

- **Enhancing workability for extended prints:** While high-thixotropy mixes like those with PSC offer superior buildability, they significantly reduce open time, affecting continuity during large-scale printing. Future research should explore mix design optimizations—such as increasing the sand-to-binder ratio, adjusting superplasticizer dosage, or incorporating suitable set retarders and fluidity-retaining superplasticizers to—prolong open time. Additionally, operational strategies like intermittent mixing or real-time rheology control could be studied to support uninterrupted printing over extended durations.
- **Long-term durability assessment:** Long-term performance of the developed mixes is crucial and thus, future work should focus on evaluating the durability of the proposed sustainable mixes, particularly under harsh environmental conditions. Key areas for investigation may include strength at later ages (45, 90, and 180 days), freeze-thaw resistance, chloride ingress, and sulfate attack.
- **Multiscale and predictive modeling:** Literature features a limited number of numerical studies capable of predicting mechanical behavior of the 3DCP structures. Future numerical studies should account for air voids present within the printed filament, which significantly impact mechanical as well as thermal properties. The use of stochastic or probabilistic modeling techniques to simulate the distribution and effects of air voids will help improve the accuracy of numerical predictions. Additionally, incorporating cohesive interlayer models will enhance the understanding of mechanical interactions between printed layers, leading to more accurate predictions of structural performance.
- **Development of functionally graded and adaptive lattice designs:** Building on the insights from this thesis, future work can focus on designing functionally graded or hybrid lattice infills with spatial variation in geometry and density to optimize performance.
- **Thermal and energy efficiency in 3D printed buildings:** As 3D-printed walls are already being used to build the complete buildings, it is crucial to conduct comprehensive life cycle assessments and energy simulations of full-scale 3D printed structures by leveraging strategic wall geometries, which can significantly reduce material use and energy consumption in the buildings. This will contribute to the development of energy-efficient and environmentally sustainable building designs.

References:

1. Tay YWD, Panda B, Paul SC, Noor Mohamed NA, Tan MJ, Leong KF. 3D printing trends in building and construction industry: a review. Virtual Phys Prototyp. 2017;12(3):261–76.

2. Panda B, Paul SC, Hui LJ, Tay YWD, Tan MJ. Additive manufacturing of geopolymer for sustainable built environment. J Clean Prod. 2017 Nov 20;167:281–8.

3. Zhuang Z, Xu F, Ye J, Hu N, Jiang L, Weng Y. A comprehensive review of sustainable materials and toolpath optimization in 3D concrete printing. Npj Mater Sustain. 2024 Jun 3;2(1):1–14.

4. Singh G, Das S, Ahmed AA, Saha S, Karmakar S. Study of Granulated Blast Furnace Slag as Fine Aggregates in Concrete for Sustainable Infrastructure. Procedia - Soc Behav Sci. 2015 Jul 3;195:2272–9.

5. Hossain MA, Zhumabekova A, Paul SC, Kim JR. A Review of 3D Printing in Construction and its Impact on the Labor Market. Sustainability. 2020 Jan;12(20):8492.

6. Buswell RA, da Silva WRL, Bos FP, Schipper HR, Lowke D, Hack N, Kloft H, Mechtcherine V, Wangler T, Roussel N. A process classification framework for defining and describing Digital Fabrication with Concrete. Cem Concr Res. 2020 Aug 1;134:106068.

7. Guamán-Rivera R, Martínez-Rocamora A, García-Alvarado R, Muñoz-Sanguinetti C, González-Böhme LF, Auat-Cheein F. Recent Developments and Challenges of 3D-Printed Construction: A Review of Research Fronts. Buildings. 2022 Feb;12(2):229.

8. Bos F, Wolfs R, Ahmed Z, Salet T. Additive manufacturing of concrete in construction: potentials and challenges of 3D concrete printing. Virtual Phys Prototyp. 2016 Jul 2;11(3):209–25.

9. Boddepalli U, Panda B, Ranjani Gandhi IS. Rheology and printability of Portland cement based materials: a review. J Sustain Cem-Based Mater. 2023 Jul 3;12(7):789–807.

10. Ma G, Wang L. A critical review of preparation design and workability measurement of concrete material for largescale 3D printing. Front Struct Civ Eng. 2018 Sep 1;12(3):382–400.

11. Chen Y, He S, Gan Y, Çopuroğlu O, Veer F, Schlangen E. A review of printing strategies, sustainable cementitious materials and characterization methods in the context of extrusion-based 3D concrete printing. J Build Eng. 2022 Jan 1;45:103599.

12. Saruhan V, Keskinateş M, Felekoğlu B. A comprehensive review on fresh state rheological properties of extrusion mortars designed for 3D printing applications. Constr Build Mater. 2022 Jun 27;337:127629.

13. Paritala S, Singaram KK, Bathina I, Khan MA, Jyosyula SKR. Rheology and pumpability of mix suitable for extrusion-based concrete 3D printing – A review. Constr Build Mater. 2023 Oct 26;402:132962.

14. Prem PR, Ambily PS, Kumar S, Giridhar G, Jiao D. Structural build-up model for three-dimensional concrete printing based on kinetics theory. Front Struct Civ Eng. 2024 Jul 1;18(7):998–1014.

15. Nodehi M, Ozbakkaloglu T, Gholampour A. Effect of supplementary cementitious materials on properties of 3D printed conventional and alkali-activated concrete: A review. Autom Constr. 2022 Jun 1;138:104215.

16. Shishkin A, Abramovskis V, Zalite I, Singh AK, Mezinskis G, Popov V, Ozolins J. Physical, Thermal, and Chemical Properties of Fly Ash Cenospheres Obtained from Different Sources. Materials. 2023 Jan;16(5):2035.

17. Siddique R, Chahal N. Use of silicon and ferrosilicon industry by-products (silica fume) in cement paste and mortar. Resour Conserv Recycl. 2011 Jun 1;55(8):739–44.

18. Liu Y, Su Y, Xu G, Chen Y, You G. Research Progress on Controlled Low-Strength Materials: Metallurgical Waste Slag as Cementitious Materials. Materials. 2022 Jan 19;15(3):727.

19. Zhang H, Zhang C, He B, Yi S, Tang L. Recycling fine powder collected from construction and demolition wastes as partial alternatives to cement: A comprehensive analysis on effects, mechanism, cost and CO2 emission. J Build Eng. 2023 Jul 15;71:106507.

20. Chen L, Yang M, Chen Z, Xie Z, Huang L, Osman AI, Farghali M, Sandanayake M, Liu E, Ahn YH, Al-Muhtaseb AH, Rooney DW, Yap PS. Conversion of waste into sustainable construction materials: A review of recent developments and prospects. Mater Today Sustain. 2024 Sep 1;27:100930.

21. Snellings R, Mertens G, Elsen J. Supplementary Cementitious Materials. Rev Mineral Geochem. 2012 Jan 1;74(1):211–78.

22. Devi G, Balushi D, Ahmed S, Almawali S. Synthesis and Application of Nano and Micro-silica particles to enhance the Mechanical Proprieties of Cement Concrete. Concr Res Lett. 2016 Dec 10;

23. Fan X, Zhang M. Experimental study on flexural behaviour of inorganic polymer concrete beams reinforced with basalt rebar. Compos Part B Eng. 2016 May 15;93:174–83.

24. Hou S, Xiao J, Duan Z, Ma G. Fresh properties of 3D printed mortar with recycled powder. Constr Build Mater. 2021 Nov 22;309:125186.

25. Ulsen C, Kahn H, Hawlitschek G, Masini EA, Angulo SC, John VM. Production of recycled sand from construction and demolition waste. Constr Build Mater. 2013 Mar 1;40:1168–73.

26. Rashid K, Hameed R, Ahmad HA, Razzaq A, Ahmad M, Mahmood A. Analytical framework for value added utilization of glass waste in concrete: Mechanical and environmental performance. Waste Manag. 2018 Sep 1;79:312–23.

27. Alyousef R, Ahmad W, Ahmad A, Aslam F, Joyklad P, Alabduljabbar H. Potential use of recycled plastic and rubber aggregate in cementitious materials for sustainable construction: A review. J Clean Prod. 2021 Dec 20;329:129736.

28. Adiguzel D, Tuylu S, Eker H. Utilization of tailings in concrete products: A review. Constr Build Mater. 2022 Dec 19;360:129574.

29. Panda B, Ruan S, Unluer C, Tan MJ. Improving the 3D printability of high volume fly ash mixtures via the use of nano attapulgite clay. Compos Part B Eng. 2019 May 15;165:75–83.

30. Wang X, Khalil A, Celik K. Three-Dimensional Printability of White Portland Cement Containing Cenospheres. Mater J. 2021 Nov 1;118(6):147–54.

31. Panda B, Tan MJ. Rheological behavior of high volume fly ash mixtures containing micro silica for digital construction application. Mater Lett. 2019 Feb 15;237:348–51.

32. Kazemian A, Yuan X, Cochran E, Khoshnevis B. Cementitious materials for construction-scale 3D printing: Laboratory testing of fresh printing mixture. Constr Build Mater. 2017 Aug 1;145:639–47.

33. Zhang Y, Zhang Y, Liu G, Yang Y, Wu M, Pang B. Fresh properties of a novel 3D printing concrete ink. Constr Build Mater. 2018 Jun 20;174:263–71.

34. Rubio M, Sonebi M, Amziane S. Fresh and rheological properties of 3D printing bio-cementbased materials. Acad J Civ Eng. 2017 Jun 21;35(2):283–90.

35. Soltan DG, Li VC. A self-reinforced cementitious composite for building-scale 3D printing. Cem Concr Compos. 2018 Jul 1;90:1–13.

36. Weng Y, Lu B, Li M, Liu Z, Tan MJ, Qian S. Empirical models to predict rheological properties of fiber reinforced cementitious composites for 3D printing. Constr Build Mater. 2018 Nov 20;189:676–85.

37. Le TT, Austin SA, Lim S, Buswell RA, Gibb AGF, Thorpe T. Mix design and fresh properties for high-performance printing concrete. Mater Struct. 2012 Aug 1;45(8):1221–32.

38. Le TT, Austin SA, Lim S, Buswell RA, Law R, Gibb AGF, Thorpe T. Hardened properties of high-performance printing concrete. Cem Concr Res. 2012 Mar 1;42(3):558–66.

39. Lim S, Buswell RA, Valentine PJ, Piker D, Austin SA, De Kestelier X. Modelling curved-layered printing paths for fabricating large-scale construction components. Addit Manuf. 2016 Oct 1;12:216–30.

40. Nerella VN, Mechtcherine V. Chapter 16 - Studying the Printability of Fresh Concrete for Formwork-Free Concrete Onsite 3D Printing Technology (CONPrint3D). In: Sanjayan JG, Nazari A, Nematollahi B, editors. 3D Concrete Printing Technology [Internet]. Butterworth-Heinemann; 2019 [cited 2025 Jan 19]. p. 333–47. Available from: https://www.sciencedirect.com/science/article/pii/B9780128154816000166

41. Tay YWD, Panda B, Paul SC, Tan MJ, Qian SZ, Leong KF, Chua CK. Processing and Properties of Construction Materials for 3D Printing. Mater Sci Forum. 2016;861:177–81.

42. Rahul AV, Santhanam M, Meena H, Ghani Z. 3D printable concrete: Mixture design and test methods. Cem Concr Compos. 2019 Mar 1;97:13–23.

43. Kruger J, Zeranka S, van Zijl G. A rheology-based quasi-static shape retention model for digitally fabricated concrete. Constr Build Mater. 2020 Sep 10;254:119241.

44. Chaves Figueiredo S, Romero Rodríguez C, Ahmed ZY, Bos DH, Xu Y, Salet TM, Çopuroğlu O, Schlangen E, Bos FP. An approach to develop printable strain hardening cementitious composites. Mater Des. 2019 May 5;169:107651.

45. Chaves Figueiredo S, Romero Rodríguez C, Y. Ahmed Z, Bos DH, Xu Y, Salet TM, Çopuroğlu O, Schlangen E, Bos FP. Mechanical Behavior of Printed Strain Hardening Cementitious Composites. Materials. 2020 Jan;13(10):2253.

46. Mohan MK, Rahul AV, Van Tittelboom K, De Schutter G. Rheological and pumping behaviour of 3D printable cementitious materials with varying aggregate content. Cem Concr Res. 2021 Jan 1;139:106258.

47. Pham L, Tran P, Sanjayan J. Steel fibres reinforced 3D printed concrete: Influence of fibre sizes on mechanical performance. Constr Build Mater. 2020 Jul 30;250:118785.

48. Rahul AV, Sharma A, Santhanam M. A desorptivity-based approach for the assessment of phase separation during extrusion of cementitious materials. Cem Concr Compos. 2020 Apr 1;108:103546.

49. Panda B, Tan MJ. Material properties of 3D printable high-volume slag cement. In Swinburne University of Technology, Melbourne, Australia; 2018.

50. Dai S, Zhu H, Zhai M, Wu Q, Yin Z, Qian H, Hua S. Stability of steel slag as fine aggregate and its application in 3D printing materials. Constr Build Mater. 2021 Sep 13;299:123938.

51. Nekkanti H. Influence of Selected Supplementary Cementitious Materials on Properties of 3D Printable Cementitious Mixture for Application in Additive Manufacturing. Diss [Internet]. 2020 May 1; Available from: https://open.clemson.edu/all_dissertations/2629

52. Ma G, Sun J, Wang L, Aslani F, Liu M. Electromagnetic and microwave absorbing properties of cementitious composite for 3D printing containing waste copper solids. Cem Concr Compos. 2018 Nov 1;94:215–25.

53. Sun J, Huang Y, Aslani F, Ma G. Electromagnetic wave absorbing performance of 3D printed wave-shape copper solid cementitious element. Cem Concr Compos. 2020 Nov 1;114:103789.

54. Sun J, Huang Y, Aslani F, Ma G. Properties of a double-layer EMW-absorbing structure containing a graded nano-sized absorbent combing extruded and sprayed 3D printing. Constr Build Mater. 2020 Nov 20;261:120031.

55. Sun J, Huang Y, Aslani F, Wang X, Ma G. Mechanical enhancement for EMW-absorbing cementitious material using 3D concrete printing. J Build Eng. 2021 Sep 1;41:102763.

56. Duan Z, Hou S, Xiao J, Singh A. Rheological properties of mortar containing recycled powders from construction and demolition wastes. Constr Build Mater. 2020 Mar 20;237:117622.

57. Qian H, Hua S, Yue H, Feng G, Qian L, Jiang W, zhang L. Utilization of recycled construction powder in 3D concrete printable materials through particle packing optimization. J Build Eng. 2022 Dec 1;61:105236.

58. Hou S, Duan Z, Ye T, Zou S, Xiao J. Mechanical properties and pore structure of 3D printed mortar with recycled powder. Constr Build Mater. 2023 Aug 29;394:132068.

59. Ding T, Xiao J, Qin F, Duan Z. Mechanical behavior of 3D printed mortar with recycled sand at early ages. Constr Build Mater. 2020 Jul 10;248:118654.

60. De Vlieger J, Boehme L, Blaakmeer J, Li J. Buildability assessment of mortar with fine recycled aggregates for 3D printing. Constr Build Mater. 2023 Feb 27;367:130313.

61. Zou S, Xiao J, Ding T, Duan Z, Zhang Q. Printability and advantages of 3D printing mortar with 100% recycled sand. Constr Build Mater. 2021 Mar 1;273:121699.

62. Zou S, Xiao J, Duan Z, Ding T, Hou S. On rheology of mortar with recycled fine aggregate for 3D printing. Constr Build Mater. 2021 Dec 13;311:125312.

63. Bai M, Wu Y, Xiao J, Ding T, Yu K. Workability and hardened properties of 3D printed engineered cementitious composites incorporating recycled sand and PE fibers. J Build Eng. 2023 Jul 15;71:106477.

64. Ding T, Xiao J, Zou S, Wang Y. Hardened properties of layered 3D printed concrete with recycled sand. Cem Concr Compos. 2020 Oct 1;113:103724.

65. Zhou Y, Luo H, Anand K, Singh A, Xie YM. Sustainable use of ultrafine recycled glass in additive manufactured (3D printed) reactive powder concrete. Constr Build Mater. 2024 Mar 15;419:135556.

66. Andrew Ting GH, Noel Quah TK, Lim JH, Daniel Tay YW, Tan MJ. Extrudable region parametrical study of 3D printable concrete using recycled glass concrete. J Build Eng. 2022 Jun 1;50:104091.

67. Ting GHA, Tay YWD, Qian Y, Tan MJ. Utilization of recycled glass for 3D concrete printing: rheological and mechanical properties. J Mater Cycles Waste Manag. 2019 Jul 1;21(4):994–1003.

68. Ting GHA, Tay YWD, Tan MJ. Experimental measurement on the effects of recycled glass cullets as aggregates for construction 3D printing. J Clean Prod. 2021 Jun 1;300:126919.

69. Tan KH, Du H. Use of waste glass as sand in mortar: Part I – Fresh, mechanical and durability properties. Cem Concr Compos. 2013 Jan 1;35(1):109–17.

70. de Castro S, de Brito J. Evaluation of the durability of concrete made with crushed glass aggregates. J Clean Prod. 2013 Feb 1;41:7–14.

71. Cuevas K, Chougan M, Martin F, Ghaffar SH, Stephan D, Sikora P. 3D printable lightweight cementitious composites with incorporated waste glass aggregates and expanded microspheres–Rheological, thermal and mechanical properties. J Build Eng. 2021;44:102718.

72. Skibicki S, Pułtorak M, Kaszyńska M, Hoffmann M, Ekiert E, Sibera D. The effect of using recycled PET aggregates on mechanical and durability properties of 3D printed mortar. Constr Build Mater. 2022 Jun 13;335:127443.

73. Daniel Oosthuizen J, John Babafemi A, Shaun Walls R. 3D-printed recycled plastic eco-aggregate (Resin8) concrete. Constr Build Mater. 2023 Dec 8;408:133712.

74. Sambucci M, Marini D, Sibai A, Valente M. Preliminary Mechanical Analysis of Rubber-Cement Composites Suitable for Additive Process Construction. J Compos Sci. 2020 Sep;4(3):120.

75. Rubber-Cement Composites for Additive Manufacturing: Physical, Mechanical and Thermo-Acoustic Characterization | SpringerLink [Internet]. [cited 2024 Aug 11]. Available from: https://link.springer.com/chapter/10.1007/978-3-030-49916-7_12

76. Sovetova M, Kaiser Calautit J. Thermal and energy efficiency in 3D-printed buildings: Review of geometric design, materials and printing processes. Energy Build. 2024 Nov 15;323:114731.

77. Ma G, Li Z, Wang L. Printable properties of cementitious material containing copper tailings for extrusion based 3D printing. Constr Build Mater. 2018;162:613–27.

78. Li X, Zhang N, Yuan J, Wang X, Zhang Y, Chen F, Zhang Y. Preparation and microstructural characterization of a novel 3D printable building material composed of copper tailings and iron tailings. Constr Build Mater. 2020;249:118779.

79. du Plessis A, Babafemi AJ, Paul SC, Panda B, Tran JP, Broeckhoven C. Biomimicry for 3D concrete printing: A review and perspective. Addit Manuf. 2021 Feb 1;38:101823.

80. krotovstudio. Dubai unveils THE WORLD'S LARGEST 3D PRINTED BUILDING by Apis Cor [Internet]. Apis Cor. 2019 [cited 2024 Oct 9]. Available from: https://apis-cor.com/2019/12/19/dubai-unveils-the-worlds-largest-3d-printed-building-by-apis-cor/

81. Apis Cor: Aerial Rotational Footage of Frank Printing Model House [Internet]. 2024 [cited 2024 Oct 9]. Available from: https://www.youtube.com/watch?v=5lR2XEa5CUg

82. 3D printed amenities block in Dubbo - Contour3D [Internet]. [cited 2023 Oct 3]. Available from: https://contour3d.com.au/our-projects/3d-printed-amenities-block/

83. Wolfs R, Bos D, Salet T. Lessons learned of project Milestone: The first 3D printed concrete house in the Netherlands. Mater Today Proc [Internet]. 2023 [cited 2023 Oct 3]; Available from: https://www.sciencedirect.com/science/article/pii/S2214785323035770

84. Wang L, Jiang H, Li Z, Ma G. Mechanical behaviors of 3D printed lightweight concrete structure with hollow section. Arch Civ Mech Eng. 2020;20:1–17.

85. Bai G, Guan J, Wang L, Li Z, Ma G. Bending performance of 3D printed ultra high-performance concrete composite beams. Addit Manuf. 2024 Jun 5;89:104298.

86. Nair SAO, Tripathi A, Neithalath N. Examining layer height effects on the flexural and fracture response of plain and fiber-reinforced 3D-printed beams. Cem Concr Compos. 2021 Nov 1;124:104254.

87. Asprone D, Auricchio F, Menna C, Mercuri V. 3D printing of reinforced concrete elements: Technology and design approach. Constr Build Mater. 2018;165:218–31.

88. Liu H, Xiao J, Ding T. Flexural performance of 3D-printed composite beams with ECC and recycled fine aggregate concrete: Experimental and numerical analysis. Eng Struct. 2023 May 15;283:115865.

89. Feng P, Meng X, Chen JF, Ye L. Mechanical properties of structures 3D printed with cementitious powders. Constr Build Mater. 2015 Sep 15;93:486–97.

90. Bos FP, Bosco E, Salet TAM. Ductility of 3D printed concrete reinforced with short straight steel fibers. Virtual Phys Prototyp. 2019;14(2):160–74.

91. van Zijl GP a. G, de Borst R, Rots JG. A numerical model for the time-dependent cracking of cementitious materials. Int J Numer Methods Eng. 2001;52(7):637–54.

92. van den Heever M, Bester F, Kruger J, van Zijl G. Numerical modelling strategies for reinforced 3D concrete printed elements. Addit Manuf. 2022 Feb 1;50:102569.

93. van den Heever M, Bester F, Kruger J, van Zijl G. Mechanical characterisation for numerical simulation of extrusion-based 3D concrete printing. J Build Eng. 2021 Dec 1;44:102944.

94. Pessoa S, Guimarães AS, Lucas SS, Simões N. 3D printing in the construction industry - A systematic review of the thermal performance in buildings. Renew Sustain Energy Rev. 2021 May 1;141:110794.

95. Sovetova M, Calautit JK. Influence of printing parameters on the thermal properties of 3D-printed construction structures. Energy. 2024 Oct 1;305:132265.

96. Ramakrishnan S, Muthukrishnan S, Sanjayan J, Pasupathy K. Concrete 3D printing of lightweight elements using hollow-core extrusion of filaments. Cem Concr Compos. 2021;123:104220.

97. Christen H, van Zijl G, de Villiers W. Improving building thermal comfort through passive design – An experimental analysis of phase change material 3D printed concrete. J Clean Prod. 2023 Mar 15;392:136247.

98. Marais H, Christen H, Cho S, De Villiers W, Van Zijl G. Computational assessment of thermal performance of 3D printed concrete wall structures with cavities. J Build Eng. 2021;41:102431.

99. Christen H, van Zijl G, de Villiers W, Moelich M. Validated simulation of thermal performance of phase change material infused recycled brick aggregate in 3D printed concrete. Constr Build Mater. 2023 Nov 10;404:133318.

100. Sun J, Xiao J, Li Z, Feng X. Experimental study on the thermal performance of a 3D printed concrete prototype building. Energy Build. 2021 Jun 15;241:110965.

101. Alkhalidi A, Hatuqay D. Energy efficient 3D printed buildings: Material and techniques selection worldwide study. J Build Eng. 2020;30:101286.

102. Ravula R, Gatheeshgar P. On the thermal-energy performance of 3D printed concrete wall panels designed with varying insulation ratios. J Build Eng. 2023 Oct 15;77:107374.

103. Nemova D, Kotov E, Andreeva D, Khorobrov S, Olshevskiy V, Vasileva I, Zaborova D, Musorina T. Experimental Study on the Thermal Performance of 3D-Printed Enclosing Structures. Energies. 2022;15(12):4230.

104. Suntharalingam T, Upasiri I, Gatheeshgar P, Poologanathan K, Nagaratnam B, Santos P, Rajanayagam H. Energy Performance of 3D-Printed Concrete Walls: A Numerical Study. Buildings. 2021;11(10):432.

105. Briels D, Kollmannsberger S, Leithner F, Matthäus C, Nouman AS, Oztoprak O, Rank E. Thermal Optimization of Additively Manufactured Lightweight Concrete Wall Elements with Internal Cellular Structure through Simulations and Measurements. Buildings. 2022 Jul;12(7):1023.

106. Dziura P, Maroszek M, Góra M, Rudziewicz M, Pławecka K, Hebda M. Influence of the In-Fill Pattern of the 3D Printed Building Wall on Its Thermal Insulation. Materials. 2023 Aug 23;16(17):5772.

107. Cuevas K, Strza\lkowski J, Kim JS, Ehm C, Glotz T, Chougan M, Ghaffar SH, Stephan D, Sikora P. Towards development of sustainable lightweight 3D printed wall building envelopes–Experimental and numerical studies. Case Stud Constr Mater. 2023;18:e01945.

108. AlZahrani AA, Alghamdi AA, Basalah AA. Computational Optimization of 3D-Printed Concrete Walls for Improved Building Thermal Performance. Buildings. 2022;12(12):2267.

109. Panda B. 3D printing of high-volume fly ash mixtures for digital concrete construction [PhD Thesis]. Nanyang Technological University; 2019.

110. Chen Y, Chaves Figueiredo S, Li Z, Chang Z, Jansen K, Çopuroğlu O, Schlangen E. Improving printability of limestone-calcined clay-based cementitious materials by using viscosity-modifying admixture. Cem Concr Res. 2020 Jun 1;132:106040.

111. Rehman AU, Kim JH. 3D concrete printing: A systematic review of rheology, mix designs, mechanical, microstructural, and durability characteristics. Materials. 2021;14(14):3800.

112. Kruger J, Zeranka S, van Zijl G. An ab initio approach for thixotropy characterisation of (nanoparticle-infused) 3D printable concrete. Constr Build Mater. 2019;224:372–86.

113. Standard Test Method for Unconfined Compressive Strength of Cohesive Soil [Internet]. [cited 2024 Nov 12]. Available from: https://www.astm.org/d2166-06.html

114. Ye J, Cui C, Yu J, Yu K, Dong F. Effect of polyethylene fiber content on workability and mechanical-anisotropic properties of 3D printed ultra-high ductile concrete. Constr Build Mater. 2021 Apr 26;281:122586.

115. Adl-Zarrabi B, Boström L, Wickström U. Using the TPS method for determining the thermal properties of concrete and wood at elevated temperature. Fire Mater. 2006;30(5):359–69.

116. Merah A. Methods of concrete accelerated carbonation test: a review. Discov Civ Eng. 2024 Aug 19;1(1):53.

117. Segal L, Creely JJ, Martin AE, Conrad CM. An Empirical Method for Estimating the Degree of Crystallinity of Native Cellulose Using the X-Ray Diffractometer. Text Res J. 1959 Oct;29(10):786–94.

118. Hanžič L, Kosec L, Anžel I. Capillary absorption in concrete and the *Lucas–Washburn* equation. Cem Concr Compos. 2010 Jan 1;32(1):84–91.

119. Agarwal SK, Masood I, Malhotra SK. Compatibility of superplasticizers with different cements. Constr Build Mater. 2000 Jul 1;14(5):253–9.

120. Rashad AM. An overview on rheology, mechanical properties and durability of high-volume slag used as a cement replacement in paste, mortar and concrete. Constr Build Mater. 2018 Oct 30;187:89–117.

121. Kruger J, Zeranka S, van Zijl G. 3D concrete printing: A lower bound analytical model for buildability performance quantification. Autom Constr. 2019 Oct 1;106:102904.

122. Zhao W, Zhao Y, Zhu L, Guan X. Preparation of 3D-Printed Concrete from Solid Waste: Study of the Relationship between Steel Slag Characteristics and Early Performance in 3D Printing. J Mater Civ Eng. 2024 Dec 1;36(12):04024427.

123. Gonçalves B, Exposito C, Toshimi Ishikawa T, Yuuki Koga G. X-ray diffraction study of the early hydration of Portland cements containing calcium carbonate by *in-situ* and *ex-situ* approaches. Constr Build Mater. 2023 Feb 15;365:129947.

124. Goyal R, Verma VK, Singh NB. Hydration of Portland slag cement in the presence of nano silica. Constr Build Mater. 2023 Aug 29;394:132173.

125. Mezhov A, Kulisch D, Goncharov A, Zhutovsky S. A Comparative Study of Factors Influencing Hydration Stoppage of Hardened Cement Paste. Sustainability. 2023 Jan;15(2):1080.

126. Sabeur H, Saillio M, Vincent J. Thermal stability and microstructural changes in 5 years aged cement paste subjected to high temperature plateaus up to 1000 °C as studied by thermal analysis and X-ray diffraction. Heat Mass Transf. 2019 Sep 1;55(9):2483–501.

127. Xiao J, Liu H, Ding T. Finite element analysis on the anisotropic behavior of 3D printed concrete under compression and flexure. Addit Manuf. 2021 Mar 1;39:101712.

128. Enhanced thermoelectric properties of carbon fiber reinforced cement composites. Ceram Int. 2016 Aug 1;42(10):11568–73.

129. Abdolhosseini Qomi MJ, Ulm FJ, Pellenq RJM. Physical Origins of Thermal Properties of Cement Paste. Phys Rev Appl. 2015 Jun 17;3(6):064010.

130. Sarkar PK, Goracci G, Dolado JS. Thermal conductivity of Portlandite: Molecular dynamics based approach. Cem Concr Res. 2024 Jan 1;175:107347.

131. Li Y, Liu W, Xing F, Wang S, Tang L, Lin S, Dong Z. Carbonation of the synthetic calcium silicate hydrate (C-S-H) under different concentrations of CO2: Chemical phases analysis and kinetics. J CO2 Util. 2020 Jan 1;35:303–13.

132. Long WJ, Wu Z, Khayat KH, Wei J, Dong B, Xing F, Zhang J. Design, dynamic performance and ecological efficiency of fiber-reinforced mortars with different binder systems: Ordinary Portland cement, limestone calcined clay cement and alkali-activated slag. J Clean Prod. 2022 Feb 20;337:130478.

133. M. G. G, Shetty KK, Nayak G, Kamath K. Evaluation of Mechanical, Ecological, Economical, and Thermal Characteristics of Geopolymer Concrete Containing Processed Slag Sand. Sustainability. 2024 Jan;16(17):7402.

134. Karadumpa CS, Pancharathi RK. Study on energy use and carbon emission from manufacturing of OPC and blended cements in India. Environ Sci Pollut Res. 2024 Jan 1;31(4):5364–83.

135. Yu Q, Zhu B, Li X, Meng L, Cai J, Zhang Y, Pan J. Investigation of the rheological and mechanical properties of 3D printed eco-friendly concrete with steel slag. J Build Eng. 2023 Aug 1;72:106621.

136. EPD-IES-0001414:001 (S-P-01414) - Portland Slag Cement [Internet]. [cited 2025 Jan 21]. Available from: https://www.environdec.com/library/epd1414

137. Zhu X, Zhang Y, Liu Z, Qiao H, Ye F, Lei Z. Research on carbon emission reduction of manufactured sand concrete based on compressive strength. Constr Build Mater. 2023 Nov 3;403:133101.

138. Bhattacherjee S, Basavaraj AS, Rahul AV, Santhanam M, Gettu R, Panda B, Schlangen E, Chen Y, Copuroglu O, Ma G, Wang L, Basit Beigh MA, Mechtcherine V. Sustainable materials for 3D concrete printing. Cem Concr Compos. 2021 Sep 1;122:104156.

139. Kumar DS, Kumar P, Sah R, Kaza M, Prasad SMR. Converting granulated blast furnace slag into fine aggregate. Int J Civ Eng Res. 2016;7(2):91–103.

140. Faleschini F, Trento D, Masoomi M, Pellegrino C, Zanini MA. Sustainable mixes for 3D printing of earth-based constructions. Constr Build Mater. 2023 Sep 22;398:132496.

141. Bergman TL. Fundamentals of Heat and Mass Transfer. John Wiley & Sons; 2011. 2249 p.

142. C1363 Standard Test Method for Thermal Performance of Building Materials and Envelope Assemblies by Means of a Hot Box Apparatus [Internet]. [cited 2024 Jan 6]. Available from: https://www.astm.org/c1363-19.html

143. Rawal R, Maithel S, Shukla Y, Rana S, Gowri G, Patel J, Kumar S. Thermal Performance of Walling Material and Wall Technology. Part 2: Derivation of U-values of Industrially Manufactured Wall Assemblies. 2020.

144. Henrique dos Santos G, Fogiatto MA, Mendes N. Numerical analysis of thermal transmittance of hollow concrete blocks. J Build Phys. 2017 Jul 1;41(1):7–24.

145. Boukendil M, Abdelbaki A, Zrikem Z. Numerical simulation of coupled heat transfer through double hollow brick walls: Effects of mortar joint thickness and emissivity. Appl Therm Eng. 2017;125:1228–38.

146. Jelle BP, Kalnæs SE, Gao T. Low-emissivity materials for building applications: A state-of-the-art review and future research perspectives. Energy Build. 2015;96:329–56.

147. Principi P, Fioretti R. Thermal analysis of the application of pcm and low emissivity coating in hollow bricks. Energy Build. 2012;51:131–42.

148. Lorente S, Bejan A. Combined `flow and strength' geometric optimization: internal structure in a vertical insulating wall with air cavities and prescribed strength. Int J Heat Mass Transf. 2002 Jul 1;45(16):3313–20.

149. Energy Conservation Building Code 2017 [Internet]. Bureau of Energy Efficiency; 2017 Jun. Available from: https://beeindia.gov.in/sites/default/files/BEE_ECBC%202017.pdf

Appendix A

Costing Analysis

Table A1. Total costs for each lattice configuration, with and without insulation infill.

RT1_ICT	RT1_CI	RT2	RT2_ISR	RT2_ICT	RT2_CI	RT3	RT3_ISR	RT3_ICT	RT3_CI
0.1373	0.1373	0.1387	0.1387	0.1387	0.1387	0.1477	0.1477	0.1477	0.1477
0.0603	0.1057	0.0000	0.0454	0.0590	0.1044	0.0000	0.0454	0.0500	0.0954
2.12	2.12	2.14	2.14	2.14	2.14	2.28	2.28	2.28	2.28
1761.83	1761.83	1779.79	1779.79	1779.79	1779.79	1895.28	1895.28	1895.28	1895.28
1644.27	2882.24	0.0000	1237.97	1608.82	2846.79	0.0000	1237.97	1363.41	2601.38
48.64	85.26	0.0000	36.62	47.59	84.22	0.0000	36.62	40.33	76.96
229.36	229.36	231.70	231.70	231.70	231.70	246.74	246.74	246.74	246.74
355.43	355.43	359.06	359.06	359.06	359.06	382.36	382.36	382.36	382.36
134.11	134.11	135.48	135.48	135.48	135.48	144.27	144.27	144.27	144.27
47.44	47.44	47.44	47.44	47.44	47.44	47.44	47.44	47.44	47.44
27.33	27.33	27.61	27.61	27.61	27.61	29.40	29.40	29.40	29.40
4248.42	5523.02	2581.08	3855.68	4237.50	5512.09	2745.49	4020.08	4149.23	5423.82
0.9309	0.7059	1.7339	0.7973	1.0145	0.7530	1.8024	0.8023	1.0345	0.7735
2038.47	2652.93	1936.96	1500.59	2194.94	2741.96	3220.82	1640.19	2150.54	2716.52

Lattice Configuration	RH2M	RH2M_ISR	RH2M_ICR	RH2M_CI	RT1	RT1_ISR
Footprint volume (m^3)	0.1069	0.1069	0.1069	0.1069	0.1373	0.1373
Insulation volume (m^3)	-	0.0454	0.0907	0.1361	-	0.0454
Print time (hr)	1.65	1.65	1.65	1.65	2.12	2.12
3D printable material cost (INR)	1371.74	1371.74	1371.74	1371.74	1761.83	1761.83
Insulation material cost (INR)	-	1237.97	2473.22	3711.19	-	1237.97
Insulation installation cost (INR)	-	36.62	73.16	109.79	-	36.62
Printer operator cost (INR)	178.58	178.58	178.58	178.58	229.36	229.36
Labour cost (INR)	276.73	276.73	276.73	276.73	355.43	355.43
Printer electricity cost (INR)	104.42	104.42	104.42	104.42	134.11	134.11
Mixer electricity cost (INR)	47.44	47.44	47.44	47.44	47.44	47.44
Pump electricity cost (INR)	21.28	21.28	21.28	21.28	27.33	27.33
TOTAL (INR)	2000.19	3274.79	4546.57	5821.17	2555.51	3830.10
U value	2.0338	0.8204	0.5657	0.4978	1.7159	0.7936
Cost Performance Index (CPI)	REF	1050.44	1734.48	2487.612	1746.84	1475.50

Publications

Publications from PhD thesis

International Journals

1. **Dey, D.**, Srinivas, D., Panda, B., Suraneni, P., & Sitharam, T. G. (2022). Use of industrial waste materials for 3D printing of sustainable concrete: A review. *Journal of Cleaner Production, 340,* 130749. https://doi.org/10.1016/j.jclepro.2022.130749
2. **Dey, D.**, Van, V. N., Xuan, H. N., Srinivas, D., Panda, B., & Tran, P. (2023). Flexural performance of 3D printed concrete structure with lattice infills. *Developments in the Built Environment, 16,* 100297. https://doi.org/10.1016/j.dibe.2023.100297.
3. **Dey, D.**, & Panda, B. (2023). An experimental study of thermal performance of 3D printed concrete slabs. *Materials Letters, 330,* 133273. https://doi.org/10.1016/j.matlet.2022.133273
4. **Dey, D.**, Panda, B., Shukla, Y., & Rawal, R. (2025). A comprehensive assessment of thermal performance of 3D printed concrete lattice walls. Progress in Additive Manufacturing, 1-18. https://doi.org/10.1007/s40964-025-01042-3
5. **Dey, D.**, Panda, B. & Kole, J. Sustainable slag based 3D concrete printing: effect of slag cement and slag sand on the rheology, mechanical and thermal properties, (**Manuscript prepared**).

Patents

1. D. Dey, B. Panda, J. Kole, M. Rastogi. 2025. PRINTABLE CEMENTITIOUS COMPOSITION AND PREPARATION METHOD THEREOF. Indian Patent, filed May 15, 2025. Patent Published. Patent Application No.: 202531046998
2. D. Dey, B. Panda, Y. Shukla, R. Rawal. PROCESS FOR MAKING CONCRETE 3D PRINTED WALLS WITH DIVERSE LATTICE DESIGNS. Indian Patent filed, February 08, 2024. Patent Published. Patent Application No.: 20243100846

Conference Papers and Book Chapters

1. **Dey, D.**, Sahu, A., Prakash, S., & Panda, B. (2023). A study into the effect of material deposition methods on hardened properties of 3D printed concrete. *Materials Today: Proceedings.* https://doi.org/10.1016/j.matpr.2023.03.034
2. **Dey, D.**, & Panda, B. (2024). Numerical evaluation of thermal performance and improvement strategies for 3D printed concrete structures. *Digital Concrete 2024 - Supplementary Proceedings.* https://doi.org/10.24355/dbbs.084-202408191219-0.

Other Publications

International Journals

1. Srinivas, D. *, **Dey, D. ***, Panda, B., and Sitharam. T.G. (2022). Printability, thermal and compressive strength properties of cementitious materials: A comparative study with silica fume and limestone. *Materials, 15(23),* 8607. https://doi.org/10.3390/ma15238607 (* Co-First Author)
2. Kumar, L., **Dey, D.**, Panda, B., & Muthu, N. (2023). Experimental and numerical evaluation of multi-directional compressive and flexure behavior of three-dimensional printed concrete. *Frontiers of Structural and Civil Engineering, 17(11),* 1643-1661. https://doi.org/10.1007/s11709-023-0004-z

Conference Papers and Book Chapters

1. **Dey, D.**, Srinivas, D., Boddepalli, U., Panda, B., Gandhi, I. S. R., & Sitharam, T. G. (2022). 3D printability of ternary Portland cement mixes containing fly ash and limestone. *Materials Today: Proceedings, 70,* 195-200. https://doi.org/10.1016/j.matpr.2022.09.020
2. **Dey, D.**, Srinivas, D., Panda, B., & Sitharam, T. G. (2022). Processing of cementitious materials for 3D concrete printing. In *Industry 4.0 and Advanced Manufacturing: Proceedings of I-4AM 2022* (pp. 283-291). Singapore: Springer Nature Singapore. https://doi.org/10.1007/978-981-19-0561-2_26
3. **Dey, D.,** Kumar, G., Prasad, V. D., & Panda, B. (2024). Experimental Investigation of Thermal Performance of 3D Printed Slab Infused with Lightweight Concrete as Insulation. In *International Conference on Additive Manufacturing* (pp. 111-121). Singapore: Springer Nature Singapore. https://doi.org/10.1007/978-981-97-6016-9_10
4. Srinivas, D., Boddepalli, U., **Dey, D.**, Choaudhary, B., Panda, B., Sitharam, T. G., & Ranjani, G. I. S. (2022). Development of Outdoor Furniture Using 3D Concrete Printing. In *North-East Research Conclave* (pp. 51-61). Singapore: Springer Nature Singapore. https://doi.org/10.1007/978-981-97-5870-8_5
5. Maurya, S., **Dey, D.**, Panda, B., & Dixit, U. S. (2023). Inline reinforcement of steel cable in 3D concrete printing. *Materials Today: Proceedings.* https://doi.org/10.1016/j.matpr.2023.04.092

Patents

1. D. Srinivas, D. Dey, B. Panda, T.G. Sitharam. 2023. CEMENTITIOUS COMPOSITIONS FOR UNDERWATER EXTRUSION 3D PRINTING AND PREPARATION METHOD THEREOF. Indian Patent, filed January 05, 2023. Patent filed. Patent Application No.: 202331001244

Poster Presentations

1. D. Dey, & B. Panda (2024), "Numerical evaluation of thermal performance and improvement strategies for 3D printed concrete structures". Presented at 4th RILEM International Conference on Concrete and Digital fabrication held at Technical University of Munich from September 04-06, 2024.
2. S.B.F. Warsi, U. Boddepalli, D. Srinivas, D. Dey, B. Choaudhary, B. Panda, T. G. Sitharam, and I. S. R. Gandhi, "Development of outdoor furniture using 3D concrete printing" North East Research Conclave held at Indian Institute of Technology, Guwahati, India, May 20-22, 2022.
3. D. Srinivas, U. Boddepalli, S.B.F. Warsi, D. Dey, B. Panda, T. G. Sitharam, and I. S. R. Gandhi, "Development of 3D Printed Structures at IIT Guwahati" presented among the selected projects at G20 summit in February, 2023. Organized by IIT Guwahati.

Achievements

1. Awarded with Prime Minister's Research Fellowship in the lateral entry category for the 8th cycle in December 2021.
2. Won the best exhibitors award in the "Innovation for the future" category in the North-East Research Conclave (NERC) held at IIT Guwahati on May 20-22, 2022.
3. Received Certificate of Completion for "Conceptualization, Design & Execution of 3D Printed Sentry Post" to Indian Army on dated 06th October 2022.
4. Received Best paper award at 2nd International Conference on Construction Materials and Structures (ICCMS 2022) held during 13-19 December 2022.
5. Received Student Project Grant on "Image based Deformation Measurement Tool for Additive Manufacturing, funded by: NewGen IEDC, DST, Govt. of India, Funding amount: 2 lakhs, (Completed in March 2023).
6. Pre-finalists in a competition conducted by TATA Steel named "Material Next 4.0" held in April 2023.
7. Received Best paper award at International Conference on Additive Manufacturing (ICAM 2024) held during March 04-06, 2024.